Parallel Transmission for Magnetic Resonance Imaging on a 9.4 Tesla Human System

A DISSERTATION
SUBMITTED TO THE FACULTY OF THE GRADUATE SCHOOL
OF THE UNIVERSITY OF MINNESOTA
BY

Xiaoping Wu

IN PARTIAL FULFILLMENT OF THE REQUIREMENTS
FOR THE DEGREE OF
DOCTOR OF PHILOSOPHY

Advisor: Kâmil Uğurbil
Co-advisor: Pierre-François Van de Moortele

January, 2010

Acknowledgements

Time flies, and it was just like yesterday when I first came to the USA. Looking back, there are many people that have earned my gratitude for their contribution to my time at the University of Minnesota.

First and foremost, I like to thank my advisor, Prof. Kamil Ugurbil, for his unlimited support, encouragement and inspiration throughout my PhD study. Kamil introduced me to the field of magnetic resonance and provided me with all I need to accomplish my work. Although very busy, he was always there when I needed him. I truly appreciate the time and respect he has given me.

I like to express my appreciation from the bottom of my heart to my co-advisor, Prof. Pierre-Francois Van de Moortele, for his outstanding instruction, constant support and tremendous help. It has been a pleasure working with and learning from him. His enthusiasm, confidence, optimism and uncompromisingly high academic standard has motivated me to work on this challenging and interesting project, and will surely have an inspiring influence in my future career. Pierre-Francois has spent millions and millions of hours patiently providing me with answers and directions, and passionately revising my papers and abstracts. For all that, I am for ever indebted.

I am grateful to Prof. Michael Garwood for serving as chair of my PhD Oral Committee, revising my abstract and providing constructive suggestions on my research. Also, it was from him that I learned nearly everything I know about the beauty of frequency swept RF pulses.

I give my appreciation to Prof. Wei Chen, Prof. Russell Ritenour and Prof. Tommy Vaughan for being on my PhD Preliminary and Final Oral Committee, and taking time to review my dossier and dissertation.

I am fortunate to have been a member of the big family of CMRR, from which I

benefitted alot. I thank Prof. Pierre-Gilles Henry for giving me kind instruction and help to get started with magnetic resonance.

I appreciate the generous help and support from Dinesh Deelchand, who shared with me his experimental tools and helped me with experiment troubleshooting.

I thank Can Akgun for providing me with electromagnetic simulations, Peter Andersen, John Strupp, and Lance DelaBarre for setting up the 9.4T multi transmit system, and Gregor Adriany and Carl Snyder for building the RF coils used in this work.

I like to thank Prof. Patrick Bolan for great conversations on kids and breast cancer. From him, I knew that RF coils can actually be made like a bra.

I like to thank Steen Moeller for stimulating and insightful discussions on solving inverse problems, Ute Goerke and Johannes Ritter for explaining to me basics of MR, and Malgorzata Marjanska for teaching me pulse sequences for MR spectroscopy and helping me with my Illustrator.

I thank Prof. Arthur From for broadening my knowledge about USA and the world, and impressing me by a mountain of papers around his cubicle that he has read.

I thank Prof. Greg Metzger for offering me a ride home with his brick on wheels when my bike got broken legs, and Prof. Noam Harel for helping me with my class essay on ocular dominance columns.

I also thank Eddie Auerbach for answering my non-7T questions and showing me that a kids bike would be much more useful if it came with no pedals at all, Angela Styczynski for proofreading my dossier and answering my questions about study in BME, Isabelle Iltis for making me believe that iTouch is also a StarWar laser sword, and Nate Powell for showing me that RF can draw concentric rings in MR brain imaging.

I like to thank Brian Hanna and Janis Zeltins for their reliable support to my use of internet and computer, Jeramy Kulesa for his help in making my water phantoms, and Deb Morgan, Cindy Spehn and Nicole Wilkinson for their warm-hearted assistance with my paperwork and volunteer arrangement.

I thank Prof. Kelvin Lim, Prof. Essa Yacoub, Prof. Shalom Michaeli, Prof. Ivan Tkac, Prof. Gulin Oz, Prof. Silvia Mangia, Prof. Melissa Terpstra and Prof. Tonya White for their best wishes and support.

Qiang Xiong and I became good friends soon after he came to CMRR. His friendship and support has made my life more pleasant at the University of Minnesota. I thank

him for sharing with me his knowledge about phosphorus MR spectroscopy and his thoughts on MRI.

I also thank Xiaoliang Zhang, Wanzhan Liu, Tram Nguyen, Nanyin Zhang, Xiao Liu, Xiaohong Zhu, Fei Du, Yi Zhang, Xiao Wang, Wen Ling, Curt Corum, Jang-Yeon Park, Djaudat Idiyatullin, Ryan Muetzel, Jinfeng Tian, Devashish Shrivastava, Uzay Emir, and Alexander Shestov, for making my time more enjoyable at the CMRR.

I thank my new groupmates Federico De Martino, Julien Sein and Sebastian Schmitter for their encouragement and help. With you, I am expecting much more fun.

Further, many other people from outside CMRR deserve my thanks. I owe a big thank you to Mrs. Barbara Beers for teaching me how to teach and helping me with my English.

I thank Xiaoxiao Kong, Shuai Leng and his wife Dong Han, for their friendship and support. I really enjoyed the time we spent together playing, eating and talking. They have been family to us all these years.

Yingpeng Wang, Longlong Nian, Jiahui Zhang, Yu Zhang and Jinsong Wu have been my best friends for many years. Although far away from me, they have been an endless source of moral support. Their encouragement and consideration has help me up through the toughest times.

As a collaborator, Tsung-Hui Chang has been a good friend since the very beginning. I appreciate the effort and time he put during our discussions on nonconvex optimization.

I thank Chenguang Liu, Zhongming Liu, Han Yuan, Xu Li, Dalong Liu, Junfeng Gao, and Jie Song for making my experience at the U more pleasant.

I thank my father, Side Wu, and my step mother, Aiping Guo, for their support and encouragement, and my parents in law, Yuqin Guan and Zhangxiang Wang, for their trust in me and their help in taking care of our baby girl.

Last, but not the least important, I like to thank my wife, Qi Wang, and my daughter, Amy Ziyue Wu, for their deep and unfailing love. Without them, nothing is meaningful in my life. Qi, thank you for your companion, support, encouragement and understanding over all these years; thank you for giving me Ziyue, the loveliest and most beautiful girl in the world; Thank you for all the sacrifices you have made for me. Yueyue, my little angel, thank you for cheering us on, just by being what you are.

Dedication

This dissertation is dedicated to my mother, Mingying Lai.

Abstract

Over the recent years, researchers have been increasingly pushing towards using ultra high magnetic field (7 Tesla and higher) for magnetic resonance imaging in human in order to benefit from substantial increases in signal to noise ratio and contrast. However, at ultra high field, severe transmit B_1 (B_1^+) inhomogeneity occurs, limiting applications of most conventional MR techniques. Multidimensional spatially selective RF pulses have been proposed as a method to mitigate B_1^+ inhomogeneity. However, those RF pulses are typically very long and are impractical at high field. Parallel transmission, an emerging technique, makes it possible to design sufficiently short selective RF pulses for use in actual experiments. In this thesis, we demonstrate the first successful implementation of parallel transmission at an ultra high field of 9.4 Tesla (T) in the human brain with an eight-channel transmit system, using accelerated ($\times 4$) RF pulses designed to create arbitrarily shaped excitation profiles. To achieve satisfactory excitation accuracy, k-space errors due to gradient system imperfection had to be accurately calibrated and integrated in RF pulse calculation. In order to limit RF power deposition in tissues, an inherent concern for patient safety at very high field, we introduced and demonstrated a new 2D RF pulse design method that effectively reduces specific absorption rate (SAR) while preserving excitation pattern fidelity. SAR reduction efficiency was demonstrated with numerical simulations while excitation pattern fidelity was experimentally verified at 9.4T. Additional preliminary work relevant to B_1^+ manipulation at high field were also conducted through the course of this thesis, including the implementation of spoke trajectory based transmit excitation with 16 channels at 9.4T, a fast 2D B_1 mapping technique and in-depth simulation of SAR in the human brain with multi transmission.

Contents

List of Tables

List of Figures

Chapter 1

Introduction

Magnetic resonance imaging (MRI) is one of the most popular non-invasive medical imaging techniques used to visualize structure and function of the human body. Unlike computerized tomography (CT), it uses no ionizing radiation. Instead, it uses a strong static magnetic field and radiofrequency (RF) waveforms to produce clear and detailed images. MRI also provides great contrast between different soft tissues of the body and thus is a preferred method to diagnose soft tissue diseases, especially those in brain, spinal cord, and pelvis.

Since the first anatomical MR images were obtained, the magnetic field used for clinical MR systems has been steadily increasing from a fraction of Tesla (T) to 1T, then to 1.5T, and more recently to 3T. The main reason for using a higher field is that signal to noise ratio (SNR) is approximately proportional to the magnetic field strength. However, as the field strength increases, challenging obstacles arise from the complex propagation of RF waves in large biological samples at increased frequencies, with consequences that are seriously deleterious for clinical applications. Of particular concern are severe transmit B1 inhomogeneities, leading to large flip angle variations observed in human tissues that can affect both tissue contrast and SNR [1, 2]. The severe transmit B1 distortions observed in the early attempts to image humans at 4T [3, 4] initially discouraged the constructors from building higher field scanners, as no solution was yet available to address this issue.

Nevertheless, there has been a noticeable push towards ultra high magnetic field strength ($\geq$ 7 T) to benefit from improved image SNR, enhanced blood-oxygen-level

dependent (BOLD) contrast in functional MRI and increased chemical dispersion in MR spectroscopy. It should be mentioned that the Center for Magnetic Resonance Research (CMRR) at the University of Minnesota has played a critical role in pioneering the use of very high magnetic fields in humans, starting with a 4T system, then with the first 7T human scanner, and later at 9.4T, at times when many in the community doubted about the future of ultra high field systems [1, 5–9].

Addressing the large flip angle variations due to severe transmit B1 inhomogeneities is essential in enabling clinical investigations in humans at ultra high field. Several approaches have been proposed to address transmit B1 inhomogeneities, such as RF coil design [10, 11], passive dielectric padding [12], adiabatic RF pulses [13, 14], and composite RF pulses [15]. It should be noted that several of those approaches had actually been proposed at low field where B1 inhomogeneities also occurred with surface coils. Recently, there has been increasing interest in using multidimensional spatially selective RF pulses, initially introduced by Pauly et al. [16] and Hardy et al. [17], to mitigate transmit B1 inhomogeneities [18, 19]. However, these RF pulses, when used with a single transmit channel, are typically very long due to limited gradient system capability, making them impractical in clinical MR applications.

Katscher et al. [20] and Zhu [21] successfully introduced the concept of utilizing the principles of parallel imaging [22–24] in RF transmission, which consists of exploiting the spatial sensitivity profiles of RF coils as a way to encode a fraction of spatial excitation information. Their work demonstrated that parallel transmission [20, 21, 25–27] with multiple RF transmit channels allows for short, accelerated spatially selective RF pulses. The implementation of parallel transmission became possible after two hardware breakthroughs: new RF coils made of multiple independent transmit coil elements [28], and RF shape boards capable of generating multiple independent RF waveforms. It should be emphasized that although so-called static B1 shim techniques constitute a major advance in transmit B1 inhomogeneity mitigation [29], they are not the focus of this thesis and will not be specifically discussed. Besides, B1 static shim could be described as a subset of parallel transmission.

Early work in parallel transmission includes development of accelerated RF pulse design algorithms based on linearization of the Bloch equations using small tip angle approximation [20, 21, 30]. However, the experimental verification of parallel transmission

was limited due to the expensive hardware requirements. In the first papers [20, 21], the concept of parallel transmission was only verified using the emulation on a single-channel RF transmit system. In 2005, the first full realization of parallel transmission was demonstrated using phantom experiments performed on a three-channel human, and four-channel animal scanners at 3T and 4.7T respectively [25]. Soon after that, successful parallel transmission using eight channels at 3T was reported [26]. Meanwhile, parallel transmission started to be evaluated for biological and medical applications with images acquired in humans, animals and biological samples [31]. Moreover, preliminary studies were also performed, based on a phantom model, to analyze the specific absorption rate (SAR) in parallel transmission [32, 33].

The long term goal of the research presented in this thesis is to enable and improve clinical application in humans at the highest magnetic field available in humans, currently 9.4 Tesla, by extensively exploiting parallel transmission capability. However, parallel transmission had never been demonstrated at this high field and a number of methodological issues needed to be solved on our system before successful results could be obtained. Critical to multi transmission implementation is the calibration of gradient errors. It was found that even when using the system eddy current preemphasis, significant gradient errors occurred on our 9.4T system, resulting in dramatic degradations of parallel transmit excitation patterns. In chapter 4 we describe how to obtain satisfactory excitation accuracy in the human brain at 9.4T. We developed the necessary tools to measure and incorporate the actual distorted gradient waveforms into RF pulse calculation. After this successful implementation, we addressed a critical issue at very high field, namely SAR levels due to increased demand in RF power. Such SAR concerns are exacerbated when using accelerated 2D RF pulses and we describe in chapter 5 a new RF pulse design approach allowing for effective SAR reduction when using accelerated 2D pulses in multi transmission. This novel pulse design method is based on the VERSE principle originally introduced for 1D slice selective RF excitation [34]. The effectiveness of adapted rate RF pulses in SAR reduction was demonstrated with electromagnetic simulations, and the accuracy of the excitation patterns was experimentally verified at 9.4T.

The outline of this dissertation is as follows.

- Chapter 2 briefly presents the history and principles of magnetic resonance imaging, as well as relevant methods that have been used in this thesis.

- Chapter 3 describes a simulation study, aiming at investigating parallel transmission using an electromagnetic model closely reproducing experimental conditions at 9.4 T.

- Chapter 4 presents the first successful parallel transmission experiments in humans at 9.4 T. This work was presented at the scientific meeting of ISMRM [35] and has been accepted for publication in Magnetic Resonance in Medicine [36].

- Chapter 5 describes a novel method for designing adapted 2D RF pulses with reduced levels of SAR in parallel excitation. This work which was presented at the scientific meeting of ISMRM [37, 38] has been submitted for publication in Journal of Magnetic Resonance.

- Chapter 6 covers additional preliminary studies, presented at the annual meetings of the ISMRM, that are directly relevant to transmit B1 manipulation at very high field. These include parallel transmission with spoke trajectories at 9.4 T using 16 RF transmit channels [39], in-depth SAR analysis for parallel transmission with a human head model [40], a new, fast 2D transmit B1 mapping technique derived from 3D-only actual flip angle imaging [41], and a novel algorithm for single-shot OVS pulse design [42].

- Chapter 7 summarizes the key components of this thesis and provides directions for future research.

Chapter 2

Background

2.1 A Brief Historical Review of Magnetic Resonance

The development and application of nuclear magnetic resonance (NMR) involves two major fields. One is magnetic resonance spectroscopy (MRS) which started about 60 years ago and constitutes a major analysis tool in chemistry to determine the composition of a wide range of compounds in liquid and solid state forms. The other field is magnetic resonance imaging (MRI) which was developed several decades later and is vastly known today as a powerful tool in medical imaging. Practically, once MR scanners became imaging devices for clinical diagnosis, the term "nuclear" was removed from "NMR" as it could suggest some relation with radioactivity and nuclear medicine techniques.

In 1946, Bloch et al. [43] and Purcell et al. [44] independently discovered the physical phenomenon of NMR, and in 1952 they shared the Nobel Prize in Physics in recognition of their pioneering work. A few years after the discovery of NMR phenomena, Proctor et al. [45] and Dickinson [46] independently found chemical shift effects in NMR spectra in 1950. After that, NMR became a very important technique for non-destructive chemical analyses. Initially, MR studies were based on sweeping the RF excitation and reception through a range of MR frequencies. Sixteen years later in 1966, Ernst [47] revolutionized NMR by introducing pulsed NMR in combination with Fourier transformation where a large range of MR frequencies were excited simultaneously instead of sequentially. Interest in possibilities of using NMR for medical diagnosis began in 1971

with Damadian's work on the differences in relaxation times between different tissues, and between normal and cancerous tissues [48].

The discovery and development of MRI is one of the most spectacular and successful events in the history of medical imaging. However, there is a time gap of almost 30 years between the discovery of NMR and the first imaging experiments. This was mainly due to the fact that imaging could not be performed with just a simple RF detector since the needed voxel size is tens or hundreds of times shorter than the RF wavelength in biological tissues.

In order to work around this very limiting constraint, Lauterbur introduced in 1973 the use of a gradient of the main magnetic field to impose a linear variation of the frequency of MR signals as a function of the spatial location of their source [49]. This space-frequency encoding principle was a fantastic breakthrough that opened the door towards the development of Magnetic Resonance Imaging. The very first published demonstration consisted of a two-dimensional MR image of a water-filled structured object reconstructed in a similar projection based procedure used in computerized tomography [49]. Later, Mansfield proposed the so called "echo-planar" technique providing the advanced idea for very fast imaging [50]. In 2003 Lauterbur and Mansfield were awarded the Nobel Prize in Physiology or Medicine for their pioneering contributions to MRI.

In 1982, Brown et al. [51] introduced the concept of k-space trajectory for MR imaging in their study on three-dimensional NMR chemical shift imaging. The application of this k-space trajectory formulation, which was discussed in detail in 1983 [52], proved to be a very powerful analytical tool for assessing imaging performance and for deriving improved MR imaging techniques. A large number of new or alternative imaging sequences have been directly conceived by varying the traversal in k-space. A couple of years later, Pauly et al. [16] introduced the concept of excitation k-space trajectory for the design of multidimensional spatially selective RF pulses.

Since the first publications, the field of NMR has been growing at an impressively high rate with astonishing diversity, especially in biomedical applications. A non-exhaustive list of MR contrast between biological tissues includes proton density, longitudinal and transversal relaxation times, diffusion and perfusion. Furthermore, dynamic variations of contrast through time allows the investigation of multiple organ

functions, using either exogenous or endogenous contrast agents. Human brain functional MRI (fMRI) is probably the most well known illustration of the latter, where MR signal changes secondary to variations in perfusion that correlate with local changes in cerebral activity can be mapped in a noninvasive manner [5, 53, 54]. In less than two decades fMRI has become by far the most used noninvasive technique to map the human brain functions in healthy volunteers.

2.2 Principles of Nuclear Magnetic Resonance

Nuclei containing a number of protons and neutrons possess the intrinsic property of spin. In quantum mechanics, spin is characterized by the spin quantum number S which takes non-negativef integers or half integers. A non-zero spin $\mathbf{S}$ is always associated with a non-zero magnetic moment $\boldsymbol{\mu}$ via the relation $\boldsymbol{\mu} = \gamma\mathbf{S}$, where γ is the gyromagnetic ratio in $\text{rad} \cdot \text{s}^{-1} \cdot \text{T}^{-1}$ and is a constant for a given nucleus. The possible spin states of a particular nucleus with spin S are specified by the magnetic quantum number, m_s, which takes values from $-S$ to S in step of one, i.e., $m_s = -S, -S+1, \ldots, S-1, S$. This gives a total of $(2S+1)$ spin states.

Hydrogen nuclei, which contain a single proton, possess a spin of one half (i.e., $S = \frac{1}{2}$) and thus have two possible spin states: $m_s = +\frac{1}{2}$ or $m_s = -\frac{1}{2}$. In the absence of an external magnetic field, these two states are degenerate and have the same energy. Therefore, the number of protons in each state will be approximately equal at thermal equilibrium. However, when an external magnetic field, B_0, is applied, the interaction between the nuclear magnetic moment and the magnetic field will break the degeneracy, causing the two states to have two energy levels: $E = +\frac{1}{2}\hbar\gamma B_0$ and $E = -\frac{1}{2}\hbar\gamma B_0$, where $\hbar = \frac{h}{2\pi}$ is the reduced Planck constant. The energy difference between the two states is $\Delta E = \hbar\gamma B_0$. This energy difference results in a small population bias towards the lower energy state (i.e., more protons are in the lower energy state at thermal equilibrium), giving rise to a net bulk magnetic moment or magnetization in parallel to B_0. Once deviated from the orientation of B_0, this magnetization, made up of a large number of spins, will be precessing about B_0 at the Larmor frequency, ω_0, which is proportional to the field strength, $\omega_0 = \gamma B_0$.

In MR imaging, hydrogen nuclei, commonly referred to as protons, have been used

as the signal source because the human body is largely composed of water. For signal generation, an external main magnetic field, B_0, is always present to polarize protons. By convention, the direction of B_0 usually defines the z axis.

After the magnetization is built up, an RF electromagnetic field pulse, oscillating at the resonance frequency of protons, is applied with an RF coil to excite or flip the magnetization. This RF pulse, generating a magnetic field, B_1, in the xy plane, will rotate the magnetization away from the z axis at certain flip angles. After the RF pulse is turned off, with the main magnetic field present, the transverse magnetization will precess about the z axis at the Larmor frequency. According to Faraday's law, this precession of magnetization, generating a time varying magnetic flux, will induce a small current in the RF receive coil.

To build an MR image, one must be able to resolve signals for different volume elements (voxel) despite of the fact that the size of these voxels is several order of magnitude smaller than the wavelength. This is achieved by encoding different positions in space with different precessing frequencies by means of a linear magnetic field gradient, $\mathbf{G}$, superimposed over the main magnetic field B_0. With this gradient, the net magnetic field along the z direction is now linearly dependent on the spatial coordinate $\mathbf{r}$, i.e., $B(\mathbf{r}) = B_0 + \mathbf{G} \cdot \mathbf{r}$, where $\cdot$ denotes the dot product of two vectors. Consequently, the spin frequency, ω, is also linearly related to the space, $\omega(\mathbf{r}) = \gamma(B_0 + \mathbf{G} \cdot \mathbf{r})$. Therefore, a signal acquired when a gradient is applied will contain different frequencies each corresponding to a different voxel which has contributed to the signal. After appropriate reconstruction of the MR signal in the frequency domain (e.g., Fourier transform), the signal of each voxel is identified by its corresponding frequency which in turn corresponds to a specific location in space.

The same general principle applies during excitation. In a simplified representation, in order to obtain a selective excitation (e.g. slice selective pulse) one can use an RF pulse of a limited bandwidth centered on a particular frequency while applying a magnetic gradient superimposed to B_0. In these circumstances, only the spins experiencing a Larmor frequency contained within the RF pulse central frequency +/- half its bandwidth will be excited.

2.3 Spatially Selective Excitation

2.3.1 The Bloch Equations

Before discussing spatially selective RF excitation where simultaneous applications of RF and gradient pulses are required to achieve a desired excitation pattern, we first need to consider the Bloch equations which mathematically describe the dynamic evolution of the magnetization as a result of the magnetic field, the relaxation constants and the diffusion. The complete Bloch equations actually consist of a system of differential equations [55]:

$$\frac{d\mathbf{M}}{dt} = \gamma \mathbf{M} \times \mathbf{B} - \frac{M_x \hat{\boldsymbol{x}} + M_y \hat{\boldsymbol{y}}}{T_2} - \frac{(M_{z,0} - M_z)\hat{\boldsymbol{z}}}{T_1} + D\nabla^2 \mathbf{M} \tag{2.1}$$

with

$$\nabla^2 \equiv \frac{\partial^2}{\partial x^2} + \frac{\partial^2}{\partial y^2} + \frac{\partial^2}{\partial z^2}$$

where $\mathbf{M} = [\, M_x, M_y, M_z \,]^{\mathrm{T}}$ is the magnetization vector in a rectangular coordinate system spanned by the three unit vectors $(\hat{\boldsymbol{x}}, \hat{\boldsymbol{y}}, \hat{\boldsymbol{z}})$. $M_{z,0}$ is the initial z component of magnetization. The vector $\mathbf{B}$ is the effective magnetic field. D is the molecular self-diffusion coefficient, and γ is the gyromagnetic ratio. T_1 and T_2 are the transverse and longitudinal relaxation times, respectively.

For MR imaging, an RF pulse generating a time dependent magnetic field in the transverse plane (xy plane) along with a time varying gradient of the main magnetic field is generally used to excite the spins. In this case, the effective magnetic field seen in the laboratory frame will be the sum of the main magnetic field, the RF induced magnetic field and the gradient related magnetic field. If we step into the rotating frame which rotates about the main field B_0 in the laboratory frame at the Larmor frequency ($\omega_0 = \gamma B_0$), the main field will be unseen since the nutation of the magnetization due to this field disappears as a result of the same rotation of the rotating frame. Therefore, the Bloch equations that describe the dynamics of the magnetization in the rotating frame during an RF excitation, ignoring the relaxation and diffusion effects, can be written as

$$\frac{\mathrm{d}\mathbf{M}(\mathbf{r},t)}{\mathrm{d}t} = \gamma \mathbf{M}(\mathbf{r},t) \times \{\, B_{1,x}(\mathbf{r},t)\hat{\boldsymbol{x}} + B_{1,y}(\mathbf{r},t)\hat{\boldsymbol{y}} + [\mathbf{G}(t)\cdot\mathbf{r}]\hat{\boldsymbol{z}} \,\} \tag{2.2}$$

where $\mathbf{G}(t)$ is a space independent gradient of the main magnetic field. $B_{1,x}(\mathbf{r},t)$ and $B_{1,y}(\mathbf{r},t)$ are the transverse components of the time varing B_1 field at a certain location denoted by $\mathbf{r}$. From this equation, it can be seen that while the RF flips the magnetization a certain angle away from the z axis, the gradient causes the magnetization to precess about the z axis. As will be discussed next, the differential equation (Eq. 2.2) can be simplified and then can be analytically solved under certain conditions for the transverse magnetization provided the RF and gradient.

2.3.2 Small-Tip-Angle RF Design

When large flip angle excitation is desired, the nonlinear Bloch equations (Eq. 2.2) have to be solved iteratively in order to calculate the required RF pulses for a desired final magnetization distribution. In this case, complicated computations are expected. However, when the flip angles are small, a linear relation between the applied RF and the resulting magnetization can be obtained from Eq. 2.2 by introducing some approximations. Using this linear relation for RF pulse design will require relatively simple RF calculations.

As described in Ref. [16], if the initial magnetization is at equilibrium, pointing to the z axis (i.e., $\mathbf{M}(\mathbf{r},0) = [\,0,0,M_0\,]^{\mathrm{T}}$, where M_0 is the magnetization amplitude), the transverse magnetization at the end of the RF pulse can be solved from Eq. 2.2 and is given by

$$\tilde{M}_{\perp}(\mathbf{r},T) = i\gamma \int_0^T M_z(\mathbf{r},t)\,\tilde{B}_1(\mathbf{r},t)\,e^{-i\gamma\mathbf{r}\cdot\int_t^T \mathbf{G}(\tau)\,\mathrm{d}\tau}\,\mathrm{d}t \tag{2.3}$$

where $i=\sqrt{-1}$, and T is the pulse duration. $\tilde{M}_{\perp} = M_x + iM_y$ and $\tilde{B}_1 = B_{1,x} + iB_{1,y}$ are the complex representations respectively for the transverse magnetization and the applied RF pulse. From now on, a tilde over a symbol is used to indicate a complex value unless otherwise specified. Note that Eq. 2.3 still does not provide a linear relation between the RF and the magnetization since the unknown z component of magnetization (i.e., $M_z(\mathbf{r},t)$) shows in the time integral of RF pulse, and therefore, further manipulations are needed to reach a linear relation.

If the flip angle of the magnetization is further assumed to be always small during the RF pulse (i.e., $M_z(\mathbf{r},t) \approx M_0$ over time), we can substitute the constant magnetization amplitude M_0 for the time varing magnetization z component $M_z(\mathbf{r},t)$ in Eq. 2.3. This

gives

$$\tilde{M}_{\perp}(\mathbf{r},T) = i\gamma M_0 \int_0^T \tilde{B}_1(\mathbf{r},t)\, e^{-i\gamma \mathbf{r}\cdot\int_t^T \mathbf{G}(\tau)\,\mathrm{d}\tau}\,\mathrm{d}t \tag{2.4}$$

where a linear dependence of the resulting transverse magnetization on the RF pulse magnitude is readily identified. If we define the time integral of the gradient waveform as $\mathbf{k}(t)$:

$$\mathbf{k}(t) = -\gamma \int_t^T \mathbf{G}(\tau)\,\mathrm{d}\tau \tag{2.5}$$

Eq. 2.4 can be rewritten as

$$\tilde{M}_{\perp}(\mathbf{r},T) = i\gamma M_0 \int_0^T \tilde{B}_1(\mathbf{r},t)\, e^{i\mathbf{r}\cdot\mathbf{k}(t)}\,\mathrm{d}t \tag{2.6}$$

The definition of $\mathbf{k}(t)$ in Eq. 2.5 is similar to that of the reception k-space trajectory, the latter being defined as $\mathbf{k}_{\mathrm{r}}(t) = \gamma \int_0^t \mathbf{G}_{\mathrm{r}}(\tau)\,\mathrm{d}\tau$ (where $\mathbf{G}_{\mathrm{r}}(t)$ is the applied gradient waveform during MR signal acquisition). The main difference between the two definitions is the different time integral limits.

Note that although it is derived in the small tip angle regime, Eq. 2.6 is also an acceptable approximation to Bloch equations for large flip angles when certain k-space trajectories are considered [56]. All multidimensional RF pulses shown in the present study were calculated for small flip angle targets, thus based on Eq. 2.6.

As shown in Ref. [16], when transmit B1 field is independent of space, appropriate mathematical manipulations can transform the time integral in Eq. 2.6 into its equivalent with integration with respect to $\mathbf{k}(t)$, showing that the RF pulse and the resulting transverse magnetization form a Fourier transform pair. In this case, $\mathbf{k}(t)$ defines a path in the spatial frequency space (or k-space) and is called the excitation k-space trajectory.

In excitation RF pulse design, the goal is to find an RF pulse that will achieve a desired transverse magnetization distribution. In the small tip angle regime, based on the Fourier relation between the RF pulse and resulting excitation pattern, the required RF waveform can be calculated by the inverse Fourier transform of the desired magnetization distribution. For example, 1D slice selection excitation with a rectangular slice profile is typically obtained using a sinc shaped RF pulse because the Fourier transform of a sinc function gives a rectangular distribution (we deliberately ignore truncation issues in this part of the discussion). During this slice excitation RF pulse,

a linear gradient is applied. Naturally, although a well defined slice profile can be obtained using such 1D slice selective RF pulses, a nonuniform excitation (i.e. flip angle) distribution will result *within* the excitation plane if the in-plane transmit B1 field is inhomogeous, which is a typical issue at high magnetic field.

This in-plane transmit B1 inhomogeneity can be addressed using multidimensional RF pulses (2D in the current case). However, due to limited gradient system capability, those RF pulses typically require a long duration (up to several tens of milliseconds), which makes them impractical due to spin transverse relaxation, amplitude of static field B0 inhomogeneity, and cumulative gradient errors. These problems are even more pronounced at very high field due to larger B0 nonuniformity and shorter transverse relaxation time constants. It has been shown that these limitations can be overcome using parallel transmission techniques, allowing for short, accelerated, selective RF pulses. These accelerated RF pulses are especially promising at very high field where transmit B1 profiles are significantly heterogeneous.

2.4 Parallel Transmission

As previously discussed, traditional multidimensional spatially selective RF pulses with a single transmit channel are typically very long and thus are impractical, especially for high field MR. Fortunately, the concept of parallel imaging using multiple receive channels for accelerated acquisition can be transferred to the transmission side for accelerated excitation.

2.4.1 Acceleration with Sensitivity Encoding

On the receive side, using coil receive sensitivities allows to undersample the receive k-space which can substantially reduce the total acquisition time [22, 23]. Similarly, using coil transmit sensitivities in excitation allows to undersample the excitation k-space, thus to decrease the total RF transmit time [20, 21].

In parallel transmission, the distinct transmit B1 sensitivity profiles of multiple RF coils are explicitly used to design a different RF pulse for each channel, and these calculated RF pulses are played out simultaneously through their corresponding channel. By making use of the spatial encoding information provided by the spatial variations of

individual coil sensitivities, some degree of k-space information can be skipped during RF excitation. The corresponding undersampled k-space results in a shortened RF pulse. As can be expected, when the k-space is undersampled, each of the parallel transmit RF pulses, if applied alone, would result in aliasing artifacts in the excitation pattern. However, when all pulses are played out together, those aliasing artifacts are cancelled out (see Fig. 3.7 for an example).

At high magnetic field, the RF wavelength in biological tissues becomes comparable to or even smaller than the size of anatomical targets. As a result, transmit B1 profiles tend to be more distorted than at low field. This B1 inhomogeneity is one of the critical issues relating with MRI at very high field. At the same time, however, these stronger B1 distortions result in less correlation between the spatial sensitivities of multiple coils, which in turn increases the performance of parallel transmission at high field.

Fig. 2.1 shows a comparison of a single-channel and a multi-channel setup. In the single-channel excitation mode, the same RF waveform is fed into all coil elements. By contrast, in parallel transmission, a different RF waveform is used to drive each of the coil element.

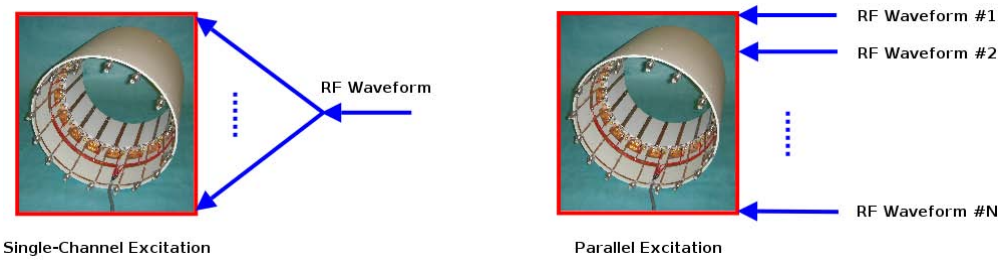

Figure 2.1: Single-channel excitation (left) vs. parallel transmission (right). A 9.4T 16-channel stripline transceiver array is shown for illustration. In the single-channel excitation mode, the same RF waveform is fed into all coil elements. By contrast, in parallel transmission, a different RF waveform is used to drive each of the coil element.

2.4.2 RF Pulse Design

As shown in Eq. 2.6, the complex transverse magnetization of small tip angles is linearly dependent on the applied multidimensional spatially selective B_1 field. In parallel transmission, the effective spatially selective B_1 is a linear, sensitivity-weighted combination

of the applied RF pulses. In this case, the resulting transverse magnetization is given by

$$\tilde{M}(\mathbf{r}) = i\gamma M_0 \int_0^T \sum_{n=1}^{N} \tilde{S}_n(\mathbf{r})\, \tilde{b}_{1,n}(t)\, e^{i\mathbf{r}\cdot\mathbf{k}(t)}\, \mathrm{d}t \tag{2.7}$$

where T is the pulse duration, and N is the number of transmit channels. $\tilde{S}_n(\mathbf{r})$ is the sensitivity profile of the n-th channel on which the RF waveform $\tilde{b}_{1,n}(t)$ is played. $\mathbf{k}(t)$ is the considered k-space trajectory.

Based on this equation, several methods have been proposed to compute the required RF pulse for individual transmit channels to achieve a desired excitation pattern [20, 21, 30, 57]. In this work, we mainly based our pulse design on the spatial domain technique [30] because it provides several advantages over other approaches as will be shown later. Therefore we focus our discussion on the spatial domain method in following paragraphs.

In the spatial domain method, the time and space coordinates of Eq. 2.7 are first discretized over the field of excitation, transforming the continuous equation into an equivalent matrix vector form

$$\tilde{\mathbf{m}} = \sum_{n=1}^{N} \tilde{\mathbf{D}}_n \tilde{\mathbf{A}}\, \tilde{\mathbf{b}}_n \tag{2.8}$$

Here $\tilde{\mathbf{m}}$ is a column vector of the digitalized transverse magnetization values normalized to the whole magnetization amplitude, i.e., $\tilde{m}_u = \tilde{M}(\mathbf{r}_u)/M_0$, $u = 1, 2, \ldots, U$, where $\mathbf{r}_u$ is the u-th location and U is the number of space samples. $\tilde{\mathbf{D}}_n$ is a $U \times U$ diagonal matrix with its diagonal elements being the discretized sensitivities of coil element n, i.e., $\tilde{d}_{(n,(u,u))} = \tilde{S}_n(\mathbf{r}_u)$. $\tilde{\mathbf{A}}$ is a $U \times V$ matrix with its elements being $\tilde{a}_{uv} = i\gamma\, \Delta t\, e^{i\mathbf{r}_u\cdot\mathbf{k}(t_v)}$, $u = 1, 2, \ldots, U$, $v = 1, 2, \ldots, V$, where $\Delta t = T/V$ is the dwell time, t_v is the v-th time point and V is the number of time samples. The vector $\tilde{\mathbf{b}}_n$ with $\tilde{b}_{(n,v)} = \tilde{b}_{1,n}(t_v)$ is the sampled RF pulse for channel n. It is worth pointing out that with this formulation, off-resonance effects can be easily taken into account by introducing an additional exponential term in the definition of matrix $\tilde{\mathbf{A}}$, i.e., $\tilde{a}_{uv} = i\gamma\, \Delta t\, e^{i\mathbf{r}_u\cdot\mathbf{k}(t_v)}\, e^{i\gamma\, \Delta B_0(\mathbf{r}_u)\, (t_v - T)}$ can be used to account for B_0 inhomogeneity or $\Delta B_0(\mathbf{r})$.

In a next step, matrices and vectors are concatenated, allowing the removal of the

explicit summation term in Eq. 2.8. This linear system is now expressed as

$$\tilde{\mathbf{m}} = \begin{bmatrix} \tilde{\mathbf{D}}_1\tilde{\mathbf{A}} & \tilde{\mathbf{D}}_2\tilde{\mathbf{A}} & \dots & \tilde{\mathbf{D}}_N\tilde{\mathbf{A}} \end{bmatrix} \begin{bmatrix} \tilde{\mathbf{b}}_1 \\ \tilde{\mathbf{b}}_2 \\ \vdots \\ \tilde{\mathbf{b}}_N \end{bmatrix} = \tilde{\mathbf{A}}_{\text{full}}\,\tilde{\mathbf{b}}_{\text{full}} \tag{2.9}$$

A great advantage with this formulation is that the problem can now be directly addressed as a standard linear system with numerical analysis softwares such as Matlab. Naturally, Eq. 2.9 can be simply used to calculate the resulting transverse magnetization given the input k-space trajectory and RF pulses. However, in RF pulse design, the excitation pattern, $\tilde{\mathbf{m}}$, is known whereas the RF pulse shapes, $\tilde{\mathbf{b}}_{\text{full}}$, are unknown and the goal is to find appropriate RF pulses capable of generating the desired predefined transverse magnetization distribution. For this purpose which consists of inverting a large size complex matrix, optimization criteria need to be introduced. To calculate parallel transmit RF pulses given a target excitation pattern, one possible minimization problem based on Eq. 2.9 can be formulated as

$$\tilde{\mathbf{b}}_{\text{full,sol}} = \min_{\tilde{\mathbf{b}}_{\text{full}}} \{\, \|\tilde{\mathbf{A}}_{\text{full}}\,\tilde{\mathbf{b}}_{\text{full}} - \tilde{\mathbf{m}}_{\text{des}}\|^2_{(\boldsymbol{\Xi},\boldsymbol{\Upsilon})} + \mathrm{R}(\tilde{\mathbf{b}}_{\text{full}}) \,\} \tag{2.10}$$

where $\tilde{\mathbf{b}}_{\text{full,sol}}$ and $\tilde{\mathbf{m}}_{\text{des}}$ represent the calculated RF pulses and the desired transverse magnetization distribution, respectively. $\mathrm{R}(\tilde{\mathbf{b}}_{\text{full}})$ is a general regularization term used to control the magnitude of the RF. $\boldsymbol{\Xi}$ and $\boldsymbol{\Upsilon}$ are two diagonal matrixes corresponding to a spatial and a temporal mask, respectively. The last three terms are discussed in more details in the next paragraph.

The spatial domain method for parallel transmit RF pulse design formulated in Eq. 2.10 have significant advantages when compared to other approaches. First, it allows the pulse designer to specify a region of interest (ROI), which is a subset of the total field of excitation (FOX), in order to exclude "don't care" regions [30] from pulse calculation. This can be done by incorporating into the problem formulation the diagonal matrix $\boldsymbol{\Xi}$ with $\boldsymbol{\Xi} = \mathrm{diag}(\xi_i)$, $\xi_i \in \{0, 1\}$, $i = 1, 2, \dots, U$ (here 0 is for don't care regions and 1 for ROI). Considering only the ROI in the pulse calculation (instead of the whole FOX) weakens the constraints imposed on the resulting RF pulses and thus leads to improved RF performance within the ROI. Second, the spatial domain

method brings a possibility to define segmented RF pulses during the continuous k-space traversal by introducing the diagonal matrix $\boldsymbol{\Upsilon}$ with $\boldsymbol{\Upsilon} = \mathrm{diag}(\upsilon_i)$, $\upsilon_i \in \{0, 1\}$, $i = 1, 2, \ldots, NV$ (here 0 is for RF off and 1 for RF on). This feature can be very useful in some cases; for example, when using an echo planar trajectory for pulse design, one may want to specify a temporal mask to apply RF pulses only during the readout gradient plateaus, but not during the ramps, in order to minimize eddy current effects. As discussed earlier, the spatial domain method for RF pulse design also provides an easy way to include B_0 inhomogeneity in pulse calculation and thus can be used to correct for off-resonance effects. Finally, it allows to introduce regularizations to control integrated RF power using $\mathrm{R}(\tilde{\mathbf{b}}_{\mathrm{full}}) = \beta \tilde{\mathbf{b}}_{\mathrm{full}}^{\dagger} \boldsymbol{\Upsilon} \tilde{\mathbf{b}}_{\mathrm{full}}$, or to suppress peak RF power using $\mathrm{R}(\tilde{\mathbf{b}}_{\mathrm{full}}) = \tilde{\mathbf{b}}_{\mathrm{full}}^{\dagger} \boldsymbol{\Lambda} \boldsymbol{\Upsilon} \tilde{\mathbf{b}}_{\mathrm{full}}$. Here, β is the Tikhonov regularization parameter and the dagger indicates a conjugate transpose. $\boldsymbol{\Lambda}$ with $\boldsymbol{\Lambda} = \mathrm{diag}(\lambda_i)$, $i = 1, 2, \ldots, NV$, is a diagonal matrix containing a different regularization parameter for each of the time samples in the full RF vector. To the best of our knowledge, those advantages, except for Tikhonov regularization, are not available with the frequency domain method, initially introduced in the seminal Transmit SENSE paper [20]. For these reasons, the spatial domain method was used in this work for pulse design.

In this work, we primarily designed 2D parallel transmit pulses which were used to accomplish a desired 2D excitation pattern defined within a particular axial slice of the scanned object. For this, we predefined 2D k-space trajectories, obtained 2D transmit B1 sensitivity profiles and formulated the minimization problem without explicit regularization terms (i.e., $\min \|\tilde{\mathbf{A}}_{\mathrm{full}} \tilde{\mathbf{b}}_{\mathrm{full}} - \tilde{\mathbf{m}}_{\mathrm{des}}\|^2_{(\boldsymbol{\Xi}, \boldsymbol{\Upsilon})}$) for 2D pulse calculations. To solve the minimization problem, we used the conjugate gradient algorithm which, as will be discussed later, involves implicit regularization effects.

2.4.3 3D Pulse Design Using Spoke Trajectories

Before discussing 3D pulse design with spoke k-space trajectories, we will briefly compare 2D and 3D parallel transmission. In 2D parallel transmission, 2D gradient waveforms or k-space trajectories are utilized to calculate 2D selective RF pulses that, by definition, only achieve a selective excitation along two dimensions without selectivity along the third dimension. For example, a 2D RF pulse designed to achieve a 2D circular target within a particular slice of the object will actually excite a 3D cylindrical volume. In

3D parallel transmission, 3D gradient waveforms are designed to calculate RF pulses that are selective along three dimensions.

According to Eq. 2.7, 3D parallel transmit RF pulses can calculated based on a 3D target excitation pattern, a 3D k-space trajectory and the 3D transmit B1 sensitivity map of each transmit coil element. A major issue with 3D trajectories that would achieve a similar spatial resolution along the three dimensions is their very long duration, even if some degree of RF pulse acceleration were to be used. This very long duration is the main reason why such pulses are almost never used in practice. There is however a useful and very practical situation which does not require high spatial frequencies for the excitation pattern in all three dimensions, which consists of targeting a homogeneous excitation profile through an entire 2D slice (or slab) of tissue, rather than eliciting high spatial frequency patterns such as in-plane square or checkerboard shapes that are commonly chosen to demonstrate parallel transmission performances. A fundamental characteristic of RF coil transmit B1 profiles is that, even though they are highly heterogeneous at very high field, their pattern is still typically relatively smooth, without significant high spatial frequency contribution. Furthermore, assuming a limited slice (or slab) thickness, transmit B1 variations through slice (or slab) are typically very limited, especially when the slice (or slab) selective direction is along the z axis. The fact that low spatial frequencies (thus low k-space values) are sufficient to achieve a reasonably homogeneous excitation profile through a slice makes it possible to use so-called "spoke" trajectories where only a few points in a k-space plane are sufficient to shape an acceptably uniform excitation profile. In this scheme, high spatial frequencies (i.e. high k-space values) are only required along the slice (or slab) selection dimension.

In practice, multi channel RF coils transmit elements are most often distributed about the z axis, which is also the case in our current settings. As a result, the natural targets for spoke trajectory based B1 mitigation consist of axial slices or slabs where spokes are defined in the xy k-space whereas slice or slab selection gradient is applied along the z axis. In this case, the 3D pulse design problem can be separated into a 1D and a 2D pulse design if three assumptions are further made as follows.

- The desired magnetization profile is separable, i.e., $M(x, y, z) = P(z) \cdot Q(x, y)$.

Here $P(z)$ represents the transverse magnetization distribution along z and typically reflects the slice or slab profile. $Q(x, y)$ is the transverse magnetization distribution within the xy plane.

- Flip angles are always small during the RF pulse.
- A 3D spoke trajectory (see Fig. 2.2 for examples) is used for pulse design.

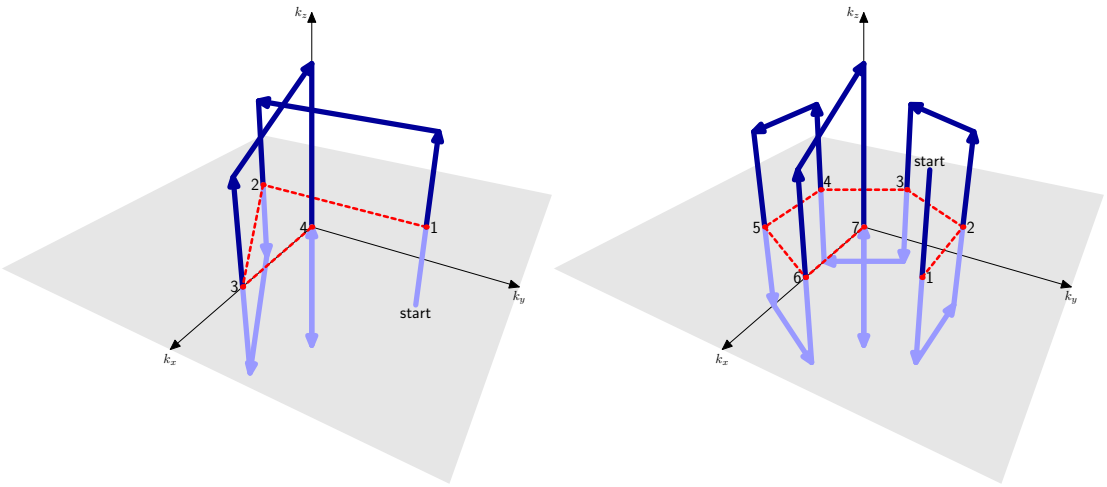

Figure 2.2: Examples of 3D spoke trajectories for a 4-spoke design (left) and a 7-spoke design (right). A 3D spoke trajectory consists of a number of spokes that are perpendicular to the transverse plane in k-space and transition segments within the transverse plane connecting two spokes. The red dashed line shows the projection of the 3D trajectory into the transverse plane. The numbers indicate in which order the spokes will be traversed.

In this separable pulse design, the 1D pulse design actually consists of an RF subpulse that will be applied during each spoke of the trajectory and will accomplish the desired slice or slab selection. This subpulse typically makes use of standard slice selective RF pulse shape (e.g. sinc pulse).

In order to compensate for in-plane B1+ inhomogeneity, different sets of RF amplitudes and phases need to be applied to the subpulse during each spoke. In addition, for the same spoke, the RF phase and amplitude modulation differs between channels. Thus, the 2D pulse design consists of finding appropriate RF amplitude and phase modulation (or weights). Once the RF subpulse and the weights are calculated, the final

RF pulse for each coil element will be obtained by assembling all weighted subpulses.

Practically, the separable pulse design consists of three steps. First, a subpulse $\tilde{b}_{1,\text{sub}}(t)$ is designed to generate a slice or a slab selection specified by $P(z)$. This subpulse can be any of the traditional slice or slab selective RF pulses, e.g., gaussian, sinc and SLR.

Second, the number of spokes and the spoke placement are determined, and different weights for different spokes and coil elements are calculated based on an optimization problem [27, 58]. Formulated in a way similar to that of Eq. 2.10, the optimization problem can be the least squares minimization

$$\tilde{\mathbf{w}}_{\text{full,sol}} = \min_{\tilde{\mathbf{w}}_{\text{full}}} \{ \|\tilde{\mathbf{A}}_{\text{full}}\, \tilde{\mathbf{w}}_{\text{full}} - 1\|_2^2 \} \tag{2.11}$$

with

$$\tilde{\mathbf{A}}_{\text{full}} = \begin{bmatrix} \tilde{\mathbf{D}}_1\tilde{\mathbf{A}} & \tilde{\mathbf{D}}_2\tilde{\mathbf{A}} & \dots & \tilde{\mathbf{D}}_N\tilde{\mathbf{A}} \end{bmatrix}$$

$$\tilde{\mathbf{w}}_{\text{full}} = \begin{bmatrix} \tilde{\mathbf{w}}_1 \\ \tilde{\mathbf{w}}_2 \\ \vdots \\ \tilde{\mathbf{w}}_N \end{bmatrix}$$

where N is the number of coil elements. $\tilde{\mathbf{D}}_n$ is a diagonal matrix with $\tilde{d}_{(n,(u,u))} = \tilde{S}_n(x_u, y_u)$, $u = 1, 2, \dots, U$, here $\tilde{S}_n(x_u, y_u)$ is the transmit B1 sensitivity of the u-th space sample located at (x_u, y_u). $\tilde{\mathbf{A}}$ with $\tilde{a}_{um} = e^{i\,(x_u \cdot k_{x,m} + y_u \cdot k_{y,m})}\, e^{i\gamma\,\Delta B_0(x_u,y_u)\,(t_m - T)}$, $u = 1, 2, \dots, U$, $m = 1, 2, \dots, M$, is a matrix involving the spoke placements, and if applicable, the ΔB_0 map, here M is the number of spokes, $(k_{x,m}, k_{y,m})$ and t_m are respectively the placement of and the end time of the m-th spoke. $\tilde{\mathbf{w}}_n = [\tilde{w}_{n,1}, \tilde{w}_{n,2}, \dots, \tilde{w}_{n,M}]^{\text{T}}$ is a column vector containing a different weight for each of the spokes for element n.

Finally, the final RF pulse for the n-th coil element is assembled with a sequence of time shifted and weighted subpulses

$$\tilde{b}_{1,n}(t) = \sum_{m=1}^{M} \tilde{w}_{n,m} \tilde{b}_{1,\text{sub}}(t - (m-1)T_{\text{sub}}) \tag{2.12}$$

where T_{sub} is the duration of the subpulse $\tilde{b}_{1,\text{sub}}(t)$.

Note that although the formulation above applies for parallel transmission, 3D pulse design using spoke trajectories can also be applied to single-channel excitation to create

a slice or slab selective excitation with mitigated in-plane transmit B1 inhomogeneity. However, 3D pulse design with a single transmit channel will require a large number of spokes to be placed in k-space in order to achieve sufficient transmit B1 homogenization, resulting in too long RF pulses which cannot be used for clinical applications at high field. By contrast, parallel transmit pulse design taking the advantage of the coil sensitivity encoding only requires a few spokes to create homogeneous RF excitation, giving rise to much shortened and clinically usable RF pulses. In other words, the acceleration process gained with parallel transmission consists hereby of a reduction of the number of spokes.

2.5 RF Power Deposition

When transmitting a radiofrequency (RF) electromagnetic field to excite nuclear spins (e.g., proton) to perform MR imaging with human subjects, RF energy will be deposited in the body as heat. The RF power dissipation has been shown to increase with increasing magnetic fields [1, 59–61]. Therefore, for high and ultrahigh field MR, the safety issue associated with the high RF power deposition is a constant concern and should be carefully considered.

2.5.1 Specific Absorption Rate

The specific absorption rate (SAR), defined as the RF power absorbed per mass of tissues, has been used in MR imaging to measure the rate at which RF energy is absorbed by the body when exposed to a RF waveform. The SAR at a certain location and a certain time $\mathrm{SAR}(\mathbf{r}, t)$ can be calculated using the electric field and body tissue properties [62, 63]

$$\mathrm{SAR}(\mathbf{r}, t) = \frac{\sigma(\mathbf{r})}{2\rho(\mathbf{r})} \tilde{\mathbf{E}}(\mathbf{r}, t) \cdot \tilde{\mathbf{E}}(\mathbf{r}, t)^* \tag{2.13}$$

where σ and ρ are the conductivity and mass density of the tissue, respectively. The vector $\tilde{\mathbf{E}}$ represents the RF related electric field. The asterisk indicates a complex conjugate.

In the case of parallel transmission, the electric field as a function of time and space $\tilde{\mathbf{E}}(\mathbf{r}, t)$ will be the superposition of individual electric fields from multiple transmit channels, each defined as the input RF pulse $\tilde{b}_{1,n}(t)$ weighted by the electric field sensitivity

$\tilde{\mathbf{E}}_{0,n}(\mathbf{r})$:

$$\tilde{\mathbf{E}}(\mathbf{r},t) = \sum_{n=1}^{N} \tilde{\mathbf{E}}_{0,n}(\mathbf{r})\, \tilde{b}_{1,n}(t) \tag{2.14}$$

where N is the number of channels. $\tilde{\mathbf{E}}_{0,n}(\mathbf{r})$ is defined as the unit current generated electric field of coil n for a given load. $\tilde{b}_{1,n}(t)$ is the RF waveform applied on channel n. The averaged SAR over the RF pulse can be obtained using the time integration of SAR divided by the pulse duration T

$$\begin{aligned} \mathrm{SAR}(\mathbf{r}) &= \frac{1}{T}\int_0^T \mathrm{SAR}(\mathbf{r},t)\,\mathrm{d}t \\ &= \frac{\sigma(\mathbf{r})}{2\rho(\mathbf{r})\,T}\int_0^T \left(\sum_{n=1}^{N} \tilde{\mathbf{E}}_{0,n}(\mathbf{r})\,\tilde{b}_{1,n}(t)\right) \\ &\cdot \left(\sum_{n=1}^{N} \tilde{\mathbf{E}}_{0,n}(\mathbf{r})\,\tilde{b}_{1,n}(t)\right)^{*} \mathrm{d}t \end{aligned} \tag{2.15}$$

This equation has been used as the basis for all SAR computations in this work.

As can be seen in Eq. 2.15, the electric field map of individual channels (due to a unit current), along with tissue property distributions, is required to calculate the resulting SAR of the input RF pulses. Since electric field maps cannot be measured on the fly for each individual during MR experiments, electromagnetic simulations need to be performed. So far only off-scanner simulations are run to estimate the distribution of electric fields because the duration of such calculations as of today is completely prohibitive for real time results. All our SAR related computations have been based on the finite difference time domain (FDTD) modelling as briefly introduced next.

2.5.2 Finite Difference Time Domain Modelling

Finite difference time domain (FDTD) is a widely used method for computational electrodynamics. In this technique, the time dependent Maxwell's equations are discretized with respect to the space and time partial derivatives, and the resulting finite difference equations are solved for the electric and magnetic field vectors in a leapfrog manner until residual variations between subsequent iterations are smaller than a user defined threshold [64]. Note that either a transient or a steady-state electromagnetic field behavior can be obtained. In our case, only steady state solutions were considered.

The computational domain in which FDTD simulations are established is generally constructed with a number of so called Yee cells [64]. A standard cartesian Yee cell is illustrated in Fig. 2.3. As can be seen, electric field components constitute the edges of the cell, and magnetic field components form the normals to the faces of the cell. In addtion, each of the cells within the computational domain is assigned appropriate values of permittivity to each electric field component and permeability to each magnetic field component.

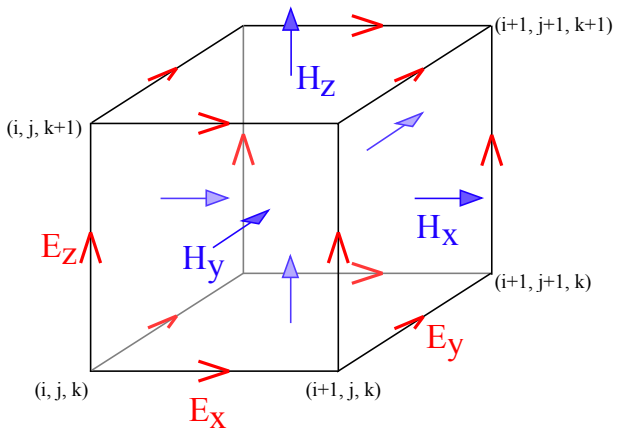

Figure 2.3: Illustration of a standard cartesian Yee cell used for FDTD, showing how electric and magnetic field vector components are defined (Courtesy of Wikipedia).

In this work, we performed our FDTD simulations using a commercial FDTD software (Remcom Inc., PA, USA). A number of multi-element RF stripline arrays, loaded with a human head model, were modelled for 7 T and 9.4 T. The human head model is constructed based on the image data provided by the Visible Human Project [1] . The head model is defined on an overall mesh of $309 \times 117 \times 161$ Yee cells with $2 \times 2 \times 2.5\,\mathrm{mm}^3$ resolution and is composed of 17 tissues with appropriate values of permittivity, conductivity and mass density assigned to the edges of the cell.

In order to calculate the SAR distribution for parallel transmission, a SAR calculator was written in Matlab. SAR values are computed for individual Yee cells following the same approach as in the Remcom software (Remcom Inc., PA, USA). Based on Eq. 2.15, SAR values are first obtained for each of the 12 electric field components on the edges of

[1] http://www.nlm.nih.gov/

a cell. Those 12 SAR numbers are then averaged to determine the SAR value assigned to the cell. Note that only voxels without null conductivity or null mass density are included in the calculation and all other voxels are masked out. The SAR calculator is written considering the following inputs: spatial distribution of tissue conductivity and mass density, complex electric field profile of each transmit coil and temporal complex RF pulse shape for each transmit coil element. Note that these calculations could not be obtained with the Remcom software which does not allow for defining temporal RF shape pulses or multiple RF inputs with different temporal shapes.

2.6 Bloch Simulation

A Bloch simulator, based on Rodrigues' rotation matrixes [2] , was developed in Matlab to numerically simulate the time evolution of the magnetization during a RF pulse. The simulator models the effective magnetic field as a sequence of hard subpulses with a constant time interval and sums an array of subrotations of magnetization due to each of the hard subpulses to approximate the total magnetization rotation in the rotating frame. Detailed simulation procedures are outlined below.

First, at a given location $\mathbf{r}$ the effective magnetic field is calculated for each time point t_i, $\mathbf{B}_{\text{eff}}(\mathbf{r}, t_i) = B_{\text{eff},x}(\mathbf{r}, t_i)\,\hat{\boldsymbol{x}} + B_{\text{eff},y}(\mathbf{r}, t_i)\,\hat{\boldsymbol{y}} + B_{\text{eff},z}(\mathbf{r}, t_i)\,\hat{\boldsymbol{z}}$. The z component arising from the gradient waveform $\mathbf{G}(t)$ is calculated with $B_{\text{eff},z}(\mathbf{r}, t_i) = \mathbf{G}(t_i) \cdot \mathbf{r}$. The complex transverse magnetic field due to the RF pulse is obtained by $\tilde{B}_1(\mathbf{r}, t_i) = \sum_{n=1}^{N_c} \tilde{S}_n(\mathbf{r})\,\tilde{b}_{1,n}(t_i)$, where N is the number of transmit channels, $\tilde{S}_n(\mathbf{r})$ and $\tilde{b}_{1,n}(t_i)$ are the transmit B1 sensitivity map and the RF pulse, respectively, for channel n. The real part of the obtained complex magnetic field is assigned to $B_{\text{eff},x}$, and the imaginary part is to $B_{\text{eff},y}$.

Second, an array of subrotations of magnetization are calculated based on Rodrigues' rotation formula. Within each time interval ($\Delta t = t_{i+1} - t_i$), the magnetization vector $\mathbf{M}(t_i)$ is assumed to rotate about a constant magnetic field $\mathbf{B}_{\text{eff}}(t_i)$ at an angle of $\theta_i = \gamma \left\|\mathbf{B}_{\text{eff}}(t_i)\right\| \Delta t$, where γ is the gyromagnetic ratio. With the unit vector $\hat{\boldsymbol{\omega}}_i = [\,\hat{\omega}_x^i, \hat{\omega}_y^i, \hat{\omega}_z^i\,]^{\mathrm{T}}$ specifying the fixed direction of the vector $\mathbf{B}_{\text{eff}}(t_i)$, the corresponding

[2] http://mathworld.wolfram.com/ RodriguesRotationFormula.html

3×3 rotation matrix is calculated with

$$\mathbf{R}_i = \mathbf{I}_3 + \mathbf{\Omega}_i \sin\theta_i + \mathbf{\Omega}_i^2 (\, 1 - \cos\theta_i \,)$$

where $\mathbf{I}_3$ is the 3×3 identity matrix and $\mathbf{\Omega}_i$ is an antisymmetric matrix

$$\mathbf{\Omega}_i = \begin{bmatrix} 0 & -\hat{\omega}_z^i & \hat{\omega}_y^i \\ \hat{\omega}_z^i & 0 & -\hat{\omega}_x^i \\ -\hat{\omega}_y^i & \hat{\omega}_x^i & 0 \end{bmatrix}$$

Then, the final magnetization vector is obtained by the initial magnetization vector multiplied by a series of rotation matrices, i.e., $\mathbf{M}(T) = (\prod_{i=V}^{1} \mathbf{R}_i)\, \mathbf{M}_0$. Here T is the pulse duration, $\prod$ is the multiplication operator, V is the number of time points, and $\mathbf{M}_0$ is the initial magnetization vector.

Finally, the abovementioned steps are repeated for all pixels within the region of interest.

Note that the current simulator does not account for relaxation or diffusion effects since those effects are expected to be small as a result of the short RF pulse in parallel transmission.

2.7 Regularization Methods

As will be shown later, the system matrix associated with parallel transmit RF pulse design (e.g. $\tilde{\mathbf{A}}_{\text{full}}$ in Eq. 2.9) is in general ill-conditioned. Using the related least squares problem for pulse calculation leads to a discrete ill-posed problem which is essentially underdetermined due to the cluster of small singular values of the system matrix. Therefore, regularization methods are required in order to calculate a useful and stable solution.

Here we first discuss the singular value decomposition of a matrix which helps to understand the difficulties associated with a discrete ill-posed problem. We then briefly introduce the Tikhonov regularization [65, 66] and the conjugate gradient iterations [67, 68] that can be used to obtain a reliable solution of parallel transmit pulses. We finally present the L-curve criterion [25, 69, 70] which is used to choose the regularization parameter.

2.7.1 Singular Value Decomposition

Let's consider $\mathbf{A} \in \mathcal{R}^{M\times N}$ to be a rectangular or square matrix and assume for ease of presentation that $M \geq N$. Then the singular value decomposition (SVD) of $\mathbf{A}$ is given by [71]

$$\mathbf{A} = \mathbf{U}\,\mathbf{\Sigma}\,\mathbf{V}^{\mathrm{T}} = \sum_{i=1}^{N} \mathbf{u}_i\,\sigma_i\,\mathbf{v}_i^{\mathrm{T}} \tag{2.16}$$

where $\mathbf{U} = (\mathbf{u}_1, \ldots, \mathbf{u}_N) \in \mathcal{R}^{M\times N}$ and $\mathbf{V} = (\mathbf{v}_1, \ldots, \mathbf{v}_N) \in \mathcal{R}^{N\times N}$ are matrices with orthonormal columns, i.e., $\mathbf{U}^{\mathrm{T}}\mathbf{U} = \mathbf{V}^{\mathrm{T}}\mathbf{V} = \mathbf{I}$. The symbol T denotes matrix transpose. $\mathbf{\Sigma} = \mathrm{diag}(\sigma_1, \ldots, \sigma_N)$ is a diagonal matrix with its non-negative diagonal elements in non-increasing order, $\sigma_1 \geq \sigma_2 \geq \cdots \geq \sigma_N \geq 0$. The numbers σ_i are called the singular values of matrix $\mathbf{A}$, and the vectors $\mathbf{u}_i$ and $\mathbf{v}_i$ are the left and right singular vectors. In the case where $M < N$, simply apply SVD to $\mathbf{A}^{\mathrm{T}}$ and interchange $\mathbf{U}$ and $\mathbf{V}$. The minimization problem characterized by a system matrix $\mathbf{A}$ may be thought of as a discrete ill-posed problem when the SVD of $\mathbf{A}$ has two characteristic features [71]:

- The singular values (σ_i) decay gradually to zero.
- The left and right singular vectors ($\mathbf{u}_i$ and $\mathbf{v}_i$) tend to have more sign changes in their elements as the index i increases, or equivalently, as σ_i decreases.

To explain why those two features of the system matrix indicate a discrete ill-posed problem, the least squares problem is considered. The least squares problem is formulated as

$$\min_{\mathbf{x}} \|\mathbf{A}\mathbf{x} - \mathbf{b}\|_2^2 \tag{2.17}$$

Solving this is equivalent to solving the following linear equations

$$\mathbf{A}^{\mathrm{T}}\,\mathbf{A}\,\mathbf{x} = \mathbf{A}^{\mathrm{T}}\,\mathbf{b} \tag{2.18}$$

If $\mathbf{A}^{\mathrm{T}}\,\mathbf{A}$ is invertible (i.e., $(\mathbf{A}^{\mathrm{T}}\,\mathbf{A})^{-1}$ exists), we have

$$\mathbf{x} = \mathbf{A}^{\dagger}\,\mathbf{b} = (\mathbf{A}^{\mathrm{T}}\,\mathbf{A})^{-1}\,\mathbf{A}^{\mathrm{T}}\,\mathbf{b} \tag{2.19}$$

Replacing $\mathbf{A}$ with its SVD then yields

$$\mathbf{x} = \sum_{i=1}^{N} \frac{\mathbf{u}_i^{\mathrm{T}}\mathbf{b}}{\sigma_i}\,\mathbf{v}_i \tag{2.20}$$

The term $\mathbf{A}^{\dagger} = (\mathbf{A}^{\mathrm{T}}\,\mathbf{A})^{-1}\,\mathbf{A}^{\mathrm{T}}$ is referred to as the pseudoinverse [68] of matrix $\mathbf{A}$.

It can be seen from Eq. 2.20 that the coefficient $\mathbf{u}_i^{\mathrm{T}}\,\mathbf{b}$ is inversely proportional to the singular value σ_i. Therefore, when $\mathbf{A}$ has very small singular values or the problem is ill-posed, the inversion amplifies those coefficients corresponding to small singular values. If $\mathbf{b}$ involves noise (which is almost always true in the real world), the solution will be dominated by those terms of the smallest σ_i contaminated with amplified noises. As a result, the solution has many sign changes and appears to be random. Therefore, to obtain a stable solution (or a solution that is insensitive to noise), regularization is desired.

2.7.2 Tikhonov Regularization

Tikhonov regularization may be the most common and well-known form of regularization. With Tikhonov regularization, we have the minimization problem [71]

$$\min_{\mathbf{x}}\{\,\|\mathbf{A}\mathbf{x}-\mathbf{b}\|_2^2+\lambda^2\|\mathbf{x}\|_2^2\,\} \tag{2.21}$$

where $\mathbf{A}\in\mathcal{R}^{M\times N}$ is the system or coefficient matrix, and λ is the regularization parameter. This is equivalent to solving

$$\min_{\mathbf{x}}\left\|\begin{bmatrix}\mathbf{A}\\ \lambda\mathbf{I}\end{bmatrix}\mathbf{x}-\begin{bmatrix}\mathbf{b}\\ 0\end{bmatrix}\right\|_2 \tag{2.22}$$

where $\mathbf{I}$ represents the identity matrix. If the null spaces of $\mathbf{A}$ and $\mathbf{I}$ in Eq. 2.22 intersect trivially such that the new coefficient matrix (composed of $\mathbf{A}$, $\mathbf{I}$ and λ) has full rank, a unique Tikhonov solution can be found and is given by

$$\mathbf{x}_\lambda = (\mathbf{A}^{\mathrm{T}}\mathbf{A}+\lambda^2)^{-1}\mathbf{A}^{\mathrm{T}}\,\mathbf{b} \tag{2.23}$$

Replacing $\mathbf{A}$ with its SVD (Eq. 2.16) provides

$$\mathbf{x}_\lambda = \sum_{i=1}^{N} f_i\frac{\mathbf{u}_i^{\mathrm{T}}\mathbf{b}}{\sigma_i}\,\mathbf{v}_i \tag{2.24}$$

with

$$f_i = \sigma_i^2/(\sigma_i^2+\lambda^2)$$

where the numbers f_i are filter factors. Note that $f_i \approx 1$ when $\sigma_i \gg \lambda$, whereas $f_i \to 0$ when $\lambda \gg \sigma_i \to 0$.

Comparing the regularized solution (Eq. 2.24) to the unregularized solution (Eq. 2.20), one can see that the contributions of the large singular values are almost retained in the regularized solution since their filter factors are close to unity. However, the contributions of the smallest singular values are filtered out in the regularized solution due to the corresponding small filter factors. Without those contributions contaminated with amplified noise, a stable solution can be obtained.

The regularization parameter λ defining the filter factor controls the filtering behavior of Tikhonov regularization. Indeed, a too large λ results in an overregularized solution with large residual errors (i.e., large $\|\mathbf{A}\mathbf{x}_\lambda - \mathbf{b}\|_2$), whereas a too small λ gives rise to an unregularized solution with large solution norm (i.e. large $\|\mathbf{x}_\lambda\|$). Therefore, the choice of the regularization parameter is crucial for obtaining a good solution that balances between the residual error and the solution norm.

2.7.3 Conjugate Gradient Iterations

The conjugate gradient (CG) algorithm is a well-known iterative method originally designed for solving sparse systems associated with a symmetric positive definite coefficient matrix. Here we briefly present one implementation of CG iterations that we found providing very stable results, including with experimental data. Applied on the system described in Eq. 2.18, this implementation consists of five consecutive statements in each of the iterations. The k-th step is given by [71]

$$\begin{aligned} \alpha_k &= \|\mathbf{A}^{\mathrm{T}}\mathbf{r}^{(k-1)}\|_2^2 \,/\, \|\mathbf{A}\,\mathbf{d}^{(k-1)}\|_2^2 \\ \mathbf{x}^{(k)} &= \mathbf{x}^{(k-1)} + \alpha_k\,\mathbf{d}^{(k-1)} \\ \mathbf{r}^{(k)} &= \mathbf{r}^{(k-1)} - \alpha_k\,\mathbf{A}\,\mathbf{d}^{(k-1)} \\ \beta_k &= \|\mathbf{A}^{\mathrm{T}}\mathbf{r}^{(k)}\|_2^2 \,/\, \|\mathbf{A}^{\mathrm{T}}\mathbf{r}^{(k-1)}\|_2^2 \\ \mathbf{d}^{(k)} &= \mathbf{A}^{\mathrm{T}}\mathbf{r}^{(k)} + \beta_k\,\mathbf{d}^{(k-1)} \end{aligned} \tag{2.25}$$

where $\mathbf{r}^{(k)} = \mathbf{b} - \mathbf{A}\mathbf{x}^{(k)}$ is the residual vector, and $\mathbf{d}^{(k)}$ is an auxiliary vector of length N. Initialized with a starting vector $\mathbf{x}^{(0)}$, the algorithm first calculates $\mathbf{r}^{(0)} = \mathbf{b} - \mathbf{A}\mathbf{x}^{(0)}$ and $\mathbf{d}^{(0)} = \mathbf{A}^{\mathrm{T}}\mathbf{r}^{(0)}$, and then proceeds to execute the iterations until certain criteria are met.

It is important to note that even when an unregularized system (e.g., Eq. 2.18) is considered, using the CG method actually implicitely regularizes the solution. This is explained by the fact that during the CG iterations, the low-frequency components of the solution tend to converge faster than the high-frequency components. In this context, therefore, the number of iterations plays the role of the regularization parameter.

In this work, we utilized the CG iterations to calculate all 2D parallel transmit RF pulses. The CG algorithm, based on iterations, does not need to perform SVD on the system matrix and thus is much faster than Tikhonov regularization since the system matrix associated with parallel transmit pulse design is typically of a fairly large size and its SVD is time consuming. The number of iterations was determined using the L-curve criterion as will be discussed later.

2.7.4 L-Curve Analysis

The L-curve has been shown to be the most convenient graphical tool for analysis of discrete ill-posed problems. As described in Ref. [71], it consists of the plot of the norm of the regularized solution, $\|\mathbf{x}_{\text{reg}}\|_2$ versus the norm of the residual error $\|\mathbf{A}\mathbf{x}_{\text{reg}} - \mathbf{b}\|_2$. Therefore, the L-curve clearly displays the compromise between the minimizations of these two quantities, which is the heart of any regularization method.

For discrete ill-posed problems, the L-curve, mostly has a characteristic L-shaped appearance with a distinct corner. This corner separates the vertical and the horizontal parts of the curve. The vertical part of the L-curve corresponds to solutions where $\|\mathbf{x}_{\text{reg}}\|_2$ is very sensitive to changes of the regularization parameter. The horizontal part of the L-curve corresponds to solutions where the residual norm $\|\mathbf{A}\mathbf{x}_{\text{reg}} - \mathbf{b}\|_2$ is most sensitive to the regularization parameter.

For a given $\mathbf{b}$, there exists an optimal regularization parameter that balances $\|\mathbf{x}_{\text{reg}}\|_2$ and $\|\mathbf{A}\mathbf{x}_{\text{reg}} - \mathbf{b}\|_2$. This optimal regularization parameter is close to the regularization parameter that corresponds to the corner of the L-curve. Therefore, an approximation to the optimal regularization parameter can be obtained by locating the corner of the L-curve. Once the optimal regularization parameter is chosen, a regularized solution with a good balance between the two norms can be computed.

In this work, the L-curve was used to determine the regularization parameter for the minimization problem of parallel transmit RF pulse design. In particular, it was

considered to choose the number of conjugate gradient iterations used for 2D pulse calculation.

2.8 Hardware Setup

All experiments were performed on a 9.4 T (400 MHz for proton), 65-cm inner diameter bore human scanner (Magnex, Oxford, UK) housed in the Center of Magnetic Resonance Research (CMRR) at the University of Minnesota. This scanner is equipped with a head gradient coil capable of a maximum gradient strength of 50 mT/m and maximum slew rate of 166 T/m/s. In addition, the scanner was driven by a DirectDrive console with eight independent Tx RF channels (Varian Inc., Palo Alto, CA, USA), each powered with a 500W RF amplifier (CPC, Brentwood, NY, USA). MR signals were acquired on eight independent receive (Rx) channels with a home built digital receiver system based on Echotek boards (Echotek, Huntsville, AL, USA). All RF coils considered for our parallel transmit experiments are multi-element transceiver arrays which were used for both multi-channel transmit and multi-channel receive. Fig. 2.4 shows a picture of the 9.4 T magnet.

Figure 2.4: Photograph of the 9.4 T human scanner on which all experiments were run.

To ensure compliance with the FDA guidelines on specific absorption rate [3] , an RF power monitoring system was embedded into the transmit chain. It continuously monitors the RF output power of each of the eight RF amplifiers with an in-house-built multi-channel monitoring unit. Each RF amplifier was equipped with a directional coupler providing a 50dB attenuated version of the output waveform whose power envelope was continuously sampled by a calibrated analog-to-digital converter board. The system was maintaining a 10-second and a 10-minute moving average and would immediately disable all RF amplifiers and terminate the MR pulse sequence if the mean power exceeded a predefined wattage threshold. Thresholds were conservatively determined against the worst case scenario assuming all RF coil electric fields to add constructively in the sample.

2.9 Fast Multi-Channel Transmit B_1 Mapping

As seen from previous discussion, parallel transmission cannot be utilized without mapping the transmit B1 (B_1^+) profile of individual RF coil elements. Two serious difficulties arise to map B_1^+ on multiple transmit channels at very high field: time and RF peak power. Traditional B_1^+ mapping techniques such as the double flip angle introduced by Insko et al. [72] require a long acquisition time because they rely on a fully relaxed longitudinal magnetization between subsequent RF pulses in order to avoid T1 induced bias. Even at low spatial resolution such approaches easily require about 5 minutes of acquisition time for a single map. Multiplied by 8 or 16 Tx channels this yields a total time incompatible with a standard MRI session where calibration scans need to be contained within a small fraction of the scanning time. A large number of new, faster B_1^+ mapping techniques have been proposed over the recent years [73–81] to speed up the acquisition process. However, most of these techniques still rely on reaching a large flip angle and require at least a couple of minutes to obtain a 3D or a multislice B_1^+ map, which is appropriate for a single channel but not for 8 or 16 channels. Some of these newly proposed techniques can actually run faster, but these rely either on very high RF peak power, which is always a concern at high field because of SAR levels, or

[3] Criteria for significant risk investigations of magnetic resonance diagnostic devices, U. S. Food and Drug Administration, 2003. http://www.fda.gov/MedicalDevices/DeviceRegulationandGuidance

on ultrafast imaging techniques such as Echo Planar Imaging that require additional corrections for geometric distortion and are especially prone to multiple artifacts when used for targets located in the torso at very high field. Another significant limitation for all single channel at a time B_1^+ mapping techniques, is that each individual transmit channel can be seen as a surface coil with a B_1^+ profile ranging over a much large dynamic range than a volume RF coil. More specifically, for voxels that are far from a given RF coil element reaching a large flip angle would require RF power that would exceed either hardware specifications or acceptable SAR limits. In this section we describe a fast B_1^+ mapping technique [77, 82] for multiple channels where one absolute B_1^+ map obtained in the large flip angle regime is merged with N fast relative B_1^+ maps obtained in the small flip angle regime, where N is the number of transmit channel elements to be mapped. This method was used for all parallel transmit experiments presented in this thesis.

The multi-channel transmit B1 mapping technique used here measures the complex B_1^+ maps for multiple channels as follows. First, it derives relative magnitude and phase B_1^+ maps based on a series of gradient echo (GE) images collected in the small tip angle regime with only one channel transmitting at a time. Second, it acquires one absolute magnitude B_1^+ map in the large tip angle regime with all channels transmitting together. Last, it merges the relative and absolute B_1^+ information to obtain the final complex B_1^+ map for individual channels.

2.9.1 Formalism for Multi-Channel Transmit and Receive

We consider the complex valued signal of a gradient echo (GE) image in steady state. At very high field transmit B1 (B_1^+) and receive B1 (B_1^-) profiles for the same RF coil significantly differ from each other in magnitude and phase [2] and must be identified as separate quantities. Considering K transmit and J receive coils, the complex image signal $\tilde{I}_{j,k}$ obtained in receive coil j ($j = 1, 2, \ldots, J$), when only one transmit coil k ($k = 1, 2, \ldots, K$) is utilized to deliver RF power, is given by

$$\begin{aligned} \tilde{I}_{j,k} &= \tilde{R}_j \cdot \tilde{T}_k \cdot \tilde{C} \\ &= \underbrace{|\tilde{B}_{1,j}^-| e^{i\phi_j}}_{\tilde{R}_j} \cdot \underbrace{\frac{\sin(\alpha_k)\, e^{i\theta_k}}{1 - \cos(\alpha_k)\, E_1}}_{\tilde{T}_k} \cdot \underbrace{M_{z0}\,(1 - E_1)\, E_2^\star\, A e^{iQ}}_{\tilde{C}} \end{aligned} \tag{2.26}$$

with $\alpha_k = V|\tilde{B}^+_{1,k}|\gamma\tau$, $E_1 = e^{-\mathrm{TR}/T_1}$ and $E_2^\star = e^{-\mathrm{TE}/T_2^\star}$. Here $\tilde{B}^-_{1,j}$ and $\tilde{B}^+_{1,k}$ represent the complex receive and transmit B1 vectors, respectively, with receive phase ϕ_j and transmit phase θ_k. M_{z0} reflects proton density. The flip angle α_k is proportional to $|\tilde{B}^+_{1,k}|$ with γ the gyromagnetic ratio, τ the equivalent square pulse duration and V a voltage related scaling factor. Three relevant groups can be identified in Eq. 2.26. $\tilde{R}_j$ is a Receive term dependent on receive coil j, $\tilde{T}_k$ is a Transmit term dependent on transmit coil k, and $\tilde{C}$ is a common term independent of the coils. This common term includes a variety of sources of signal amplitude (A) and phase (Q) variations [83] such as ΔB_0, system noise, etc., which will not be detailed. Note that $\mathbf{r}$ is removed from the notations of space dependent terms for simplicity. As will be seen later, Eq. 2.26 forms the basis of the fast mapping technique.

2.9.2 Relative Phase and Magnitude B_1^+ Mapping

Relative B_1^+ Phase Maps

To calculate relative transmit phases, one transmit channel k_{ref} is chosen as a reference. Here, $k_{\mathrm{ref}} = 1$ is arbitrarily considered. As previously shown [29, 83], all phase terms vanish in the ratio of $\tilde{I}_{j,k}/\tilde{I}_{j,1}$, except for the relative transmit phase, irrespective of signal magnitudes. Denoting by $\Psi_k(j)$ the relative phase of transmit coil k estimated with receive coil j, we have

$$\Psi_k(j) = \arg\left(\frac{\tilde{I}_{j,k}}{\tilde{I}_{j,1}}\right) = \arg\left(\frac{\tilde{R}_j\,\tilde{T}_k\,\tilde{C}}{\tilde{R}_j\,\tilde{T}_1\,\tilde{C}}\right) = \arg\left(\frac{\tilde{T}_k}{\tilde{T}_1}\right) = \arg\left(\frac{e^{i\theta_k}}{e^{i\theta_1}}\right) = \theta_k - \theta_1 \qquad (2.27)$$

where $\arg(\cdot)$ means the phase of a complex value.

When only one coil is transmitting RF, the signal to noise ratio (SNR) will be very low for areas that are far away from the coil. In order to reduce the resulting phase noise, the final estimation of Ψ_k is obtained by averaging through J receive coils,$\Psi_k = \sum_{j=1}^{J} \Psi_k(j)/J$. Only images with one coil transmitting at a time are utilized in Eq. 2.27. It should be emphasized that only relative (not absolute) B_1^+ phases can be measured [83] in standard MR settings. Relative B_1^+ maps are however sufficient for parallel transmit RF design.

Relative B_1^+ Magnitude Maps

Using the same data, we can establish a relative magnitude ratio as

$$P_k(j) = \left|\frac{\tilde{I}_{j,k}}{\tilde{I}_{j,0}}\right| = \left|\frac{\tilde{R}_j\,\tilde{T}_k\,\tilde{C}}{\tilde{R}_j\,\tilde{T}_0\,\tilde{C}}\right| = \left|\frac{\tilde{T}_k}{\tilde{T}_0}\right| = \frac{\sin\alpha_k}{\sin\alpha_0}\cdot\frac{1-\cos\alpha_0\cdot E_1}{1-\cos\alpha_k\cdot E_1} \tag{2.28}$$

with $\alpha_k = V|\tilde{B}^+_{1,k}|\gamma\tau$ and $\alpha_0 = V\left|\sum_{k=1}^{K}|\tilde{B}^+_{1,k}|\,e^{i\theta_k}\right|\gamma\tau$. Here α_0, the flip angle when all coils are transmitting together, is proportional to the magnitude of the sum of K complex transmit B1 vectors. $P_k(j)$ represents, for receive coil j, ($j = 1, 2, \ldots, J$, where J is the number of receive coil; in the present work we only used transceivers so $K = J$) the fraction of the signal magnitude, when transmitting through coil k, over the signal magnitude when transmitting through all coils.

Under appropriate conditions, two approximations can be made on Eq. 2.28. First, we assume small tip angles, e.g., $(\alpha_k, \alpha_0) < 10°$, which leads to $\sin\alpha_k \approx \alpha_k$ and $\sin\alpha_0 \approx \alpha_0$. Second, we assume that with conveniently chosen α and TR, the ratio $(1-\cos\alpha_0\cdot E_1)/(1-\cos\alpha_k\cdot E_1)$ is not very different from unity and thus can be replaced by 1. As a result, the signal intensity is approximately proportional to α and the following linear algebraic formalism can be written

$$P_k(j) = \left|\frac{\tilde{I}_{j,k}}{\tilde{I}_{j,0}}\right| = \frac{\sin\alpha_k}{\sin\alpha_0}\cdot\frac{1-\cos\alpha_0\cdot E_1}{1-\cos\alpha_k\cdot E_1} \approx \frac{\alpha_k}{\alpha_0} = \frac{|\tilde{B}^+_{1,k}|}{\left|\sum_{k=1}^{K}|\tilde{B}^+_{1,k}|\,e^{i\theta_k}\right|} \tag{2.29}$$

For better SNR, the final P_k estimation is obtained by averaging through the J receiver coils, $P_k = \sum_{j=1}^{J} P_k(j)/J$.

Note that although used in the definition of the relative magnitude ratio, the magnitude of the image acquired with all coils transmitting together can be replaced by the magnitude of sum (MOS) of the J single transmit coil complex images since no significant differences should be observed between those two magnitude images if linear approximations are fulfilled. At this point, relative transmit magnitude maps have been established without altering any corresponding transmit phases.

Data Acquisition

In this study, a series of $(K+2)$ GE images was acquired, consisting of K images ($\tilde{I}_k$, $k = 1, 2, \ldots, K$, $K = 8$ or 16) with RF power delivered to only one transmit coil at

a time, one additional image with all coils simultaneously transmitting RF ($\tilde{I}_0$) used to verify the assumed linear approximation, and one additional image without any RF power used to calibrate the noise level of each receive channel. In this scheme, only transmit B1 magnitudes are modulated (ON/OFF), not the phases. A low flip angle was used ($\alpha < 10°$) to satisfy $\sin\alpha \approx \alpha$. Low spatial resolutions (3-4mm/pixel) along phase encoding axis were used, along with relatively short TR's, to shorten the acquisition. Because of small tip angles, the signal intensity was still approximately proportional to α with very limited T1 weighting. One second of dummy RF pulsing was used to approach the steady state for each image. RF spoiling and gradient spoilers were used to avoid stimulated echoes in final images. Using all images from each $J = K$ receive channels, we collected a total number of $K \times (K + 2)$ images. Each of the latter was normalized by the noise standard deviation of the corresponding receive channel. Only pixels with SNR above 4 were considered to derive the relative B1 information, allowing for reducing noise in relative phase calculation and for avoiding significant issues that arise due to random distribution in magnitude images where SNR is too low.

2.9.3 Absolute Magnitude B_1^+ Mapping

In order to derive the absolute magnitude B_1^+ map for individual RF coils, one absolute magnitude B_1^+ map (or more) needs to be acquired in the large flip angle regime with all coils transmitting together. In our implementation, we always utilized the same set of transmit B1 phases during the small and the large flip angle images. Although a different set of phase could be actually used for the large flip angle map, this unique set of phases allows a simplified formalism to describe the algorithm.

In principle any absolute B1 mapping techniques could be used for this purpose. We choose the actual flip angle imaging (AFI) method introduced by [74] where two TR are interleaved because it provides significant advantages at high field. First, AFI is fast and measures 3D magnitude B1 map over the whole head within less than 3 minutes despite of long tissue T1 at 9.4T because the T1 weighted terms vanish during the parametric calculation. Second, a single large flip angle is used, which needs to be somewhere between 15° and 90°, which typically requires less RF peak power than other multi-flip-angle methods where the largest flip angle often largely exceeds 90° in some locations. Last, it is less sensitive to physiological head motion than long TR based

techniques. A noticeable difference with the relative B1 maps is that here standard images reconstructed as root sum of square through all receive channels can be used to calculate this absolute B1 map which inherently optimizes receive SNR for multiple receive channels.

Actual Flip Angle Imaging

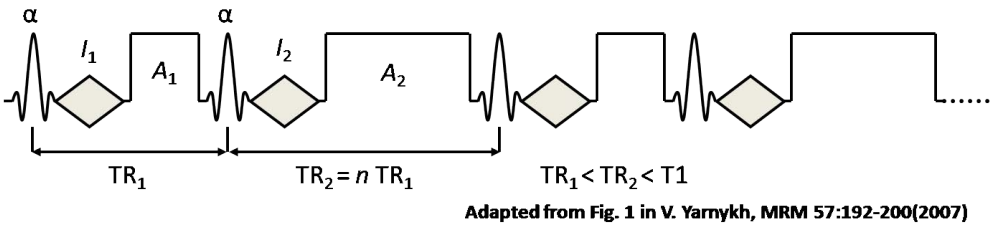

Figure 2.5: Schematic diagram of AFI pulse sequence. All RF excitations are performed for the same flip angle α with two interleaved repetition times (TR_1 and TR_2). Image acquisitions (shown by shaded diamonds) are conducted using gradient echos. A_1 and A_2 represent gradient spoilings.

Fig. 2.5 displays the timing diagram of the AFI sequence. As can be seen, the AFI pulse sequence consists of two identical interleaved images where RF excitations are obtained with a unique flip angle α. The only difference between the two images consists of the two interleaved repetition times, TR_1 and TR_2 ($TR_1 < TR_2 < T_1$). The two images, I_1 and I_2, are acquired after the corresponding pulses in a standard gradient echo scheme. Here A_1 and A_2 are gradient spoilers used to destroy transverse magnetizations at the end of the two time delays. Once the pulsed steady state is reached, the flip angle can be calculated using the ratio of the two acquired images

$$\alpha \approx \arccos[(r \cdot n - 1)/(n - r)] \tag{2.30}$$

where $r = I_2/I_1$ and $n = TR_2/TR_1$. Note that Eq. 2.30 is obtained by assuming an ideal spoiling of transverse magnetization in the sequence and that the validity of Eq. 2.30 requires the image signals to be formed with the same flip angle.

Data Acquisition

In this study, a 3D gradient echo pulse sequence was modified to acquire the two interleaved TR images. For all AFI acquisitions, $TR_1 = 28\,ms$ and $TR_2 = 140\,ms$ ($n = 5$) were used. In addition, both RF and gradient spoilings were optimized to minimize the effects of stimulated echos as described in Ref. [84]. The incremental phase for RF spoiling was set to 35°, and a strong gradient spoiling regime was reached with $A_1 = 225$ mT·ms/m and $A_2 = 1125$ mT·ms/m. Given the fact that we were primarily interested in obtaining B_1^+ map within an axial slice, we used a selective slab excitation centered along z direction on the slice of interest. This selective slab excitation together with 15 phase encoding steps along z resulted in a reduced acquisition time. Through-plane resolution was 5 mm.

2.9.4 Merging Absolute and Relative B_1^+ Maps

In the last step of this multi-channel mapping technique, the obtained relative and absolute B1 maps are combined to generate the final complex B_1^+ map for individual RF coils. The absolute magnitude B1 map of transmitting through all coils is multiplied by the relative magnitude B1 map to calculate the absolute B_1^+ magnitude map for each coil. This calculated absolute magnitude map is then combined with the corresponding relative B_1^+ phase map to derive the final complex B_1^+ map. Assuming that RF phases θ_k are used, the final complex valued map for channel k is provided by

$$\tilde{B}^+_{1,k} = P_k \cdot |\tilde{B}^+_{1,0}(\theta_k)| \cdot e^{i\Psi_k} \tag{2.31}$$

where $|\tilde{B}^+_{1,0}(\theta_k)|$ is the large tip angle magnitude B_1^+ map with all coils transmitting RF. P_k is the relative magnitude B1 ratio, representing the fraction of the signal magnitude, when transmitting through coil k, over the signal magnitude when transmitting through all coils.

In this study, prior to applying the multi-channel mapping, local B1 phase shim [29, 82] was applied to obtain transmit phases that would provide sufficient SNR for every pixel within the region of interest.

Chapter 3

Parallel Excitation: A Simulation Study

3.1 Introduction

In this chapter we describe a simulation study, aiming at investigating parallel transmission using an electromagnetic model closely reproducing experimental conditions at 9.4 T. Two dimensional (2D) parallel excitation RF pulses with spiral and echo planar trajectories were designed for different specifications based on simulated transmit B1 profiles. Bloch simulations of parallel excitation were performed to verify those calculated pulses and to investigate some important properties of 2D parallel excitation.

3.2 Materials and Methods

The RF coil which was modeled in this work was a 16-element stripline array [28] mounted on a cylindrical former of 32 cm in diameter. Electromagnetic field distributions of this coil loaded with a spherical phantom (18 cm in diameter) filled with 90-mM saline (conductivity = 0.9 S/m and dielectricity = 80) were calculated by solving the Maxwell's equations with the finite difference time domain method (Remcom Inc., PA, USA). The output magnetic fields were further processed to calculate the complex transmit B1 map for each of the 16 coil elements [85]. Although the stripline array coil that we modeled (and which we used in multiple experiments) had 16 transceiver elements,

our 9.4 T human system was only equipped with eight independent transmit channels at the time of this study. As a result, we used every other elements (odd numbered) of the 16 channel coil to perform 8 channel parallel transmission. Fig. 3.1 shows the resulting transmit B1 maps within an axial slice of the phantom, along with the magnitude and phase of the complex sum of them. One can immediately notice in this figure the strong transmit B1 inhomogeneities that are typical when imaging large samples at very high magnetic field.

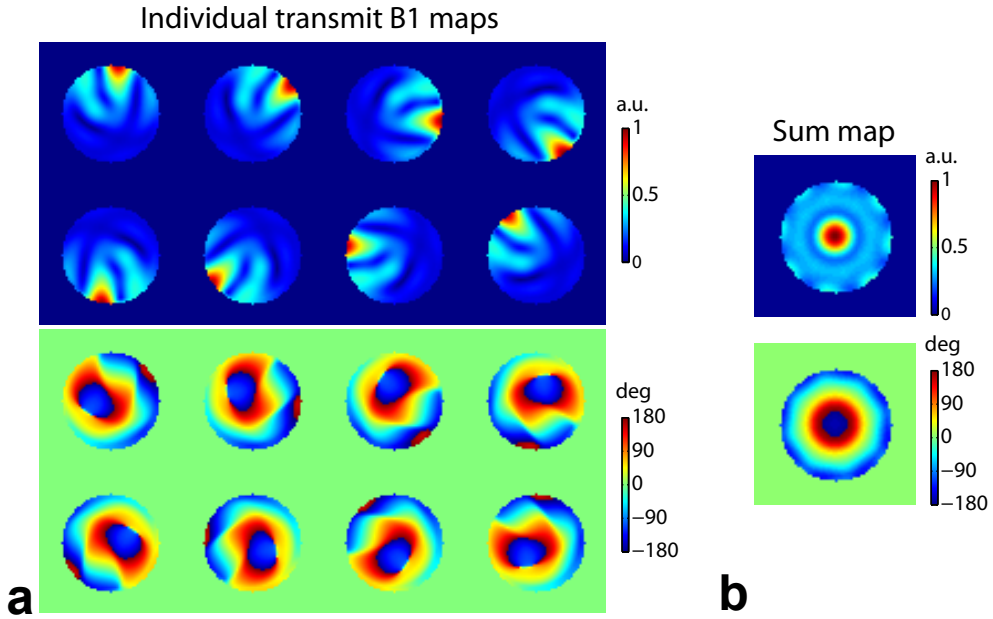

Figure 3.1: (a) Simulated transmit B1 magnitude (top) and phase (bottom) maps for the eight elements of a stripline array loaded with a phantom at 9.4 T. (b) The magnitude and phase of the complex sum of the eight maps in (a).

Three desired excitation patterns (Fig. 3.2) designed within the axial slice of interest of the phantom were considered for selective RF pulse design: a homogeneous excitation, "CMRR" letters (which stands for the Center for Magnetic Resonance Research at the University of Minnesota) and a checkerboard. All patterns were defined on a 64×64 grid with a spatial resolution of 4.4 mm.

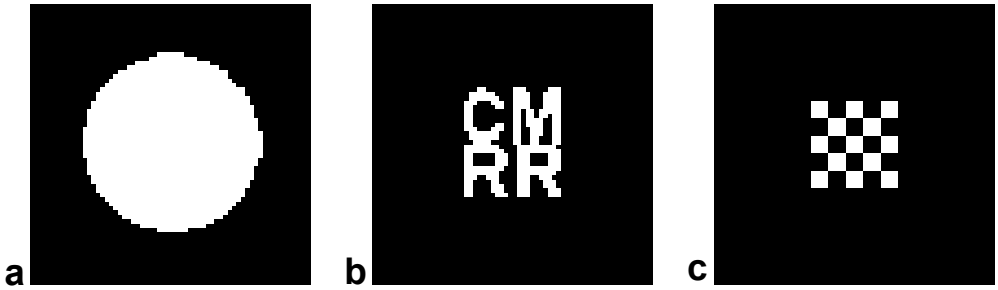

Figure 3.2: Three desired excitation patterns. (a) Uniformity excitation. (b) CMRR letters. (c) A checkerboard. All patterns were defined on a 64×64 matrix with 4.4-mm resolution. Brightness represents a uniform excitation for 30° flip angles, whereas darkness stands for 0° flip angles. The phase was set to 0° everywhere.

3.2.1 K-Space Trajectory

Two-dimensional (2D) spiral and echo planar (EP) excitation k-space trajectories used for pulse calculations were designed with different levels of k-space undersampling (Fig. 3.3a and b). The spirals were designed with constant angular velocities, and the EP trajectories with rewinders were derived from the EP trajectories generated for standard EPI sequences by our 9.4T console. The dwell time was set to $4\,\mu$s for all trajectories in order to comply with the data format required by the scanner. The maximum gradient strength and slew rates of the designed spirals were 16.5 mT/m and 152 T/m/s, and the maximum gradient strength and slew rates of the EP trajectories were 23.5 mT/m and 159 T/m/s. Note that all those excitation k-space trajectories started from the periphery of k-space and ended at the origin of k-space.

Both the spiral and EP trajectory designs started by fully sampling the k-space and then undersampled the k-space by reduction factors of 2, 4 and 8 (defined as a metric to quantify the extent to which the k-space was undersampled). The spiral trajectory that fully sampled the k-space had 16 turns and was 10.9 ms in length. The spiral trajectories undersampled the k-space along the radial direction via successively doubling the separation between the turns of the spiral while keeping the k-space coverage unchanged. Consequently, the number of turns (pulse duration) decreased to 8 (5.5 ms), 4 (2.7 ms) and 2 (1.4 ms), corresponding to a reduction factor of 2, 4 and 8, respectively. The EP trajectory with a fully sampled k-space had 33 readout lines and was 10.2 ms.

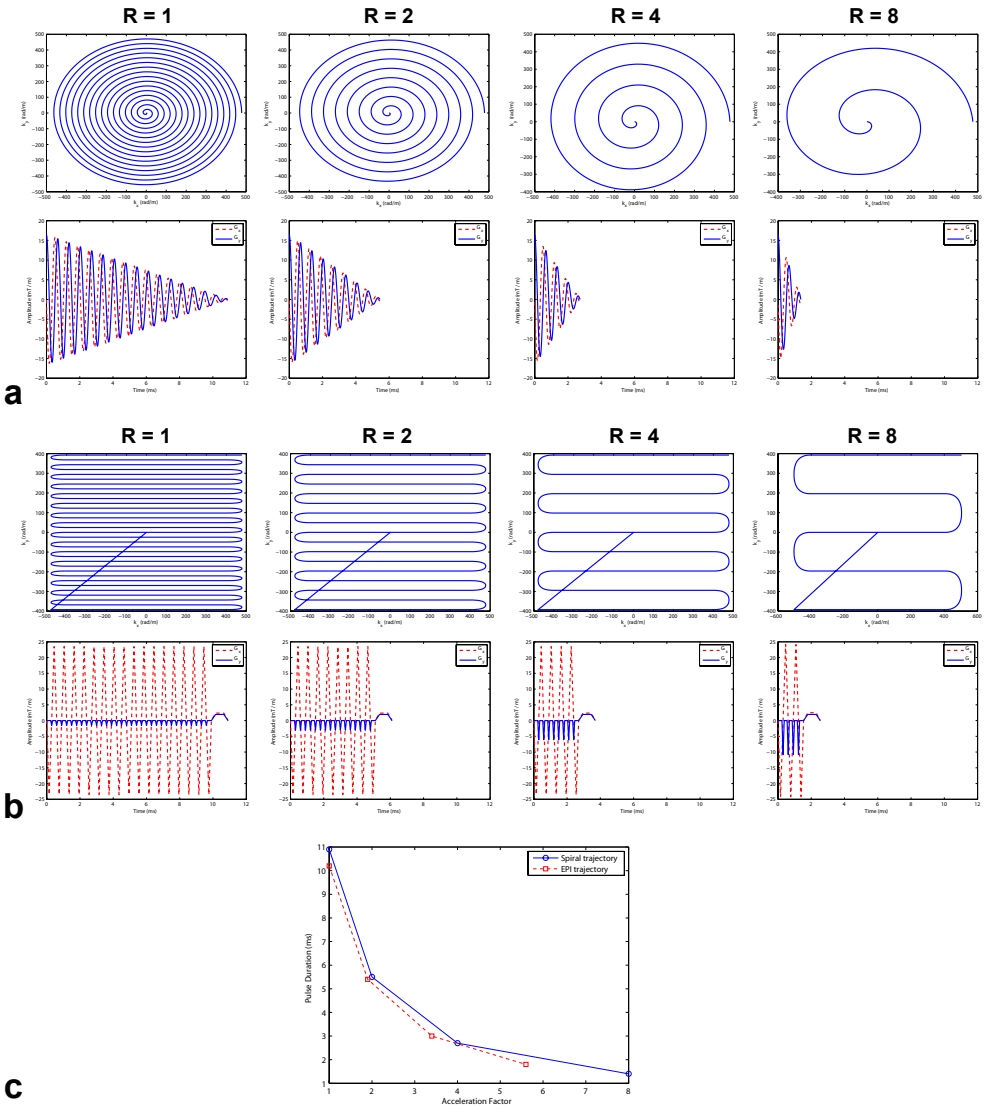

Figure 3.3: Spiral-in (a) and echo planar (b) k-space trajectories, and corresponding Gx (red dashed curve) and Gy (blue solid curve) waveforms. The k-space trajectories started by fully sampling the k-space (reduction factor = 1) and then undersampled it radially (spiral) or along phase encoding direction (echo planar) by reduction factors of 2, 4 and 8. (c) RF pulse duration vs acceleration factor for spiral (blue circle) and echo planar (red square) trajectories. Note that acceleration in time was the same as reduction in k-space sampling for spirals, but it was less than reduction for echo planar trajectories due to the tail rewinder.

Unlike spirals which radially undersampled k-space, EP trajectories undersampled the k-space along phase encoding direction by increasing the distance between readout lines while preserving the k-space coverage. As a result, the number of lines (pulse duration) reduced to 17 (5.4 ms), 9 (3.0 ms) and 5 (1.8 ms), corresponding to a reduction factor of 2, 4 and 8, respectively.

Although a larger reduction factor will result in a shorter pulse duration, the actual pulse duration often does not exactly decrease linearly with the reduction factor, which is mostly due to limits and constraints in gradient waveform design (slew rate, gradient strength, rewinding lobes). Therefore, we rather choose a metric associated with the actual pulse duration: we defined the ratio of unaccelerated over accelerated pulse durations as the "acceleration factor" and we used the latter (not the reduction factor) to quantify RF pulse acceleration. In spiral trajectories (Fig. 3.3a), RF pulse and gradient waveform typically end at the same time because there is no gradient rewinding lobe. Therefore, the dwell time (4 μs) multiplied by the number of time points directly provides the pulse duration. EP trajectories, however, typically end with a rewinding gradient lobe played after the end of the RF excitation (Fig. 3.3b). In practice, in our EP sequences this rewinder lobe had always the duration of one readout line (with the gradient strength being adjusted accordingly in order to end at the center of the k-space). Therefore, the RF pulse duration with an EP trajectory was defined as the duration of one readout line multiplied by the number of the readout lines plus one. Fig. 3.3c displays a plot of pulse duration versus acceleration factor for the abovementioned spiral and EP trajectories.

3.2.2 RF Pulse Calculation

Parallel transmit RF pulses were designed in the small tip angle regime using the spatial domain method [30]. The minimization problem was formulated as $\min_b \|Ab - m\|_{(S)}$, where A is the system matrix involving considered excitation k-space trajectories and transmit B1 maps. b is a vector containing the eight complex valued RF waveforms, and m is a vector representing the desired excitation pattern. S is a diagonal matrix defining the region of interest on which RF pulses are calculated. Here all terms, except for S, are complex. Therefore, for conciseness, the tilde sign is no longer used to indicate a complex value. The nominal flip angle was set to 30° for all desired excitation patterns

(Fig. 3.2). The minimization problem was solved for required RF shapes (b) using conjugate gradient (CG) iterations. The number of iterations (playing the role of the regularization parameter) was determined with the L-curve criterion [25]. The L-curve was generated by running 50 CG iterations and plotting the solution norm ($\|b\|_2$) vs residual norm ($\|Ab - m\|_2$) for each iteration. The number of iterations at the corner of the L-shaped curve was chosen to calculate the pulses.

In order to show the advantages of parallel transmission for accelerated 2D selective excitation, traditional single-channel 2D spatially selective RF pulses were also designed based on the same k-space trajectories used for multi channel transmit pulses, and were compared to those parallel transmit pulses. In this single-channel case, an identical RF waveform was obtained for all channels using the complex sum (Fig. 3.1b) of the eight individual maps as the transmit B1 input.

In construction of all system matrixes, pixels without spins (located outside the phantom) were excluded. The dwell time was 4 μs for both the gradient and RF pulses (4 μs is the time unit used by the gradient and RF waveform synthesizers of the scanner). The spatial resolution was set to 4.4 mm for the field of exitation and for the interpolated transmit B1 maps.

As expected, the time dimension of matrix A dramatically decreases with increasing acceleration. Table 3.1 lists the matrix sizes for different specifications.

Spiral Trajectory			EP Trajectory		
AF	Parallel Tx	Single-Ch Tx	AF	Parallel Tx	Single-Ch Tx
1	1284×21808	1284×2726	1	1284×21808	1284×2726
2	1284×10904	1284×1363	1.9	1284×12208	1284×1526
4	1284×5448	1284×681	3.4	1284×7408	1284×926
8	1284×2720	1284×340	5.6	1284×5088	1284×636

Table 3.1: Sizes of system matrix A for different specifications. Note that the matrix size decreased as the acceleration factor (AF) increased.

3.2.3 Bloch Simulation

Bloch simulations of 2D parallel transmission using the rotation matrix based simulator were performed to simulate the distribution of transverse magnetization due to the

application of selective gradient and RF pulses. The transverse magnetization distributions corresponding to different acceleration factors, different k-space trajectories and different target excitation patterns were simulated. Those distributions were compared to the target excitation pattern in order to evaluate the performance of RF pulses calculated with different specifications. Similar simulations were also conducted using RF pulses designed for single-channel excitation, and the results were compared to those of parallel transmission. In all simulations, the excitation pattern was calculated on a $20 \times 20\,\mathrm{cm}^2$ FOX with a 64×64 matrix in order to match the pulse design settings. In all cases, the longitudinal magnetization at equilibrium was assumed to be uniform through the sample; relaxation and diffusion terms were ignored.

To verify parallel transmission, Bloch simulations using only one of the eight calculated RF pulses at a time were conducted. The RF pulses designed for the checkerboard using the spiral trajectory of $4\times$ acceleration were considered for this verification. The eight simulated excitation patterns, each resulting from one different transmit channel, were checked to see if artifacts due to k-space undersampling would exist and to verify if the desired excitation pattern would emerge in the complex sum of the eight artifact contaminated patterns.

3.2.4 B_0 Inhomogeneity: Impact and Correction

To demonstrate the impact of B_0 inhomogeneity (ΔB_0) on excitation accuracies in parallel transmission, a 2D gaussian shaped ΔB_0 distribution with a maximum off resonance frequency of 100 Hz was designed and considered for Bloch simulations using RF pulses calculated for different acceleration factors, without ΔB_0 compensation.

To show the effectiveness of incorporating ΔB_0 information into pulse design to correct for off-resonance effects, the maximum frequency was changed from 100 to 500 Hz and the new ΔB_0 map was considered in Bloch simulations. Simulated excitation patterns using RF pulses calculated with and without correction of this increased B_0 inhomogeneity were obtained and compared.

3.3 Results

From the SVD of the system matrix (Fig. 3.4), one can see that the singular values decayed to zero (resulting in a large condition number), and that the left and right singular vectors tended to oscillate more strongly as the index i increased.

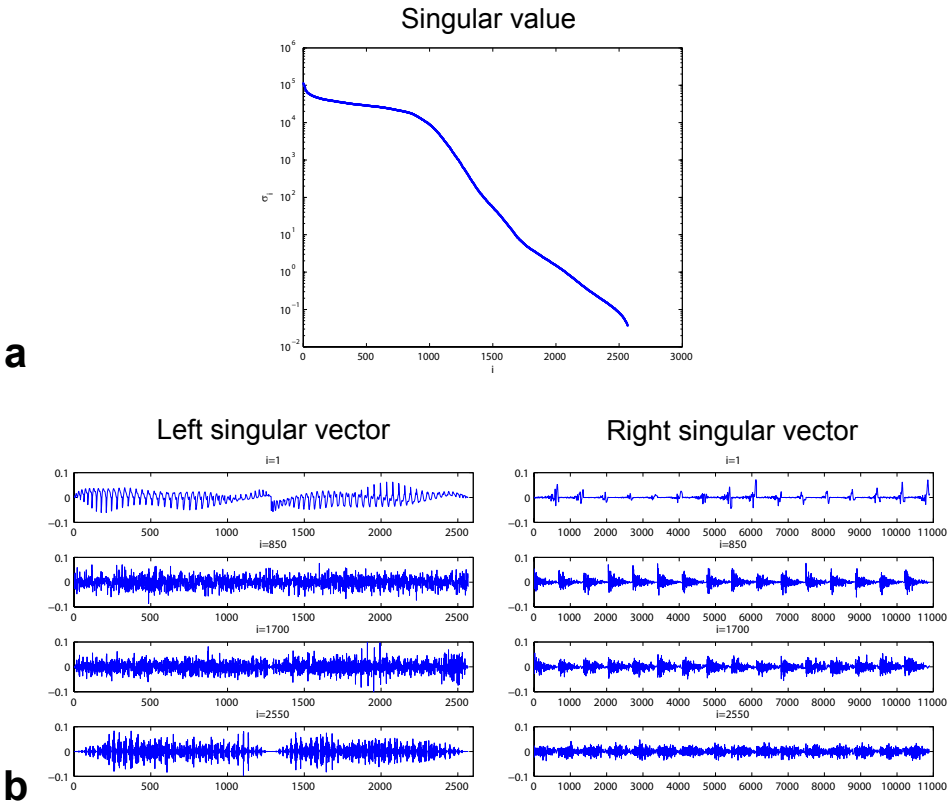

Figure 3.4: Singular values (a) and vectors (b) of a system matrix used for parallel transmit RF pulse calculations. The matrix was built using the spiral trajectory with $4\times$ acceleration. The condition number of this matrix was large ($\sigma_1/\sigma_N \approx 3.04 \times 10^6$) and its singular vectors tended to oscillate more strongly as index i increased, indicating a discrete ill-posed problem associated with RF pulse design.

As seen in Fig. 3.5a, the plot of solution norm ($\|b\|_2$) vs residual norm ($\|Ab - m\|_2$) obtained based on conjugate gradient iterations exhibited a typical L-shaped curve with a distinct corner. Fig. 3.5b displays the magnitude and phase of the RF pulse for each of the eight channels, calculated with the corner number of iterations.

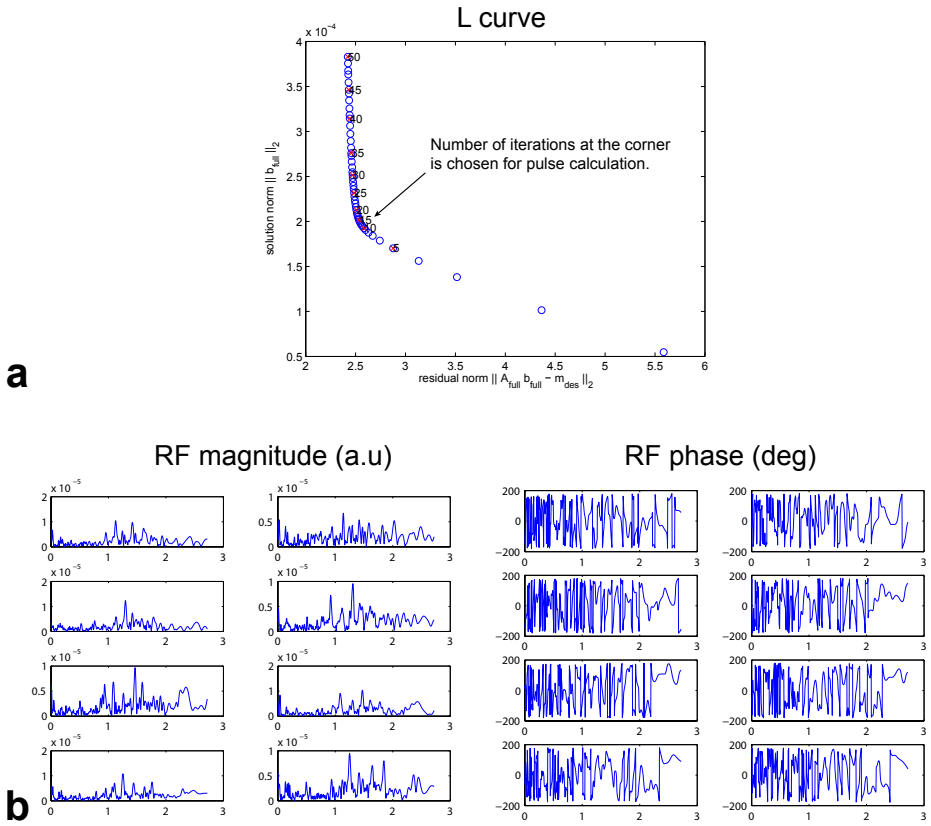

Figure 3.5: Calculations of parallel transmit RF pulses for a checkerboard pattern using a spiral trajectory with 4× acceleration. (a) The L-shaped curve, the corner of which was used for determining the number of conjugate gradient iterations optimal for pulse calculation. (b) Resulting RF magnitude and phase variations as a function of time for each of the 8 transmit channels.

Fig. 3.6 shows the simulated excitation pattern for the parallel transmit RF pulses designed with the spiral trajectory of 4× acceleration. The excitation magnitude pattern matched the target checkerboard with small deviations visible from the comparison of simulated and desired intensity profiles. The phase of the transverse magnetization was close to the desired value (0°) within those desired excitation squares. The random phase values were observed elsewhere, which was expected given the fact that the magnitude target for those voxels was zero.

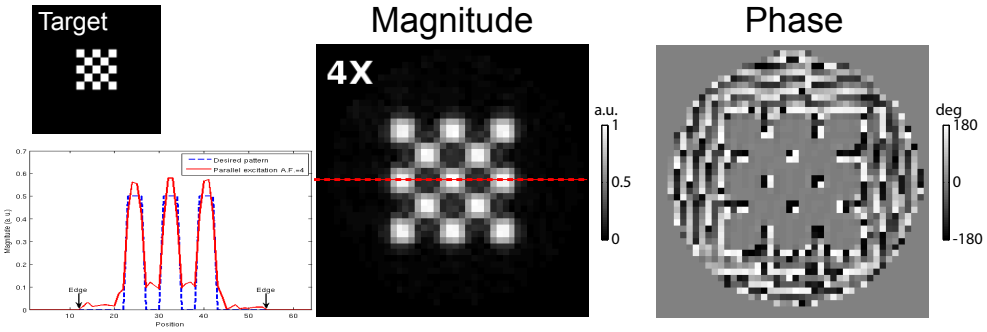

Figure 3.6: Magnitude and phase of simulated transverse magnetization. RF pulses shown in Fig. 3.5 were used. The lower left plot displays comparison of desired (blue dashed curve) and simulated (red solid curve) intensity profiles along the red dashed line in the magnitude map. The excitation pattern matched the target checkerboard. Note that the phase was close to the desired value (0°) within those desired excitation squares, but was randomly distributed elsewhere.

Fig. 3.7a displays the calculated excitation pattern for each of the eight RF pulses designed for an acceleration factor of 4. As expected, significant artifacts due to undersampling of k-space were observed in each of the eight excitation patterns considered separately. Fig. 3.7b shows that the sum of the magnitudes (SOM) of the eight excitation patterns resulted in dramatic aliasing artifacts. By contrast, those artifacts disappeared when the complex sum of the eight patterns was performed as seen in the magnitude of the complex sum (MOS).

Fig. 3.8 shows a comparison of parallel transmission and single-channel excitation for different acceleration factors and different target excitation patterns using spiral trajectories. For each of the three target patterns, significant excitation errors were observed with single-channel transmission and acceleration. Those errors became more

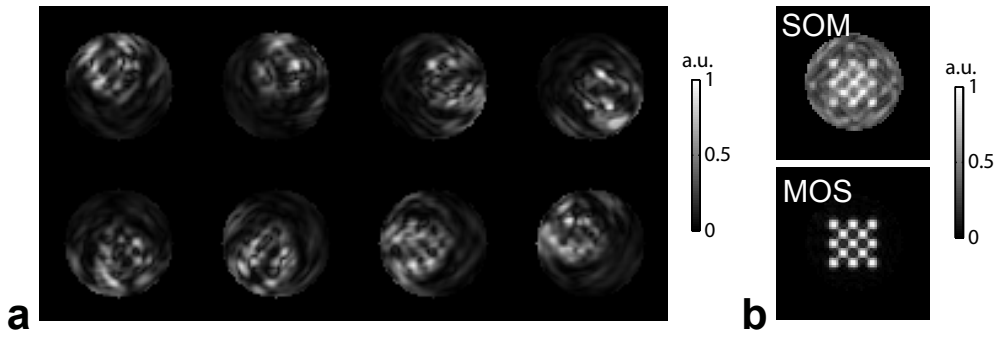

Figure 3.7: Verification of parallel transmission. (a) Simulated excitationn patterns for each of the eight RF pulses as in Fig. 3.5. (b) Sum of the magnitudes (SOM) of and the magnitude of the complex sum (MOS) of the eight excitation patterns in (a). Note that artifacts due to k-space undersampling observed in the SOM image were eliminated in the MOS image.

and more severe as acceleration increased. By contrast, the target excitation patterns were easily identified when using actual parallel transmission for each acceleration factor. However, excitation fidelity decreased as acceleration increased with noticable excitation errors seen in the background when using 8× reduction, which constitutes the theoretical acceleration limit of an eight-channel transmit setup. Similar results were obtained when using EP trajectories for pulse design (Fig. 3.9).

Fig. 3.10 displays the effects of B_0 inhomogeneity on excitation accuracy of parallel transmission. Without correction of ΔB_0 in pulse design, blurring artifacts were observed in the excitation pattern when using the spiral trajectories, whereas when using the EP trajectories, geometric distortions (mostly a shift along the phase encoding direction) were seen. Those excitation inaccuracies due to off-resonance effects became less with more accelerated RF pulses and were almost invisible with 8× reduction (corresponding to a pulse duration less than 2 ms) when the ΔB_0 was not large (100 Hz maximum).

As seen in Fig. 3.11, when large off resonances were present (500 Hz maximum), strong distortions were evident in excitation patterns even with RF pulses designed with significant acceleration (4× reduction, corresponding to a pulse duration of about 3 ms compared to more than 10 ms with no reduction) but without correction of ΔB_0.

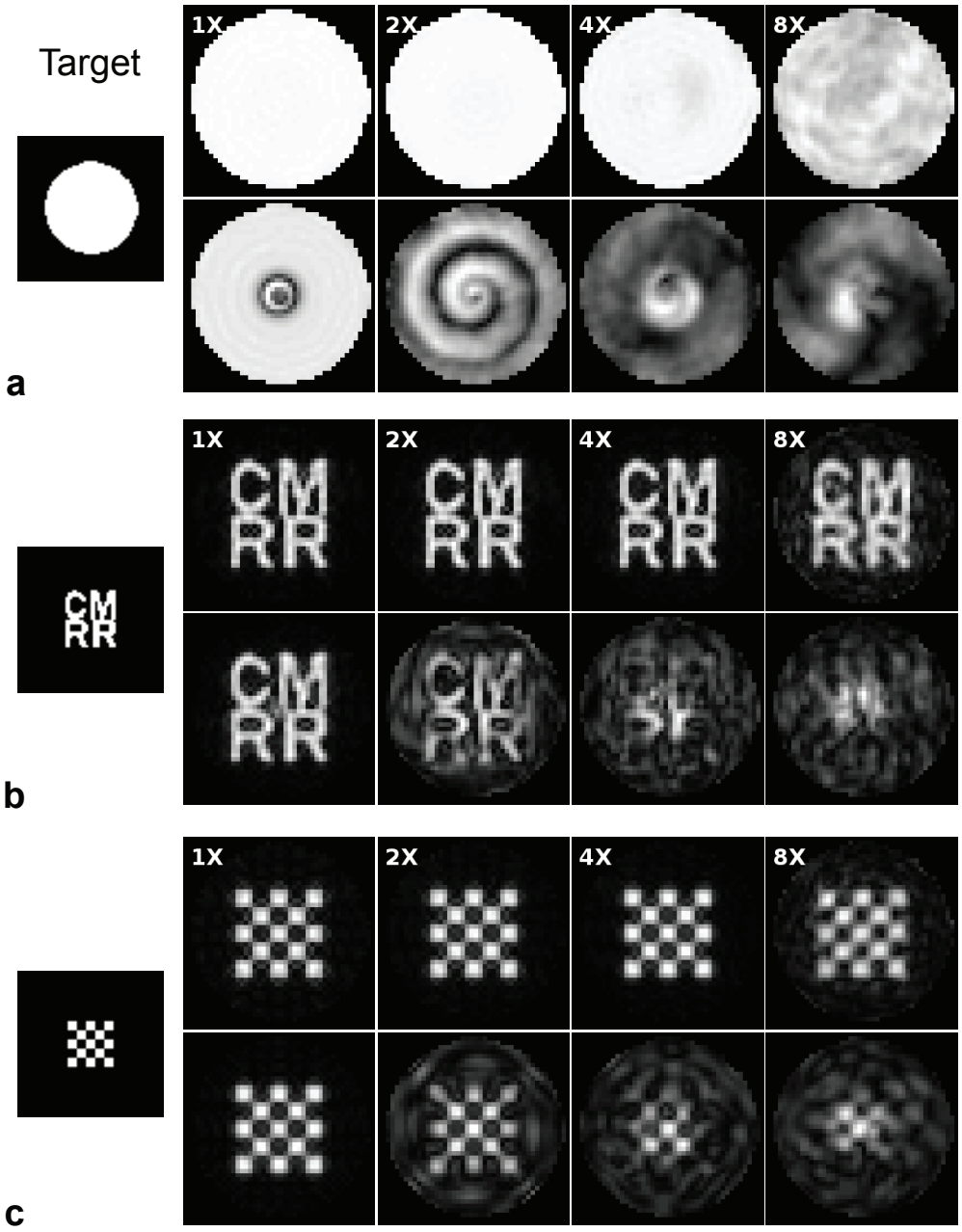

Figure 3.8: Parallel vs single-channel transmission using spirals. RF pulses were designed for 1×, 2×, 4× and 8× accelerations and for flat (a), CMRR (b) and checkerboard (c) targets. For each target, top row shows excitation patterns for parallel transmission, and bottom row for single-channel transmission. Note that obvious blurring artifacts due to k-space undersampling were observed with single-channel excitation and acceleration.

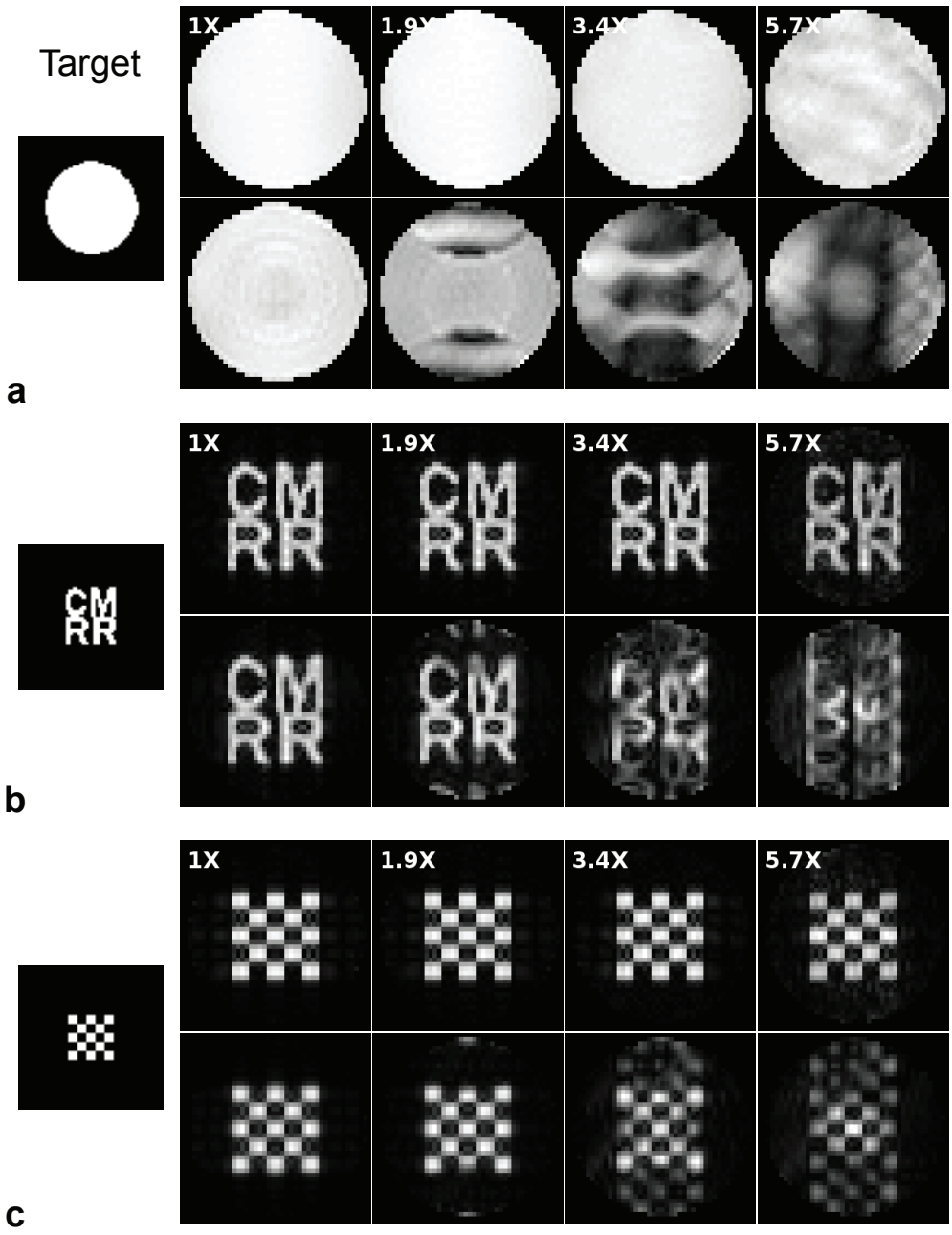

Figure 3.9: Parallel vs single-channel transmission using echo planar trajectories. RF pulses were designed for 1×, 1.9×, 3.4× and 5.7× accelerations and for flat (a), CMRR (b) and checkerboard (c) targets. For each target, top row shows excitation patterns for parallel transmission, and bottom row for single-channel transmission. Note that obvious aliasing artifacts due to k-space undersampling were observed with single-channel excitation and acceleration.

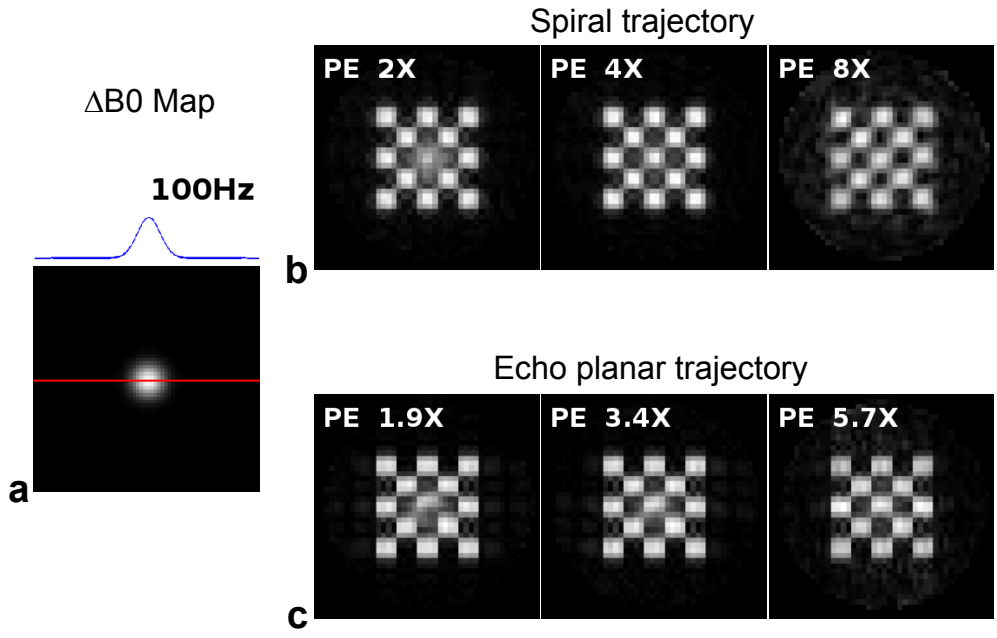

Figure 3.10: Effects of off resonance on excitation accuracy in parallel transmission. (a) Gaussian shaped ΔB_0 with a maximum frequency of 100 Hz considered in Bloch simulations. (b,c) Excitation patterns using RF pulses designed for different accelerations and without off-resonance compensation. Note that for both spiral and echo planar trajectories, off-resonance effects decreased with increasing acceleration.

However, those distortions were effectively eliminated using corrected RF pulses designed with consideration of B_0 inhomogeneity.

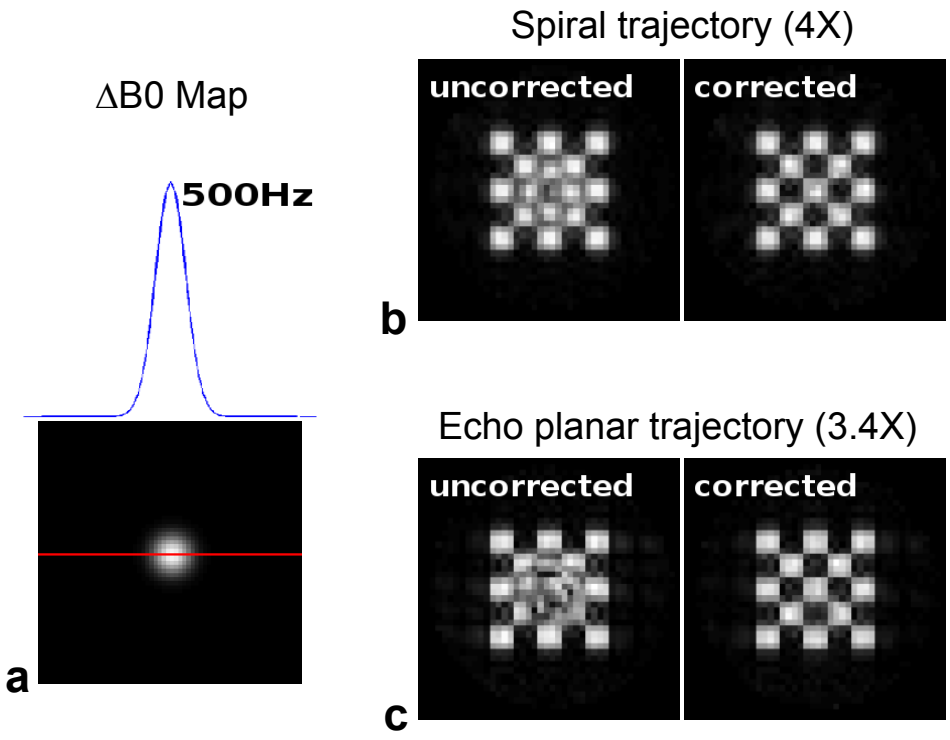

Figure 3.11: Correction of ΔB_0. (a) Considered gaussian shaped ΔB_0 with maximum frequency being 500 Hz. (b,c) Excitation patterns for moderately accelerated RF pulses ($\sim$ 3ms in length) designed with (corrected) and without (uncorrected) off-resonance compensation. Note that for both spiral and echo planar trajectories, excitation deteriorations due to off-resonance effects were minimized with corrected pulses.

3.4 Discussion and Conclusion

We have demonstrated successful implementation of RF pulse design for 2D parallel transmission based on simulations at 9.4 T. Our results show that our computational model for parallel transmit RF pulse design was able to provide correct accelerated 2D selective pulses with or without B_0 inhomogeneity compensation for a multi-channel

transmission setup. Those results also suggest that our Bloch simulator can be used to evaluate the performance of those designed RF pulses. In addition, we compared parallel transmission to single-channel transmission using different specifications.

The analysis of the system matrix based on sigular value decomposition showed that the inverse problem formulated for parallel transmit RF pulse design in small tip angle regime is by essence an discrete ill-posed problem. Therefore, a regularization is in the calculation to obtain reliable RF pulse solutions. In this study, the conjugate gradient iterations with implicit regularization proved to provide satisfactory results, and this approach offers the significant advantage of being highly efficient in terms of computation time. However, it should be mentioned that other methods (e.g., Tikhnov regularization) can be considered for improved regularization.

Significant distortions present in excitation patterns using shortened RF pulses designed for single-channel transmission indicate that without the incorporation of multiple transmit B1 sensitivity profiles into pulse design, it is impossible to achieve accelerated 2D spatially selective RF excitation by undersampling the k-space. Indeed, those single-channel transmit RF pulses are meant to be only designed and applied with a fully sampled k-space. By contrast, parallel transmit RF pulses were able to provide recognizable and undistorted excitation patterns even when a significantly reduced pulse duration with acceleration of up to $\times 8$ was used. It can be noted that in the single-channel excitations with acceleration, the excitation errors due to k-space undersampling mostly translated to blurring artifacts when using spiral trajectories, whereas they translated into Nyquist ghosts when using EP trajectories. This is consistent with well-known artifacts observed in images reconstructed using undersampled k-space data, indicating that the excitation k-space model (i.e., the RF waveform and resulting transverse magnetization form a Fourier transform pair) is a good linear approximation of the nonlinear Bloch equations.

When off-resonance frequency is not very large (e.g., < 100 Hz), uncorrected parallel transmit RF pulses designed without B_0 inhomogeneity compensation are almost insensitive to off resonances, especially for high acceleration factors (> 4). This is because of the much shortened pulse duration due to acceleration which increases the RF bandwidth, thus reducing the sensitivity to off-resonance effects. However, a too large acceleration factor cannot be used since the excitation fidelity decreases with increasing

acceleration and particularly noticeable background excitation errors start to be seen when the corresponding reduction of k-space sampling approaches the theoretical limit of the multi-transmit setup (e.g., 8 for eight channels in our case). Therefore, in general a moderate acceleration (e.g., $4\times$ in our case) providing a good compromise between pulse duration and excitation accuracy should be considered for pulse design. When large B_0 inhomogeneity is present (e.g. ~ 500 Hz), strong artifacts due to off-resonance effects are inevitable outcome of any uncorrected RF pulses, indicating a necessary of ΔB_0 correction in pulse design. Our results further show that incorporating known ΔB_0 information into RF pulse calculation can effectively minimize those obvious off-resonance induced artifacts and restore the excitation fidelity.

In conclusion, we have demonstrated 2D parallel transmission with eight transmit channels using simulations. With the capability of designing and evaluating RF pulses correctly and robustly, we are ready to proceed to carry out real parallel transmission experiments on our 9.4 T human scanner.

Chapter 4

Parallel Excitation in the Human Brain at 9.4 T Counteracting k-Space Errors With RF Pulse Design

This is a manuscript accepted for publication in Magnetic Resonance in Medicine.

4.1 Introduction

Multidimensional spatially selective radiofrequency (RF) pulses [16, 17] have been proposed in a variety of MR applications, including arbitrarily defined excitation volumes [86] and transmit B1 (B_1^+) inhomogeneity mitigation at high field [19]. However, due to limited gradient system capability, these RF pulses typically require a long duration (several tens of milliseconds), which makes them impractical due to spin transverse relaxation, amplitude of static field (B_0) inhomogeneity, and cumulative gradient errors. These problems are even more pronounced at very high field due to larger B_0 nonuniformity and shorter transverse relaxation time constants. It has been shown that these limitations can be overcome using parallel excitation techniques [20, 21, 25, 26, 30, 58, 87, 88], allowing for short, accelerated, selective RF pulses.

These accelerated RF pulses are especially promising at very high field where B_1^+ profiles are significantly heterogeneous [2]. However, even with such shortened RF pulses significant degradation of excitation patterns can occur, especially in the case of gradient system imperfections.

Previous studies have shown with conventional single-channel transmit (Tx) systems that using the actual, measured gradient waveforms (or k-space trajectory) for two-dimensional (2D) RF pulse calculation can effectively reduce gradient waveform-induced excitation pattern errors [89, 90]. This has also been demonstrated in parallel excitation on an animal system with four Tx channels [91]. To date, parallel excitation with human subjects has been reported at field strengths up to 7 T using 2D [92] and three-dimensional [58] RF pulses, but to the best of our knowledge this has not been reported at higher field. Furthermore, we are not aware of k-space trajectory calibrations in humans for multi-Tx RF pulse design.

In this note, we report for the first time successful parallel excitation results in human brain at 9.4 T with eight Tx channels. For this implementation, it was necessary to measure the actual gradient waveforms in addition to ΔB_0 maps before designing 2D selective RF pulses (acceleration $\times 4$) to address severe distortion and blurring initially observed in excitation patterns. Experimental results were highly consistent with numeric simulations for both in vivo and phantom data.

4.2 Materials and Methods

All experiments were performed on a 9.4 T, 65-cm inner diameter bore human scanner (Magnex, Oxford, UK), equipped with a head gradient coil capable of a maximum gradient strength of 50 mT/m and maximum slew rate of 166 T/m/s. The scanner was driven by a console with eight independent Tx RF channels (Varian Inc., Palo Alto, CA, USA), each powered with a 500W RF amplifier (CPC, Brentwood, NY, USA). To ensure compliance with the FDA guidelines on specific absorption rate, the RF output power of each of the eight RF amplifiers was continuously monitored with an in-house-built multi-channel monitoring unit. Each RF amplifier was equipped with a directional coupler providing a 50dB attenuated version of the output waveform whose power envelope was continuously sampled by a calibrated analog-to-digital converter

board. The system was maintaining a 10-second and a 10-minute moving average and would immediately disable all RF amplifiers and terminate the MR pulse sequence if the mean power exceeded a predefined wattage threshold. Thresholds were conservatively determined against the worst case scenario assuming all RF coil electric fields to add constructively in the sample. Additionally, only small flip angle RF excitation with low level RF output power was utilized for in-vivo parallel excitation experiments. MR signals were acquired on eight independent receive (Rx) channels with a home built digital receiver system based on Echotek boards (Echotek, Huntsville, AL, USA). All computations, including RF pulse design and Bloch simulations, were conducted in Matlab (MathWorks Inc., Natick, MA, USA). Three healthy volunteers were recruited for this study, which was approved by the local institutional review board. All subjects provided written consent. Representative results are shown for one subject.

4.2.1 Parallel Excitation Measurements

All parallel excitation experiments were performed with an elliptical eight-channel transceiver stripline array, similar to the coil described in Ref. [93]. Each channel of the stripline array was used for both transmission and reception. A 16 cm diameter spherical saline phantom (NaCl 99 mM) doped with copper sulfate ($T_1 \approx 200\,\mathrm{ms}$) was used for preliminary measurements and demonstration of 2D parallel transmission.

4.2.2 Analytical Gradient Waveform Design

2D gradient waveforms (Gx and Gy), corresponding to a spiral excitation k-space trajectory, were designed for accelerated spatially selective excitation. Slew rate-limited gradient waveforms were first calculated based on G. Glover's algorithm [94] at the maximum available slew rate (166 T/m/s) to generate a spiral-in excitation k-space trajectory that radially undersampled the k-space by a factor of four (Fig. 4.1a and b). The fully sampled k-space corresponded to a field of excitation (FOX) of $16 \times 16\,\mathrm{cm}^2$ with a spatial resolution of 5 mm. Gradient ramps were appended at the beginning of these initially calculated gradient waveforms as they typically start with nonzero values on at least one axis. The resulting gradient waveforms had a total duration of 2.34 ms with a temporal resolution of $4\,\mu$s.

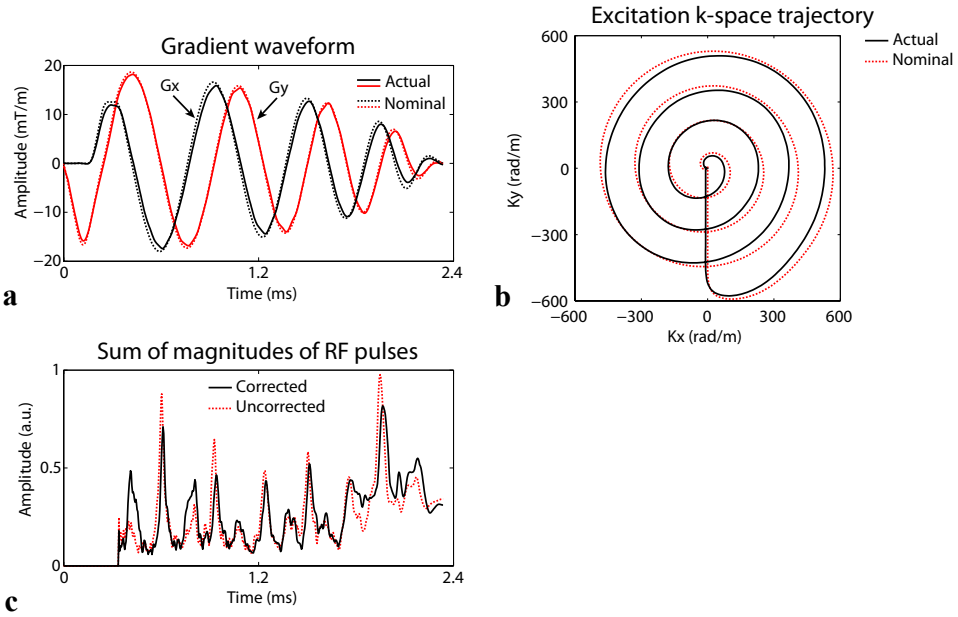

Figure 4.1: Gradient waveform and sum of magnitudes of RF pulses. (a) Nominal versus actually measured gradient waveforms. (b) Corresponding k-space trajectories. These slew rate limited gradients were designed for $\times 4$ acceleration (2.34 ms RF pulse duration). (c) Sum of magnitudes of the eight RF pulses based on nominal (uncorrected) and measured (corrected) trajectories. Note that no RF pulse was applied during the initial ramp of the gradient waveform. Also note the deviation of the actual k-space trajectories compared with their nominal counterparts, resulting in noticeable differences in shape between the sums of magnitudes of RF pulses.

4.2.3 Actual Gradient Waveform Measurement

Even with application of system pre-emphasis for eddy current compensation, significant distortion and blurring were found to be present in excitation patterns with 2D RF pulses based on spiral gradient waveforms calculated with the ideal analytical definition mentioned above. Thus, actual Gx and Gy were measured in separate experiments to identify potential gradient waveform deviations, using a self-encoding gradient method as previously described in Ref. [89]. This method relies on a modified gradient echo (GE) pulse sequence where the Cartesian encoding steps along the phase direction are replaced with a variable self-encoding pre-dephasing gradient followed by the gradient waveform to be measured used as a readout gradient during which the MR signals are sampled. Note that, as in [89], we measured Gx and Gy independently assuming no significant cross terms between the two. To limit induced eddy currents while providing whole excitation k-space coverage, the trapezoid self-encoding gradient had a long duration (11 ms) with limited maximum gradient strength. To improve automatic peak signal finding, homogeneous Tx and Rx B1 distributions were obtained using a small doped water tube (1 cm in diameter, 170 mM NaCl and 0.3 mM NiCl2, $T_1 \approx 1300\,\text{ms}$) set in the center of a one-channel ring shaped Tx/Rx RF coil of 15 cm in diameter. Slice selective acquisitions were obtained in an axial plane, in this single-channel Tx/Rx setup, with slice thickness = 5 mm, TR/TE =100/14.4 ms, bandwidth = 250 kHz, and 96 self-encoding steps. Similar to [89], reception k-space trajectories (Kx and Ky) were extracted from these data by locating the maximum signal values along the self-encode dimension. The peak position at each time point was determined by thresholding the magnitude signal to only contain its main lobe and fitting this lobe with a second-degree polynomial to find the position of its maximum. To minimize noise impact, ten data acquisitions were averaged before extracting k-space trajectories, yielding a total acquisition time of 6 min 24 s for both Gx and Gy characterizations. These trajectories were smoothed segment by segment, before calculating their time derivative to obtain the actual gradient waveforms. In addition, baseline k-space trajectories were obtained by running the same acquisitions (for Gx and for Gy), but without the application of the spiral gradient waveforms. These baseline trajectories, which are reflecting B0 inhomogeneities but not the actual gradient waveforms, were subtracted from the previously measured trajectories just before final waveform calculations.

4.2.4 Transmit B_1, Receive B_1 and ΔB_0 Field Mapping

In the multi-transmit setup, complex valued B_1^+ maps were obtained for each individual channel with a fast multi-channel B_1^+ mapping method introduced in [77]. With this method, eight relative B_1^+ maps (magnitude and phase), derived from a series of GE images collected in the small flip angle regime with one channel transmitting at a time, are combined with one absolute magnitude B_1^+ map, obtained in the large flip angle regime with all channels transmitting together. The eight small flip angle GE images (one per transmit channel) were acquired with TR/TE = 200/4 ms, slice thickness = 5 mm, FOV = $20 \times 20\text{cm}^2$, matrix size = 128×64, and acquisition time = 2 min 4 s. The large flip angle map was obtained using the Actual Flip Angle (AFI) method introduced by V. L. Yarnyhk [74] with TR1/TR2/TE = 28/140/4.6 ms, FOV = $20 \times 20 \times 7.5\text{cm}^3$, matrix size = $128 \times 64 \times 15$, and acquisition time = 2 min 40 s. Note that, to avoid areas with very low B_1^+ due to B_1^+ destructive interferences between Tx channels [83] when arbitrarily using the native phase of each RF channel without modification, local B_1^+ phase shimming was first calculated based on the eight relative B_1^+ maps as described in [29, 82] so that only one large flip angle AFI acquisition was needed (Fig. 4.2). The total acquisition time for B_1^+ estimations for the eight channels was 4 min 24 s. Figure 4.3 shows typical B_1^+ maps for both the phantom and human brain.

In addition to B_1^+ mapping, an estimation of the product (Rx B_1 profile $\times$ proton density) was derived from GE images which were acquired using the same RF phase B_1 shimming as for AFI based B_1^+ maps with about 15° flip angles in the center of the slice. Given the relatively short TR (150 ms) some degree of T_1 contrast bias is expected in the product estimation, especially in the brain because of long T_1 constant in tissues at 9.4T (Fig. 4.2c).

ΔB_0 maps were calculated from two GE images acquired at different echo times [95] (TE1/TE2/TR = 8/9/60 ms, FOV = $20 \times 20\,\text{cm}^2$, matrix size = 128×64), and were incorporated into RF pulse design, to minimize deteriorations of excitation patterns due to off-resonance effects [25, 26, 30].

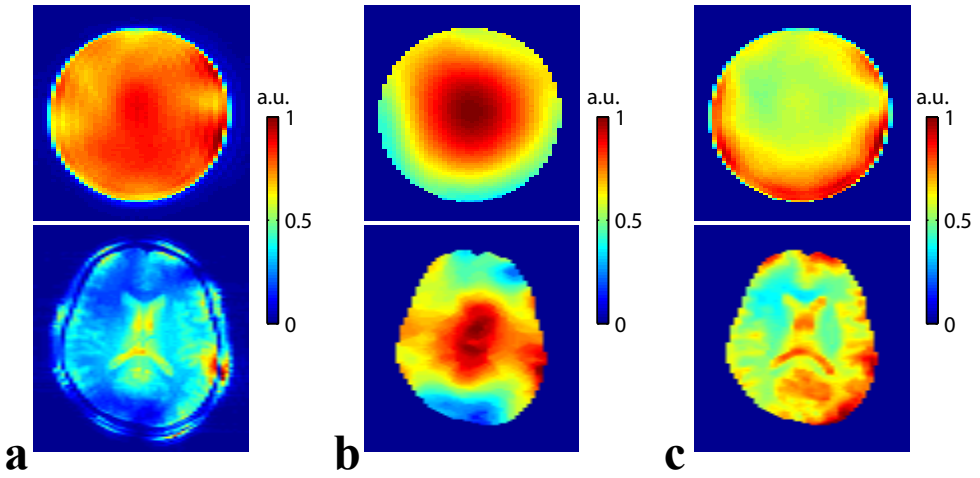

Figure 4.2: Gradient Echo (GE) images and B_1 profiles in phantom (top) and human brain (bottom) using a standard slice selective RF pulse. (a) Magnitude GE image (sum of magnitudes of the eight receive channels). (b) Transmit B_1 profile used for image acquisitions in (a). (c) Estimation of the product (receive B_1 profile $\times$ proton density) derived from (a) and (b). Note visible brain structures in this estimation (bottom in c) because of proton density and because of some degree of T_1 contrast due to long T_1 values in tissue at 9.4 T. In each of these acquisitions all channels were transmitting together using a same standard slice selective RF pulse.

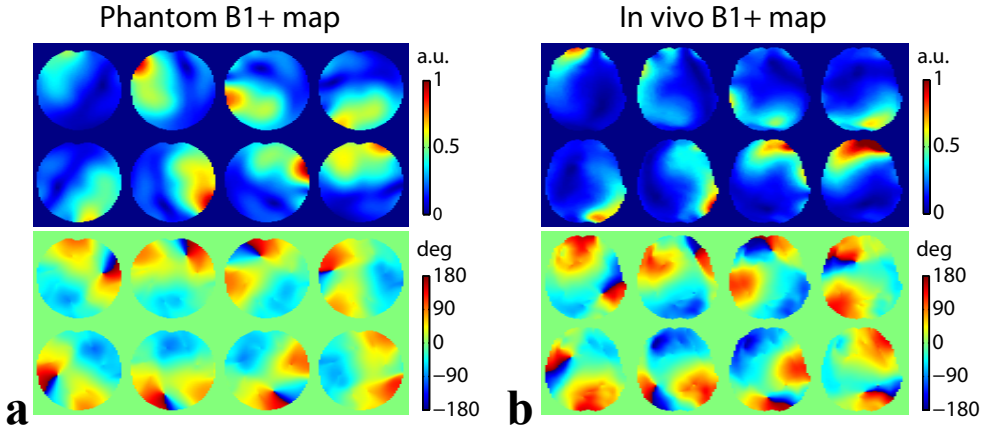

Figure 4.3: Absolute magnitude (top) and relative phase (bottom) transmit B1 maps of each individual transmit channel in an axial slice in the phantom (a) and in the human brain (b).

4.2.5 RF Pulse Design

In this study, parallel transmit pulses were designed in the small tip angle regime using Grissom's method [30]. The optimization problem was formulated to minimize the residual error $\|Ab - m\|_{(S,T)}$. Here, matrix A is generated based on the excitation k-space trajectory, the ΔB_0 map and B_1^+ maps; vector b represents the eight complex RF pulse shapes; vector m represents the desired excitation pattern; the diagonal matrixes S and T define a spatial mask for the region of interest and a temporal mask for RF pulsing, respectively. The minimization problem was solved for b using conjugate gradient (CG) iterations along with the L-curve criterion [25]. The desired excitation pattern was a rectangle with uniform flip angle and uniform phase distributions in a transverse plane, which was defined on a $20 \times 20\,\mathrm{cm}^2$ region with a 5-mm resolution. Pixels without spins (located outside the phantom or outside the brain tissues) were excluded from RF pulse calculations. RF pulses were set to zero during the initial ramp of the gradient waveforms.

To investigate the impact of gradient error on excitation patterns, uncorrected and corrected parallel Tx RF pulses were calculated using the ideal and actual gradient waveforms, respectively. In all cases RF pulses were designed with ΔB_0 correction.

4.2.6 Parallel Transmit Experiment

All images of parallel excitation patterns were acquired with a modified 3D GE pulse sequence where the slice selective excitation is replaced by accelerated 2D spatially selective RF excitation. Relevant acquisition parameters were: TR/TE = 150/4 ms, FOV = $20 \times 20 \times 20\,\mathrm{cm}^3$ and matrix size = $128 \times 64 \times 40$. Nominal flip angles were 17° for the phantom and 4° for human subjects. Maximum B_1 magnitude during the pulse was 5.2 μT in human brain and 8 μT in phantom. The resulting images were divided by the sum of magnitudes of eight estimated proton density weighted Rx B_1 profiles to mainly retain intensity variations due to RF excitation. In addition, flip angle distributions within the target rectangle were also mapped for the phantom, using AFI with TR1/TR2/TE = 28/140/4.6 ms, FOV = $20 \times 20 \times 20\,\mathrm{cm}^3$ and matrix size = $128 \times 64 \times 40$. This flip angle mapping was not performed for in vivo experiments because the limited source of RF power together with a larger load of a human head

than our phantom did not allow for large flip angles with the accelerated RF pulses. For each 500-W RF amplifier, only about 200W is available at the RF coil.

4.2.7 Simulations

A Bloch simulator was developed in the spin domain [96] and was used for calculating the excitation patterns corresponding to uncorrected and corrected RF pulses. To reproduce as closely as possible the experimental conditions, Bloch simulations were based on the actual gradient waveforms (rather than the ideal spiral counterpart) as well as on measured B_1^+ and ΔB_0 maps. As will be seen, a time delay was observed between the actual gradient waveforms on X and Y axes. In order to distinguish between shearing distortions typically induced in excitation pattern by such delay and other pattern distortions, additional simulations using uncorrected RF pulses were obtained where the measured gradient waveforms were corrected for the time delay between X and Y axes. Excitation patterns were defined on a $20 \times 20\,\mathrm{cm}^2$ FOX with a 128×64 matrix to match the experimental settings. All simulations assumed a uniform magnetization at equilibrium. Relaxation and diffusion terms were ignored.

4.3 Results and Discussion

The actual gradient waveforms were significantly different than their ideal counterparts, even though their overall pattern was similar (Fig. 4.1a). A delay of 12 μs was identified between the x and y gradient axes (y gradient events occurred earlier). In addition, actual gradient strengths were decreased by as much as 4% for Gx and 3% for Gy around the peak values of the waveforms. This resulted in significant k-space trajectory deviations (Fig. 4.1b), and the corresponding calculated RF pulses exhibited substantial differences, as illustrated when comparing the sum of magnitudes of uncorrected versus corrected RF pulses (Fig.4.1c).

For both phantom and in-vivo experiments, the experimental excitation patterns obtained with RF pulses that had been designed based on the ideal gradient waveforms suffered strong blurring and geometric distortions (Figs. 4.4 and 4.5). By contrast, using the actual gradient waveform for the RF pulse design provided significant improvement, resulting in excitation patterns matching very closely the target rectangle.

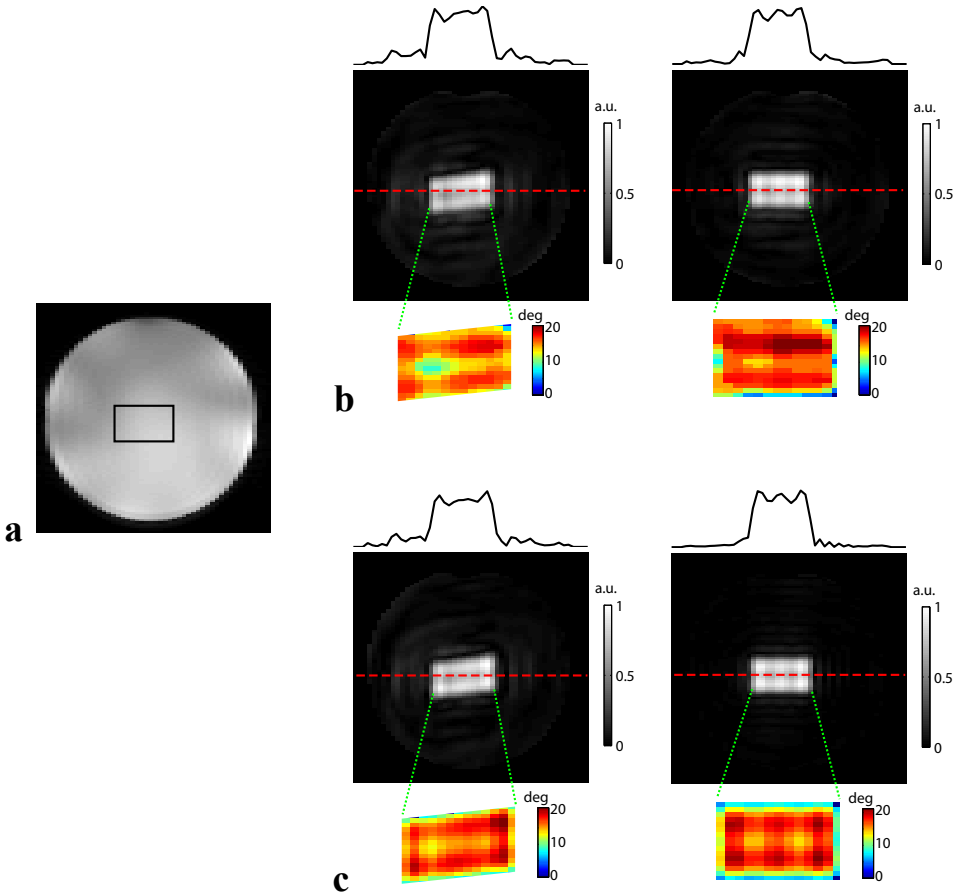

Figure 4.4: Comparison of RF pulse performances in the phantom. (a) Rectangle target (black box) overlaid on an axial image. (b) Experimental excitation pattern for uncorrected (left) and corrected (right) parallel transmit RF pulses ($\times 4$ acceleration, 2.34 ms). Excitation patterns were imaged with a 3D GE sequence using the accelerated RF pulse with nominal flip angle = 17°. Estimated receive B1 profiles were removed from the experimental images to mainly retain image intensity variations due to transmit B1. Plots above images display intensity profiles along the red dashed line. Maps in colors show flip angles within the rectangle target, acquired with actual flip angle imaging. (c) Corresponding results obtained with Bloch simulations based on same acquisition parameters. Note the good agreement between experimental results and simulations.

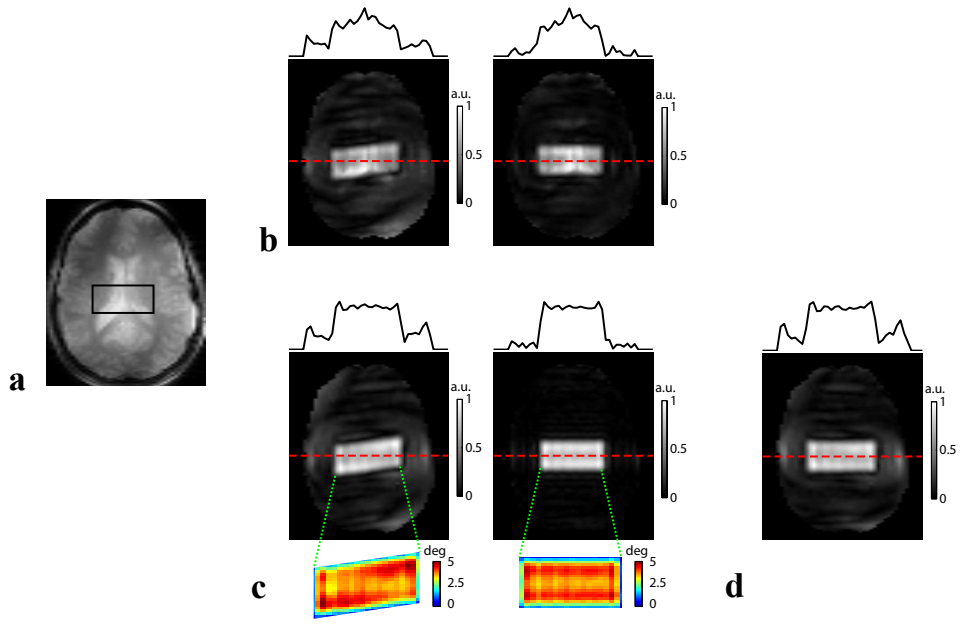

Figure 4.5: Comparison of RF pulse performances in human brain. (a) Rectangle target (black box) overlaid on an axial image. (Note that gray scales were adjusted to help visualize residual brain structures within the rectangle target, resulting in excessive darkness in other areas of the brain). (b) Experimental excitation patterns for uncorrected (left) and corrected (right) parallel transmit RF pulses ($\times 4$ acceleration, 2.34 ms). Excitation patterns were imaged with a 3D GE sequence using the accelerated RF pulse with a nominal flip angle of 4°. Estimated receive B1 profiles were removed from experimental images, although residual T1 contrast was present due to long T1 in brain tissues. Plots above images display intensity profiles along the red dashed line. (c) Corresponding results obtained with Bloch simulations based on same acquisition parameters. Maps in colors show simulated flip angles within the rectangle target. (d) Additional simulated excitation pattern using uncorrected pulses with the delay between gradient axes being compensated. Note significant improvement of excitation accuracy achieved using corrected pulses.

In addition, good agreement was observed between the experimentally obtained excitation patterns and the numeric simulations for both phantom and in vivo experiments (Figs. 4.4 and 4.5). Note, however, that these numeric simulations were strictly predicting excitation patterns, assuming homogeneous proton density and ignoring T_1 and T_2 relaxations. Because of long T_1 in brain tissues at 9.4 T, our in-vivo Rx B_1 estimation was partially contaminated with T_1 contrast, resulting in some visible brain structures (Fig. 4.5b).

Consistent with others' recent work [97] our results show that obvious errors in excitation pattern (mostly shearing distortion and blurring) can be effectively addressed using appropriate pre-calibration of excitation k-space deviation in RF pulse design. Note that all experiments were obtained using the standard pre-emphasis of the system for eddy current compensation. The corresponding gradient errors primarily concerned synchronization between gradient axes, which is expected to translate into shearing distortion, as well as gradient strength fidelity. Our simulations with uncorrected RF pulses show that correcting for the delay between X and Y gradient waveforms eliminated most the shearing distortion of the excitation patterns (Fig. 4.5d). However, strong blurring and fidelity errors still persisted after this correction, indicating that it was necessary to incorporate the whole measured gradient waveforms into the RF pulse design to restore excitation pattern fidelity. Note that, although we had satisfactory results using the peak finding approach for gradient measurements, other methods providing reduced acquisition time or increased SNR could be considered [98, 99].

With large susceptibility induced B_0 inhomogeneity, one could expect additional difficulty to achieve accurate excitation patterns in parallel excitation at 9.4 T in humans. In this study gradient deviations were however the dominant source of phase errors. The limited impact of B_0 inhomogeneity, despite the fact that B_0 shim was not used, was likely due to the relatively short duration (2.34 ms) of the accelerated RF pulses.

In summary, we have demonstrated successful accelerated 2D selective RF excitations in human brain at 9.4 T, currently the highest magnetic field available for human studies, with eight Tx channels in the context of gradient errors and without using B_0 shim.

Chapter 5

Adapted RF Pulse Design for SAR Reduction in Parallel Excitation with Experimental Verification at 9.4 Tesla

This is a manuscript submitted for publication to the Journal for Magnetic Resonance.

5.1 Introduction

Recently, there has been an increasing interest in using parallel excitation [20, 21] to accelerate multidimensional spatially selective RF pulses [16, 17]. This approach is especially promising to mitigate severe transmit (Tx) B1 inhomogeneities observed at high magnetic field [27, 58] where short T_2 and $T_2^\star$ relaxation constants impose stronger limits on RF pulse duration [25, 26, 30]. However, using shorter RF pulses for a given flip angle intrinsically tends to increase RF magnitude, resulting in higher specific absorption rate (SAR) deposition in tissue [32, 33, 40]. This is a serious concern at high magnetic field since larger RF power is needed to reach a given flip angle excitation at higher magnetic field [1].

It is therefore critical to develop accelerated RF pulse design methods capable of

limiting or reducing SAR levels. Most approaches that have been proposed in this direction can be separated in two groups. The first group relies on a fixed gradient waveform which is unchanged through the RF pulse design. Here, SAR limitation is obtained by RF pulse (but not gradient waveform) manipulation, based on solving an optimization problem using explicit RF pulse regularization [30, 100] or electrodynamic constraints [101, 102] while maintaining excitation fidelity. In the second group of methods, the gradient waveform or excitation k-space trajectory is altered in order to reduce RF peak magnitude in RF pulses, thus reducing SAR. In the implementation proposed by Graesslin et al. [103] the traversal rate of a chosen k-space trajectory is adapted based on filtered FFTs of the desired excitation patterns. This implementation however assumes RF waveforms and resulting excitation patterns to be linked by a direct Fourier transform, which is only verified with small tip angles, so it would not provide optimal RF pulses for large tip angles. Another implementation introduced by Xu et al. [104] relies on designing variable slew rate spiral gradients for reducing RF peaks based on initially calculated RF pulses. This method does not assume a Fourier transform relationship between RF pulses and resulting excitation patterns, and thus can be used with large tip angles. However, the corresponding formalism relies on an analytical representation of the initial gradient waveforms to calculate slew rate adjustments, thus it is restricted to certain gradient waveforms only.

We have proposed, in the second group of methods, a different implementation where the gradient waveform modulation allowing for RF peak power reduction is not calculated by explicitly altering the gradient slew rate [37]. Rather, the gradient amplitude is adapted similarly to the variable-rate selective excitation, or VERSE principle, initially introduced by Conolly et al. [34] for RF pulses with a single transmit channel. Our method can provide optimal RF pulse for any flip angle and can be used with any gradient waveform (it does not require an analytical description of the latter). We have previously reported numeric simulations at 7 T [37] and experimental verification in a phantom at 9.4 T [38] in the form of scientific conference abstracts. In this paper we fully describe this method, which is compared against simply stretching RF pulse and gradient waveform in the temporal dimension. Our results based on 2D RF pulses designed for 8 Tx channels and with $\times 4$ reduction indicate that substantial SAR reduction can be obtained with very limited increase in RF pulse duration.

5.2 Theory

5.2.1 RF Power Dissipation

The RF energy deposited into tissues during RF pulsing typically increases with the static magnetic field strength [1, 59–61]. In parallel excitation, the average SAR produced in a voxel at location $\mathbf{r}$ by an RF pulse of duration T with N Tx channels can be expressed as [63]:

$$\mathrm{SAR}(\mathbf{r}) = \frac{\sigma(\mathbf{r})}{2\rho(\mathbf{r})\,T} \int_0^T \left| \sum_{n=1}^{N} \tilde{\mathbf{E}}_{0,n}(\mathbf{r})\, \tilde{b}_{1,n}(t) \right|^2 \mathrm{d}t \tag{5.1}$$

where σ and ρ represent the conductivity and mass density of the scanned object, respectively. $\tilde{\mathbf{E}}_{0,n}(\mathbf{r})$ is the complex-valued E field of the n-th Tx channel driven by a unit current for a given load, and $\tilde{b}_{1,n}(t)$ is the complex-valued RF pulse applied through the n-th Tx channel.

5.2.2 Adapted-Rate Parallel Excitation

In this work we extend to multiple Tx channels and 2D RF pulse the VERSE principle introduced for 1D slice selective RF pulse with a single Tx channel by Conolly et al. [34]. The VERSE principle states that, ignoring relaxation and diffusion terms, changes in magnitude and duration of a magnetic field will not induce a change in the rotation of magnetization if the field surface (field strength $\times$ duration time) remains identical. Therefore, when an RF pulse is applied together with spatial encoding gradients (e.g., slice excitation), it is possible to simultaneously alter RF pulse shape and gradient waveform while retaining a same flip angle for on-resonance isochromats. On the other hand, as shown in Eq. 5.1, SAR is proportional to the time integral of the squared magnitude of the electric field induced by an RF pulse, indicating that RF pulses with lower peak values may give rise to less SAR for a given flip angle and pulse duration. Thus, high RF peaks can be suppressed with gradient waveforms modified accordingly to reduce SAR for a target flip angle. This simultaneous manipulation can be realized by introducing a time control function. Let $\tilde{B}_1(\mathbf{r}, t)$ and $\mathbf{G}(t)$ respectively denote the Tx B1 field and the multidimensional gradient waveform to be adapted. The adapted Tx B1 field $\tilde{B}_1^{\mathrm{ad}}(\mathbf{r}, t)$ and gradien waveform $\mathbf{G}^{\mathrm{ad}}(t)$ for the same flip angle can be given

by:

$$\tilde{B}_1^{\mathrm{ad}}(\mathbf{r},t) = \tilde{B}_1(\mathbf{r},\tau(t))\dot{\tau}(t) \tag{5.2}$$

$$\mathbf{G}^{\mathrm{ad}}(t) = \mathbf{G}(\tau(t))\dot{\tau}(t) \tag{5.3}$$

Here the time control function $\tau(t)$ has the same units of time and satisfies $\tau(0) = 0$ and $\tau(T^{\mathrm{ad}}) = T$ (T and T^{ad} are the original and adapted pulse durations, respectively.). The dot denotes the time derivative, and a tilde over the symbol indicates it's complex. The manipulations defined in Eqs. 5.2 and 5.3 do not change the surface of the net magnetic field (i.e., the time integral of the sum of RF and gradient related magnetic fields) and therefore retain the flip angle. Although the manipulation in Eq. 5.2 is applied on the total Tx B1 field, it can be directly translated to multiple Tx channels. In parallel excitation, since the relationship between total Tx B1 field and RF pulses is linear, the desired manipulation of the total Tx B1 field can be implemented by applying the same operation on individual RF pulses. Therefore, Eq. 5.2 can be replaced by a series of equations

$$\tilde{b}_{1,n}^{\mathrm{ad}}(t) = \tilde{b}_{1,n}(\tau(t))\dot{\tau}(t) \tag{5.4}$$

where $n = 1, 2, \ldots, N$, and N is the number of Tx channels. $\tilde{b}_{1,n}^{\mathrm{ad}}(t)$ and $\tilde{b}_{1,n}(t)$ are the adapted and original RF pulses for channel n, respectively.

5.2.3 Design of Time Control Function

A key task in adapted rate parallel excitation is to find a time control function that can limit the peaks of the resulting RF pulses. One possible way to design such a time control function is to attenuate and elongate the original RF pulse and gradient waveform whenever the corresponding level of SAR is too high. When a single Tx channel is used, SAR is directly proportional to the square of the RF amplitude $|\tilde{b}_1|$, thus it is possible to use a simple $|\tilde{b}_1|$ threshold above which RF output is considered too high. If we further assume that RF and gradient amplitudes are never to be increased, which is equivalent to say that $\dot{\tau}(t)$ can never be greater than unity, the time control function can be defined as:

$$\dot{\tau}(t) = \begin{cases} \frac{a}{|\tilde{b}_1(t)|} & \text{if } |\tilde{b}_1(t)| > a \\ 1 & \text{otherwise} \end{cases} \tag{5.5}$$

where a is a threshold which can in principle take any value in the range $(0, |\tilde{b}_1|_{\max})$. Naturally, lowering the threshold a yields RF pulse peaks that are further suppressed with lower SAR levels, but to the cost of longer RF pulse duration. The goal is to design a time control function with appropriate balance between SAR reduction and RF pulse elongation.

In the case of multiple Tx channels that are each playing a different RF pulse shape, SAR for each time point cannot anymore be expressed as directly proportional to a squared b_1 quantity. In theory, the only way to express SAR(t) is then to compute the net electric field produced by each complex $\tilde{b}_{1,n}$ combination in Eq. 5.1. But this would not be practical to calculate SAR reduction on-the-fly during an in-vivo MR experiment because electric fields cannot be mapped with current MRI techniques. One possibility is to utilize electromagnetic models, but the latter are highly depending on specific RF coil designs and on anatomical variations between subjects, so that such implementation would lack generality. Fortunately, we consistently observed in our numerical simulations, obtained with different RF coil designs, different excitation targets and different anatomical targets, a high correlation between the sum of the magnitude of $|\tilde{b}_{1,n}|$ through all Tx channels (SOM) and the corresponding spatially averaged total E field. We further verified that, in multi Tx RF pulse design, SOM can reliably be used to determine RF peaks that are too high, with the time control function now written as:

$$\dot{\tau}(t) = \begin{cases} \frac{a}{\mathrm{SOM}(t)} & \text{if } \mathrm{SOM}(t) > a \\ 1 & \text{otherwise} \end{cases} \tag{5.6}$$

5.2.4 Pulse Design

We propose to design adapted-rate parallel excitation RF pulses in three steps demonstrated here with spiral gradient trajectories which are most often chosen in parallel excitation given their high time k-space coverage efficiency. First, original parallel excitation RF pulses are calculated using slew rate limited gradient waveforms. Second, a SOM threshold is determined and gradient waveforms are modified using a time control function defined by the originally calculated pulses (Eqs. 5.3 and 5.6). Last, in order to retain excitation fidelity, the final adapted rate RF pulses are calculated based on

the new adapted gradients, rather than from direct manipulation of the original RF pulses with the time control function used for the gradient waveform. A critical reason for this choice is to account for B_0 inhomogeneities when designing adapted rate multi Tx RF pulses, especially at high field. Indeed, it is well known that adapted rate RF pulses are inherently sensitive to off resonance induced distortions [34]. Fortunately, in our implementation this issue can be addressed by explicitly including measured ΔB_0 information with the adapted gradient waveform during the final RF pulse calculation. Another reason is that the gradient waveforms obtained after Eq. 5.3 require further operations to be actually usable by the scanner (e.g., interpolation and smoothing in order to never exceed maximum slew rate).

5.3 Materials and Methods

All computations, except for electromagnetic field simulations, were performed in MATLAB (MathWorks Inc., Natick, MA) on a Pentium Linux workstation with 6 GB of RAM.

5.3.1 Pulse Calculation

All parallel excitation RF pulses were calculated using the spatial domain method [30]. The pulse design problem was formulated to minimize the residual error $\|Ab - m\|_{(S,T)}$. Here matrix A involves excitation k-space trajectory and B_1^+ maps; vector b contains individual complex RF pulse shapes; vector m represents the desired excitation patterns; diagonal matrixes S and T define a spatial mask for the region of interest (ROI) and a time window for RF pulsing, respectively. Practically, the ROI includes all voxels located inside tissues or phantom and excludes all pixels located in the air. This minimization problem was solved using conjugate gradient iterations, initialized with a zero pulse and terminated when the difference between two successive residual errors was less than a predefined value. RF pulses were calculated using spiral trajectories with excitation k-space undersampled by a factor of 4 ($\times 4$ reduction). All pulse designs excluded voxels outside the ROI.

5.3.2 Numerical Simulations

2D RF pulse design and corresponding 3D SAR computations at 7 T were obtained based on simulated electromagnetic field maps calculated with the XFDTD software (version 6.3, Remcom Inc., PA, USA) for an eight-element RF stripline transceiver array [28] loaded with a human head model provided with the XFDTD software ($2 \times 2 \times 2.5\,\mathrm{mm}^3$ resolution, Fig. 5.1).

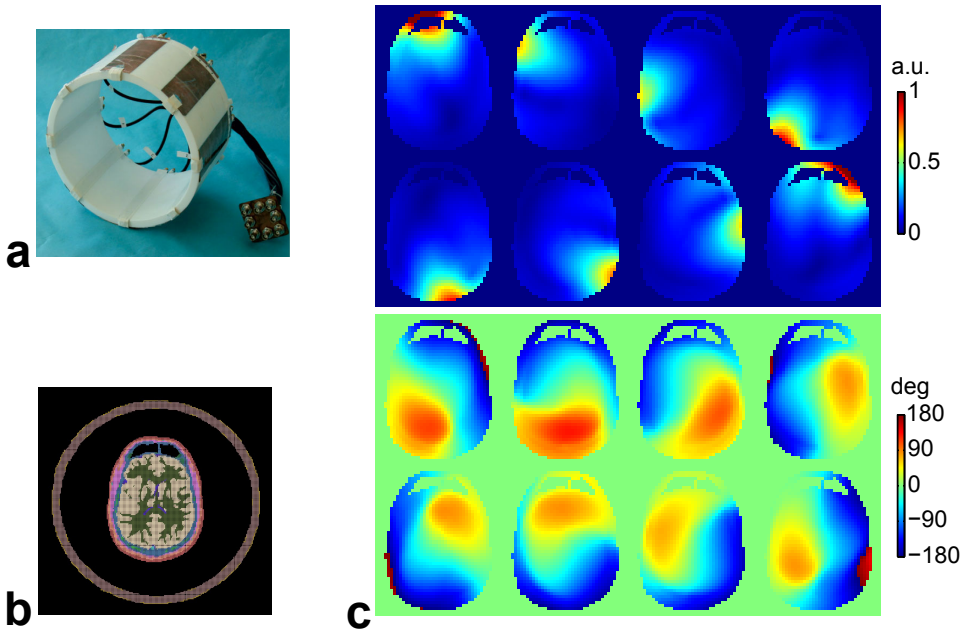

Figure 5.1: XFDTD simulations at 7 T. (a) Picture of the eight-channel transceiver array. (b) An axial slice of the FDTD model for the array in (a), loaded with a human head model. (c) Transmit B1 magnitude (top) and phase (bottom) maps of individual channels of the array.

Slew rate-limited gradient waveforms for 2D spiral k-space trajectory [94] were originally designed (Fig. 5.2) for $\times 4$ reduction (3.4 ms), assuming maximum gradient strength of 40 mT/m and maximum slew rate of 160 T/m/s. The fully sampled k-space corresponded to a field of excitation of $21 \times 21\mathrm{cm}^2$ with a spatial resolution of 4.4 mm. Three excitation targets in an axial slice of the head were considered: an oval covering brain tissues, a big ellipse in the middle, and a small ellipse on the right side. All patterns were defined on a 48×48 matrix in a $21 \times 21\mathrm{cm}^2$ region centered on the

gradient isocenter.

For each target, RF pulses were initially calculated using the originally designed gradient waveforms. The temporal average of the SOM of these original RF pulses was used as the threshold (parameter a in Eq. 5.6) in gradient manipulations since it was found to provide a good balance between SAR reduction and pulse elongation. Resulting adapted gradient waveforms were then used to calculate adapted RF pulses. Note that the modified gradient waveforms were re-sampled at a uniform sampling rate of $4\,\mu$s per dwell time to match format requirement on the scanner and were smoothed to not exceed the maximum slew rate before final RF calculations. For comparison, RF pulses were also designed using gradient waveforms that were simply stretched to reach the same duration as the adapted pulses by uniformly slowing down the original k-space traversal. The time control function used for this stretching manipulation was defined by the ratio of the pulse durations before and after adaptation, i.e., $\dot{\tau}(t) = T/T^{\mathrm{ad}} < 1$.

For each calculated RF pulse, Bloch simulations were conducted to evaluate excitation pattern fidelity and corresponding 3D SAR distributions were computed over the entire head, the neck and the top part of the shoulder. These 3D SAR maps were defined for a $52 \times 30 \times 30\mathrm{cm}^3$ volume of $260 \times 150 \times 120$ FDTD cells. SAR value for individual cells and subsequent masking were determined as follows. SAR was first calculated for each of the 12 edges of a cell based on simulated E fields and using Eq. 5.1 (the FDTD gridding defines E fields and tissue properties on the edges of cells). The average of these 12 SAR numbers was then assigned to the cell. SAR maps were further masked in order to only retain valid cells, defined as having their 12 edges with nonzero conductivity and mass density. Global SAR was calculated by summing SAR values of all valid cells in the head.

5.3.3 Experimental Verification

Experiments were performed on a 9.4 T, 65-cm inner diameter bore human scanner (Magnex, UK), equipped with a head gradient coil capable of maximum gradient strength of 50 mT/m and slew rate of 166 T/m/s. The system had eight independent Tx channels (DirectDrive, Varian, USA), each powered with a 500W RF amplifier (CPC, Brentwood, NY, USA). The system was also equipped with eight receive (Rx) channels with home-made digital receivers based on Echotek boards (Huntsville, AL, USA). An

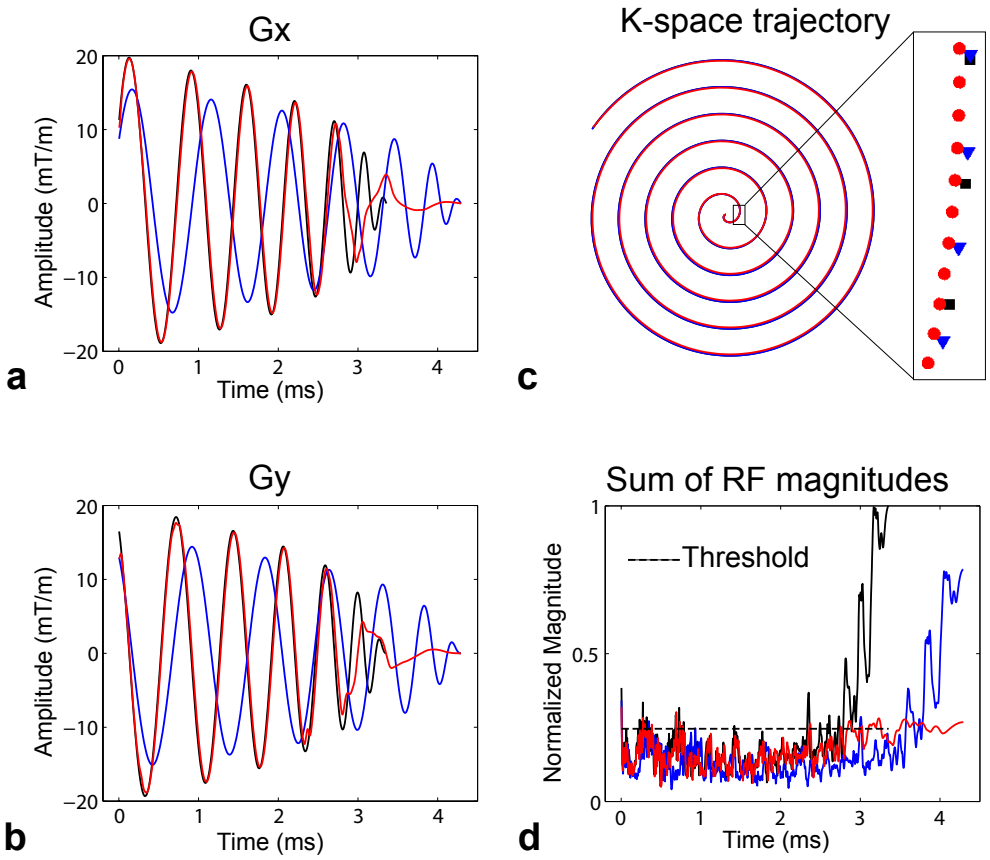

Figure 5.2: Parallel excitation RF pulse design using original (black), stretched (blue) and adapted (red) gradient waveforms. (a,b) Gradient waveforms. (c) Corresponding k-space trajectories. The inset on the right is the zoomed-in view of a trajectory segment showing the traversal paths followed by different traversal rates. Note that only subtle differences occur. (d) Sum of the magnitudes (SOM) of eight RF pulses designed with the three trajectories shown in (c). The time average of the original SOM (black) was used as the threshold for gradient adaptation. 2D RF pulses with $\times 4$ reduction were calculated for a large oval target using simulated transmit B1 maps as in Fig. 5.1. Note how the adaptive slowdown of k-space traversals effectively suppressed original large RF peaks.

elliptical eight-channel transceiver array [93] loaded with a spherical saline phantom (NaCl 99 mM) of 16 cm in diameter ($T_1 \approx 200\,\text{ms}$) was used in all experiments.

The complex B_1^+ maps (Fig. 5.6a) of the eight Tx channel were estimated by combining eight relative B_1^+ maps (magnitude and phase) and one absolute magnitude B_1^+ map [36, 77]. The relative maps were derived from eight gradient echo (GE) images collected at low flip angle with only one channel transmitting at a time, whereas the absolute magnitude map was obtained at high flip angle with all channels transmitting together using the actual flip angle technique (AFI) [74]. The eight GE images were acquired with TR/TE = 200/4 ms, slice thickness = 5 mm, and FOV/matrix = $18 \times 18\,\text{cm}^2/128 \times 64$. The AFI was obtained with TR1/TR2/TE = 28/140/4.6 ms, slab thickness = 25 mm, and FOV/matrix = $18 \times 18 \times 7.5\,\text{cm}^3/128 \times 64 \times 15$. The total acquisition time of B_1^+ estimation for the eight channels was 4 min 24 s.

Eight product $\rho \cdot |B_1^-|$ maps, with ρ being the proton density and $|B_1^-|$ the magnitude receive B1 profile, were also estimated from GE images, acquired with the same set of RF phases and magnitudes as in AFI based B_1^+ mapping, and normalized with the actual flip angle map. In addition, a ΔB_0 map was measured using two GE images acquired at different echo times (TE1/TE2 = 8/9 ms) and was incorporated into RF pulse design to minimize off-resonance effects [25, 26, 30]. Note that B_1^+ shim [29, 82] was performed before all field mapping to reduce substantial Tx B1 destructive interferences between channels [83] observed when using the initial arbitrary B_1^+ phase of each RF channel obtained after booting the system.

Initial slew rate limited gradient waveforms were designed with $\times 4$ reduction and max slew rate of 166 T/m/s resulting in 2.34 ms duration (Fig. 5.6b). The excitation target was a uniform square, defined on an $18 \times 18\,\text{cm}^2$ region with a 5-mm resolution. However, both original and adapted RF pulses were calculated with actual measured gradient waveforms to minimize degradations of excitation patterns due to substantial gradient errors on our system despite of active eddy current compensation [36]. For this purpose Gx and Gy were measured in an additional session using the method of Duyn et al. [99] which extracts k-space trajectories based on phase differences between two FID signals obtained from one slice with the test gradient turned on and off, respectively. In addition, for all gradient waveforms initial ramps were appended during which RF pulses were set to zero to reduce SAR.

With calculated RF pulses, excitation patterns were obtained from both experiments and simulations. Excitation patterns of original and adapted pulses were imaged using a 3D GE pulse sequence where accelerated 2D selective excitations had been included. Images were acquired with TR/TE = 150/4 ms, FOV/matrix = $18 \times 18 \times 18\,\mathrm{cm}^3/128 \times 64 \times 36$ and nominal flip angle = 10°. The resulting images were divided by the sum of magnitude of the eight estimated product $\rho \cdot |B_1^-|$ to mainly retain intensity variations due to RF excitation. Excitation patterns were also computed based on Bloch simulations, ignoring relaxation and diffusion terms. In all simulations, we used the measured B_1^+ and ΔB_0 maps and defined the excitation pattern on an $18 \times 18\,\mathrm{cm}^2$ FOX with a 128×64 matrix, to match as closely as possible the experimental conditions.

5.4 Results

In Fig. 5.2 are shown the original, stretched and adapted gradient waveforms and k-space trajectories as well as the corresponding SOM(t) obtained for eight-channel multi Tx RF pulse design at 7 T when a large oval ROI covering brain tissues was used as the target pattern. As can be seen in Fig. 5.2, adapting the gradient waveforms for RF pulse calculation was very effective in suppressing RF peaks (as defined by SOM(t)) exceeding a defined threshold in the originally calculated RF pulses. In our approach, adapted RF pulses and corresponding gradient waveforms are necessarily longer than original pulses because we start with the shortest possible pulses achievable in our hardware configuration. However, a direct comparison of SOM(t) in Fig. 5.2d indicates that RF peak suppression was significantly more efficient with adapted pulses than with pulses simply stretched to a same final RF pulse duration. As expected, in adapted RF pulses strong gradient slowdowns occurred where strong high RF peaks were observed in the initial RF pulses. One can notice that despite large variations in temporal sampling density, the k-space trajectory paths (ignoring traversal speed) were only marginally altered (Fig. 5.2c). Importantly, Fig. 5.3 shows that similar excitation pattern fidelity was obtained with original and adapted RF pulse design.

3D SAR maps were calculated in the whole head volume for two different 2D targets, using original, stretched and adapted RF pulses. Axial, sagittal and coronal views extracted from these 3D maps are shown in Fig. 5.4. A greater SAR reduction was

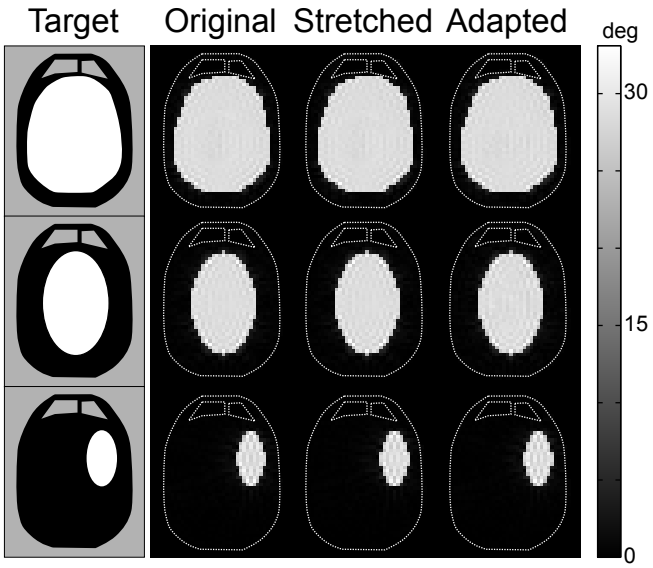

Figure 5.3: Simulated flip angle (FA) maps using RF pulses designed with original, stretched and adapted gradient waveforms. RF pulses, similar to those in Fig. 5.2, were designed for three targets (leftmost column) and were used in a Bloch simulator for FA calculations. In all displays for target patterns, white represents excitation of 30° flip angles with a uniform 0° phases, black indicates no excitation, and gray shows spin-free regions not considered in pulse design. Note that excitation accuracy was well preserved using adapted rate k-space trajectories for pulse design.

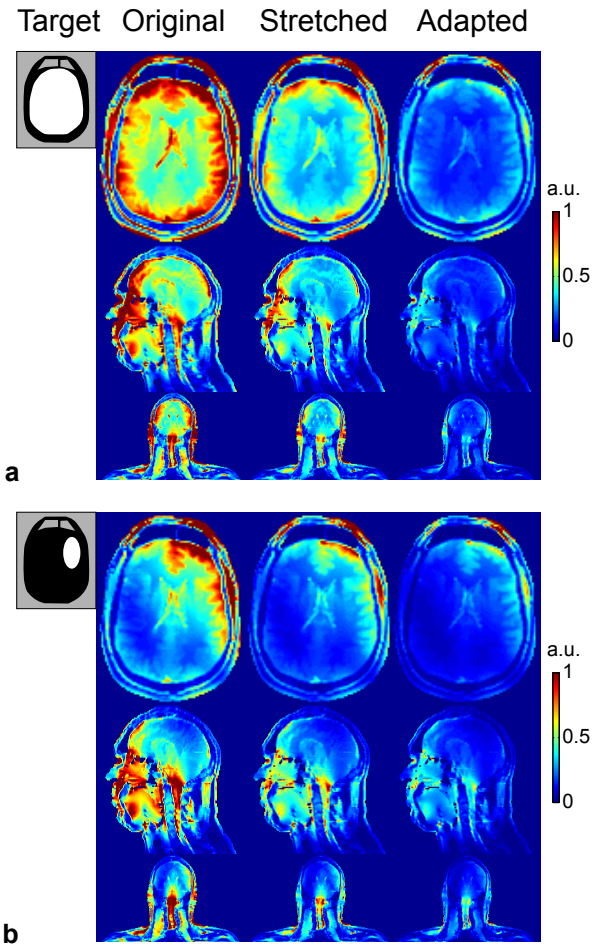

Figure 5.4: SAR distributions at 7 T of parallel excitation RF pulses designed for a large oval target (a) and a small ellipse target (b) based on electromagnetic simulations. RF pulses similar to those shown in Fig. 5.2 were used for these SAR computations. 3D SAR maps are displayed in three orthogonal views (axial: top row; sagittal: middle row; coronal: bottom row). Note the effective SAR reduction achieved using adapted rate k-space trajectories for RF pulse design.

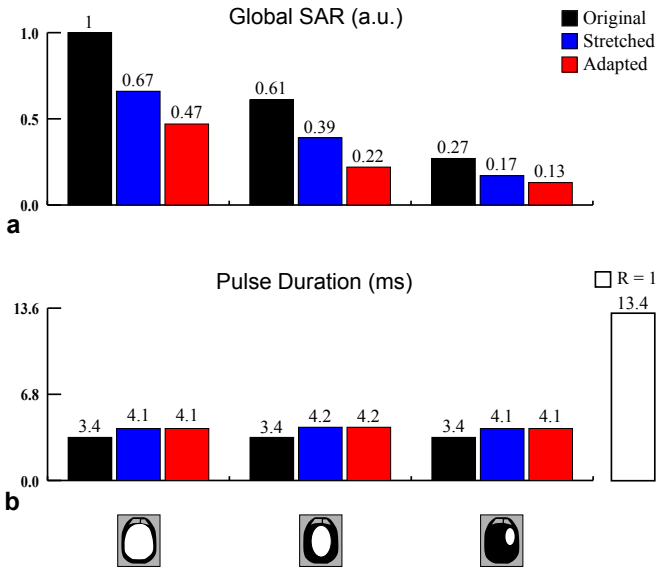

Figure 5.5: Global SAR values (a) and pulse durations (b) of RF pulses designed using original (black), stretched (blue) and adapted (red) gradient waveforms for three targets (shown at the bottom). Global SAR values were calculated by summing up 3D SAR quantities within the human head, neck and shoulders as shown in Fig. 5.4. The pulse duration for full k-space sampling without reduction (i.e., $R = 1$) is also shown in white for comparison. Note that SAR was effectively decreased using adapted rate k-space trajectories for pulse design at the cost of a slight increase in pulse duration.

clearly obtained with adapted rather than with stretched RF pulses. A quantitative comparison over the entire 3D SAR data is summarized in Fig. 5.5. Using adapted RF pulses effectively reduced SAR by as much as 64% at the cost of a slight increase in pulse duration, resulting in lower SAR levels than with stretched gradient for same pulse duration (Figs. 5.4 and 5.5). Even considering the slight increase in pulse duration, the RF pulses designed using adapted rate k-space trajectories for a reduction factor of 4 were still much shorter than those without reduction (4 ms vs 13.4 ms). Our experimental implementation of original and adapted RF pulses at 9.4 T with eight Tx channels confirmed that measured excitation pattern obtained with both pulses were closely matching the excitation target (Figs. 5.6 and 5.7).

5.5 Discussion and Conclusion

We have proposed and demonstrated an RF pulse design method for effective SAR reduction in 2D parallel excitation based on the variable rate principle initially described in VERSE for 1D selective excitation [34]. In the presented method, adapted RF pulses are calculated in three steps. First, an original RF pulse is designed with predefined fastest k-space trajectories. Adapted rate k-space trajectories are then calculated based on this reference. Finally, optimized RF pulses are re-calculated based on the adapted rate trajectories. Simulations at 7T showed that with this approach SAR was effectively reduced at the cost of a slight increase in pulse duration, with much greater efficiency than by simply stretching RF pulses and gradient waveform. Because our 7 Tesla installation does not yet support multi channel excitation, we made an experimental verification on a 9.4 T system equipped with 8 independent transmit channels. Our experiments showed that excitation patterns were not altered by the adapted low SAR RF pulses.

Compared with other methods previously proposed for reducing SAR in parallel excitation using gradient manipulation, our approach has several specific advantages. Unlike with k-space domain method [103], our gradient manipulations are directly based on calculated RF pulses without relying on the Fourier transform of the excitation patterns and hence can provide optimized pulses for arbitrary flip angles. Unlike the variable slew rate method [104], it adapts gradient amplitudes without requiring analytical gradient

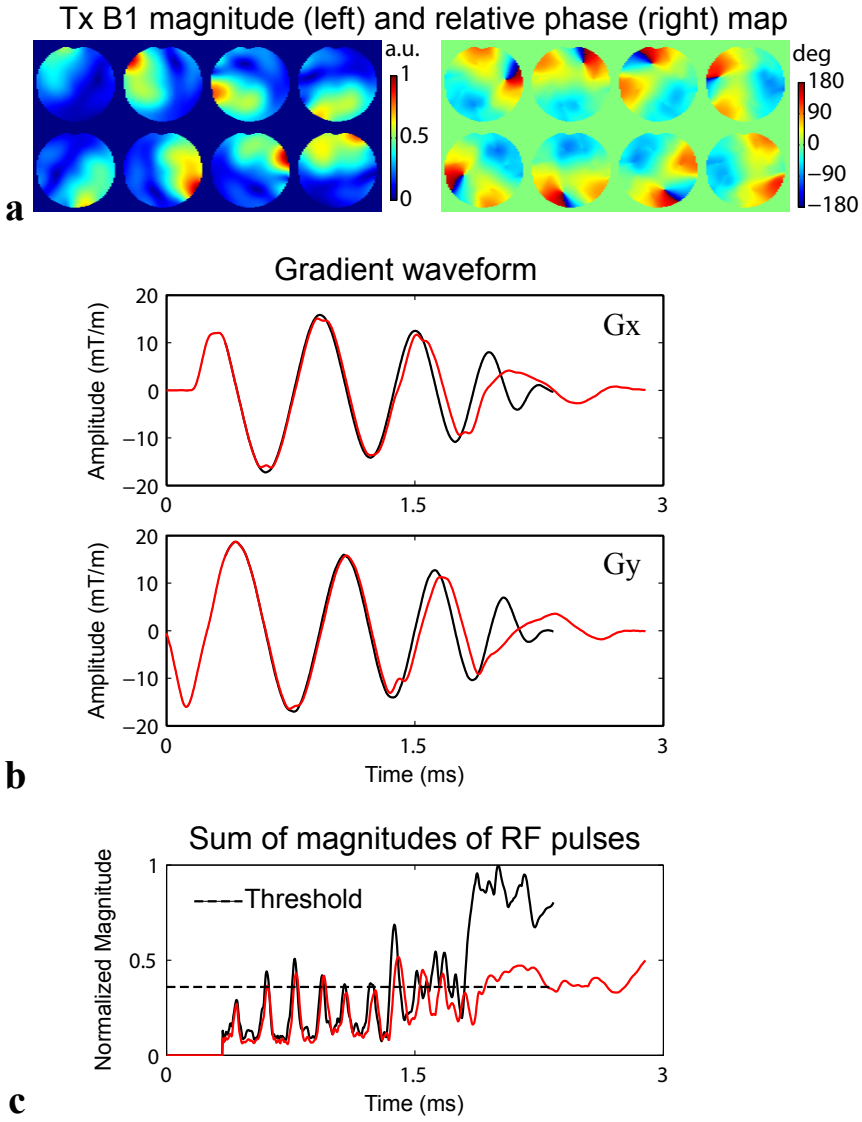

Figure 5.6: RF pulse design in experimental verification at 9.4 T. (a) Measured absolute magnitude (left panel) and relative phase (right panel) transmit B1 maps of the 8 channel RF coil loaded with a spherical water phantom. (b) Measured original (black) and adapted (red) gradient waveforms. (c) Sum of magnitudes of RF pulses calculated using gradients in (b). Both original and adapted RF pulses were designed for $\times 4$ reduction (duration = 2.3 and 2.9 ms, respectively).

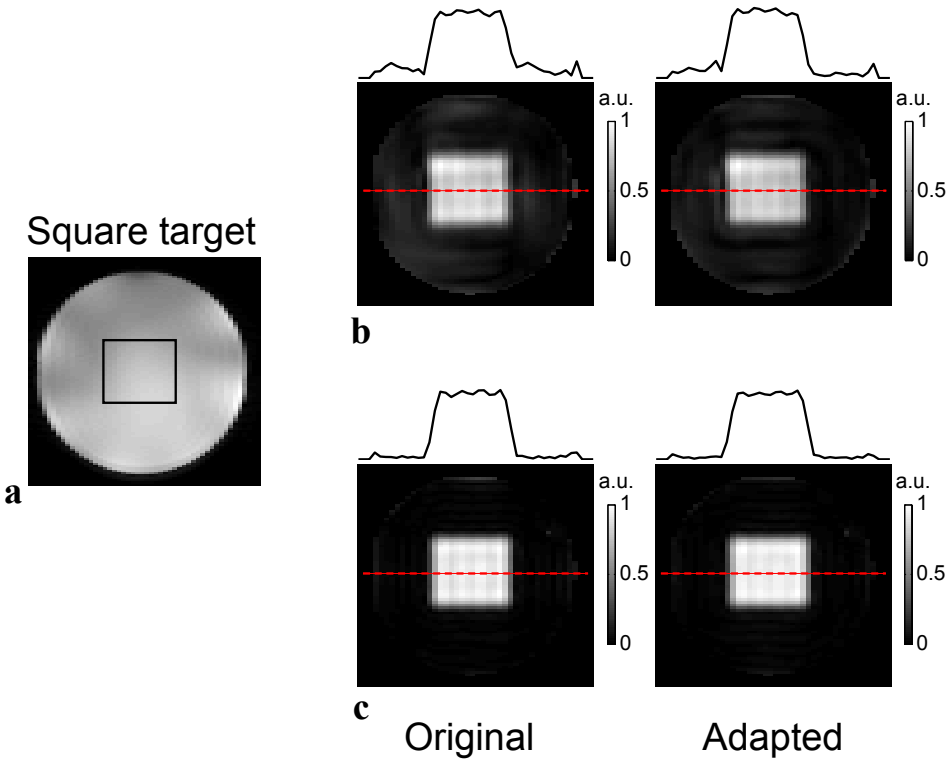

Figure 5.7: Feasibility of RF pulses designed using adapted rate k-space trajectories. (a) Square target (black box) overlaid on the image of the slice of interest (SOI). (b) Experimental excitation patterns within SOI for original (left) and adapted (right) RF pulses as in Fig. 5.6. Excitation patterns were imaged with a 3D GE sequence using accelerated RF pulses with nominal flip angle = 10°. Estimated receive B1 profiles were removed from experimental images to mainly retain image intensity variations due to transmit B1. Plots above images display intensity profiles along the red dashed line. (c) Corresponding results obtained with Bloch simulations based on same acquisition parameters. Note comparable performance between original and adapted RF pulses.

formulations and therefore can in principle apply to any type of gradient waveform.

In its current implementation our method also has a few limitations. First, it only includes decreases in gradient strengths, inevitably resulting in increased pulse duration. This corresponds practically to the hardware limits of our configuration as we always start with the shortest possible RF pulses, so k-space traversals can only be slowed down to not violate gradient slew rate limits. If original pulses (before adaptation) were not as short as possible, our final adapted RF pulses could be further shortened by speeding up k-space traversals during segments of lower RF amplitude in the original pulse. Second, our method requires RF pulses to be calculated twice, which in principle doubles the RF computation time. However, considering the constant increase in calculation speed on computers, it seems reasonable to assume that this should not constitute a significant limitation. It will also be very interesting to see whether including explicit regularization with SAR constraints in RF pulse minimization problem can bring further SAR reduction when used along with gradient adaptations in pulse calculations. The practicality of the latter approach will also benefit from increased computer calculation speed.

Chapter 6

New Developments in Progress

6.1 In-Vivo Parallel Transmission with 16 Channels

It has been shown that parallel transmission (pTx) [20, 21, 25, 30, 105], which consists of playing different RF pulses through independent transmit (Tx) channels, can be used to mitigate Tx B1 (B_1^+) nonuniformity and to achieve more homogeneous spatially selective RF excitation at high magnetic field. At this time, human scanners equipped with a Multi Tx console have typically a smaller number of Tx channels than Receive (Rx) channels (8 Tx channels is the most common configuration). There is however a growing body of evidence suggesting that better performance are expected when using a larger number of Tx channels [40, 101]. Of particular interest is the prospect of expanding multiple RF coils along the z axis [106], whereas so far almost all multi transmit experiments have been performed with multiple coil elements distributed along the X and Y axes. Although such "z-coil" have not yet been developed at 9.4Tesla in our center, we have at that field 16 channel strip line arrays with which we can experimentally implement 16-channel parallel excitation. We have previously reported a successful implementation of Transmit SENSE in the human brain at 9.4 T with an 8 Tx channel system, which required addressing methodological issues such as k-space trajectory inaccuracies and large susceptibility induced ΔB_0 [36]. Recently, our 9.4 T system has been upgraded with a 16 Tx channel console. Here we report preliminary results of 2D (Transmit SENSE) and 3D (Spoke trajectories) pTx in the human brain at 9.4 T using a 16-channel RF coil.

6.1.1 Materials and Methods

All experiments were conducted on a 9.4 T human scanner (Magnex, UK) driven by a console with 16 independent Tx RF channels (Varian, USA), each powered with a 500 W RF amplifier (CPC, USA). A 16-ch transceiver strip-line array [107] was used for both transmission and reception. Healthy volunteers were recruited for this study. All computations were performed in Matlab. In-vivo B_1^+ maps (Fig. 6.1) were obtained for individual channels using a fast multi-channel B_1^+ mapping technique [77]. ΔB_0 maps were derived from images acquired at two TE and were incorporated into RF pulse design to minimize off-resonance effects.

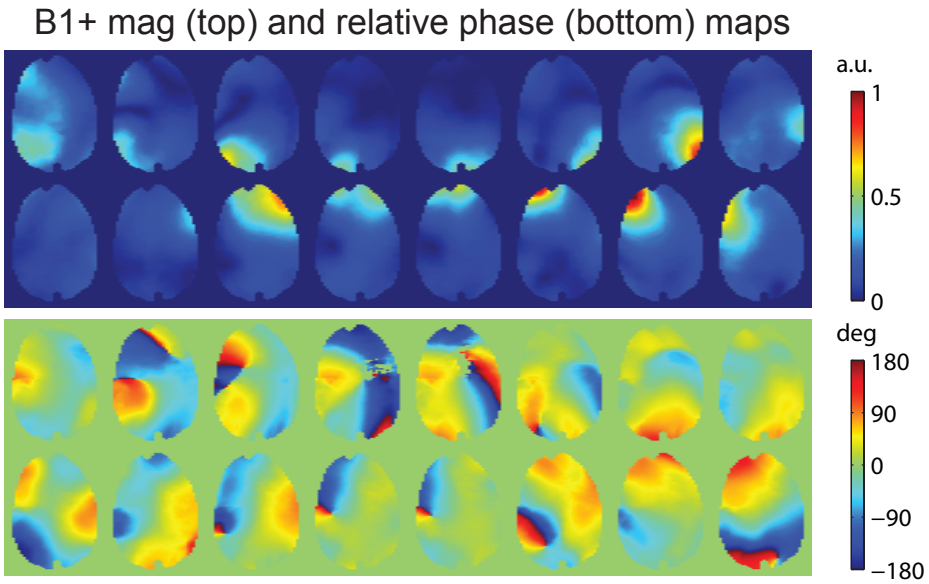

Figure 6.1: Transmit B1 map for a 16-channel transceiver coil.

All pTx RF pulses were designed in the small tip angle regime using the spatial domain method [30]. For 2D pTx experiments, RF pulses were calculated with a slew rate-limited spiral trajectory undersampling the k-space by a factor of 4 ($\sim$ 2.4 ms in length). Two target excitation patterns were considered in an axial slice of the brain: a rectangle and a logo "M", and the minimization problem defined to calculate b, the 16-RF pulse shape vector, was solved with conjugate gradient iterations. To correct for

excitation distortions due to gradient waveform errors, the actual, measured k-space trajectories were used for pulse design [36]. Excitation patterns were imaged using a modified 3D gradient echo (GE) imaging sequence. For 3D pTx experiments, slice-selective RF pulses were designed using a 5-spoke trajectory to mitigate B_1^+ inhomogeneity and achieve a more uniform excitation. The spoke placement was determined based on the Fourier transform (FT) of the desired in-plane uniform excitation. Spokes were placed where the 5 largest magnitude FT coefficients were found. The subpulses were defined as Gaussian RF shape RF pulses with a time-bandwidth-product of 2. Slice-selective gradients were designed for a slice thickness (full width at half maximum) of 5 mm. The total pulse duration was 4.5 ms (without the gradient rewinder). The complex weights corresponding to each spoke and to each Tx coil element were calculated using a magnitude least squares optimization [105] where the Tikhonov regularization parameter was determined by the L-curve criterion [25]. The k-space deviations that we previously demonstrated on our system were not taken into account for 3D pTx pulse design with spoke trajectories because our preliminary simulations did not show any noticeable impact of these gradient errors upon spoke based 3D RF pulses excitation pattern.

The resulting RF pulse for one channel as well as the corresponding gradient waveforms are shown in Fig. 6.2. The in-plane excitation pattern was imaged with a modified 2D GE pulse sequence. All data shown here were normalized by the estimated product [Proton Density] $\times$ [Receive B1 profile] ($\rho \cdot |B_1^-|$) in order to better identify the Tx B1 component.

6.1.2 Results and Discussion

Fig. 6.3 shows experimental excitation patterns for 2D pTx RF pulses designed with the measured k-space trajectory. The excitation patterns matched the target patterns, although some brain structures were visible. This is mostly due to residual T1 weight present in the brain images used for estimating $\rho \cdot |B_1^-|$ (long T1's are observed in brain tissues at 9.4 T).

Fig. 6.4 displays the excitation pattern (left) along with six intensity profiles (right) corresponding to the red dotted lines (left) for slice selective 3D pTx pulses. Overall B_1^+ homogeneity was satisfactory through the slice of interest, but one can notice that

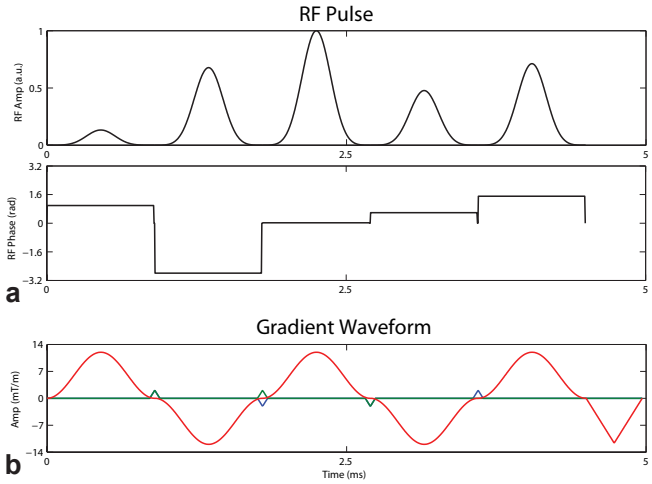

Figure 6.2: RF and gradient pulses for 3D pTx with 5 subpulses. (a) RF magnitude (top) and phase (bottom) for one transmit channel. (b) Gx (green), Gy (blue) and Gz (red) waveforms. Note that Gx and Gy consist of blips.

some areas of weak signals were still present. Based on our previous report on k-space trajectory inaccuracies in 2D Transmit SENSE RF pulses, one could naturally expect a similar source of artifact to be involved. However, in the present situation, including the measured k-space trajectories in the RF pulse design did not attenuate these defects, which is consistent with our simulations showing no significant impact of the measured k-space errors upon these 3D RF pulse excitation pattern. However, our k-space trajectory calibration was only concerned with Gx, Gy and Gz components and did not map global B0 components occurring with fast variations of Gx, Gy and Gz. We are hypothesizing that such B0 components (and/or higher order eddy currents) may be responsible for these k-space errors, especially considering the fact that the main oscillating gradient during the RF pulses is now Gz (by opposition only Gx and Gy were used during RF pulses in 2D Transmit SENSE) and that fast Gz switching is especially prone to generate B0 eddy currents. This verification however will require in the future the implementation of additional, specific calibration methods.

In conclusion, in this study preliminary results have been presented for in-vivo 2D and 3D parallel transmission at 9.4 T using a 16-element coil. These initial results are very promising, especially with 2D pTx, while additional calibrations may be required,

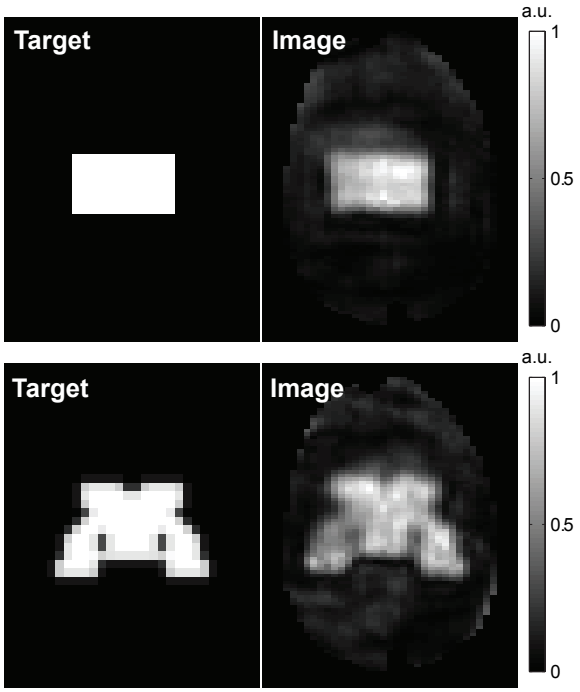

Figure 6.3: Excitation patterns for 2D pTx experiment. Two excitation targets (left) were considered. Some brain structures were visible in the imaged excitation patterns (right), mostly due to residual T1 weights. All pulses were designed with measured gradient waveforms to correct for phase errors due to k-space deviations.

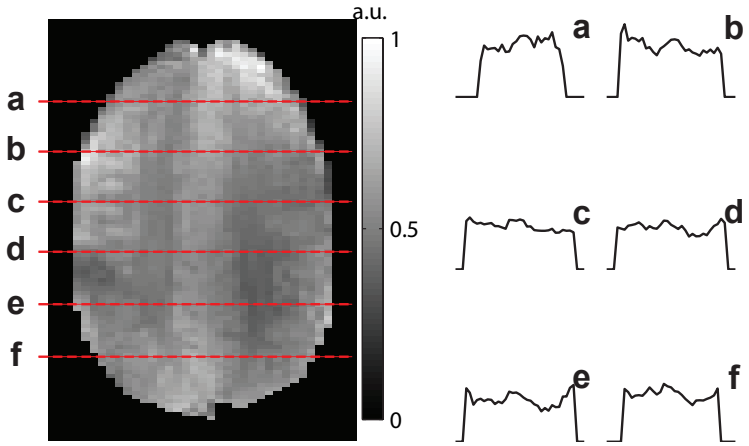

Figure 6.4: Imaged excitation pattern (left) along with six intensity profiles (right) for slice selective 3D pTx pulses. The red dotted lines on the left image show the locations of those intensity profiles on the right.

especially with regards to eddy currents, to obtain more homogeneous 3D pTx excitation patterns.

6.2 SAR Analysis for Transmit SENSE at 7T

Transmit SENSE [20, 21, 25] shortens multidimensional selective excitation by transmitting independent RF pulses through multiple channels. One useful application of Transmit SENSE is to compensate for transmit B1 inhomogeneity, especially at high field strength. However, the specific absorption rate (SAR) has to be considered in order to expand Transmit SENSE application in human studies. The relation between SAR behavior and different parameters of Transmit SENSE has been investigated using a phantom model [32, 33]. Besides the fact that shortening RF pulse duration inherently tends to increase SAR levels, other factors play important roles, especially with regards to RF coil design. In this study, we specifically investigated the impact of reduction factors, RF coil geometry and number of RF coil elements upon SAR behavior in Transmit SENSE at 7T with a human head model using electromagnetic field simulations.

6.2.1 Methods

Two 16-channel RF stripline arrays of different geometries were used in this study (Fig. 6.5). A larger one was mounted on a cylindrical holder of 32cm in diameter [108], while a smaller one was mounted on an elliptical holder of 24cm in major axis and 20cm in minor axis [109]. All RF coil elements were assumed to be completely decoupled. Transmit B1 and electric field maps within an axial slice of the brain for the two types of coil were obtained from simulations using the XFDTD software (REMCOM Inc., PA, USA). 2D-selective RF pulses for Transmit SENSE were calculated for a region of interest (ROI) using the spatial domain method [30] with a spiral excitation k-space trajectory designed with G. Glover's algorithm [94]. One example of such gradient waveforms is shown in Fig. 6.6b. The conjugate gradient algorithm was used to solve the minimization problem for RF pulse calculation. The desired excitation pattern consisted of a homogeneous excitation (30° flip angle) in the brain tissue through the whole slice of interest and was defined on a 48×48 matrix with a field of excitation (FOX) of 21cm (Fig. 6.6a). For each coil, RF pulses were calculated for different reduction factors ($R =$ 1, 2, 4, 8 and 16) with $N \geq R$. In order to evaluate the impact of the number of RF coil elements, a various number of RF coil elements (out of 16) were included for RF pulse design ($N = 4$, 8 and 16). Fig. 6.6c shows the resulting pulse duration as a function of reduction factor. Finally, the corresponding SAR behavior within the axial slice was calculated with Eq. 2.15, using the electric field maps from the simulation. All calculations were performed in MATLAB (The MathWorks Inc., MA, USA).

6.2.2 Results and Discussion

Fig. 6.7 shows the spatial distributions of the absorbed energy in the axial slice during a Transmit SENSE pulse for reduction factors of 1, 2 and 4 when transmitting through 16, 8 and 4 coil elements of different geometries. One can see that the overall absorbed energy increased with increasing reduction factor. Energy deposition tended to be more localized using the smaller coil as higher peak values were observed in the vicinity of coil elements.

Fig. 6.8 shows a plot of the absorbed energy versus the number of coil elements for different reduction factors and different coil geometries. Again, SAR consistently

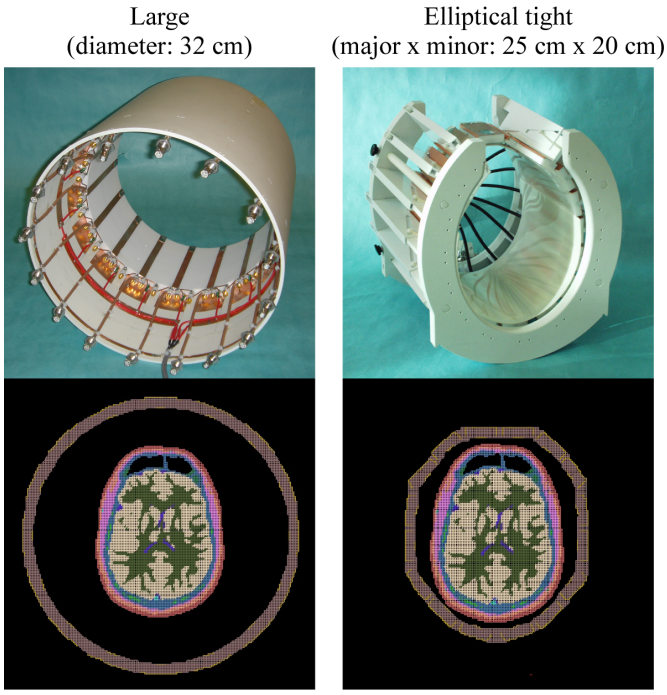

Figure 6.5: The 16-channel large (left column) and elliptical (right column) transceiver arrays for 7 T. (top) Pictures of the coils. (bottom) The Remcom models of the two arrays loaded with a human head tissue model.

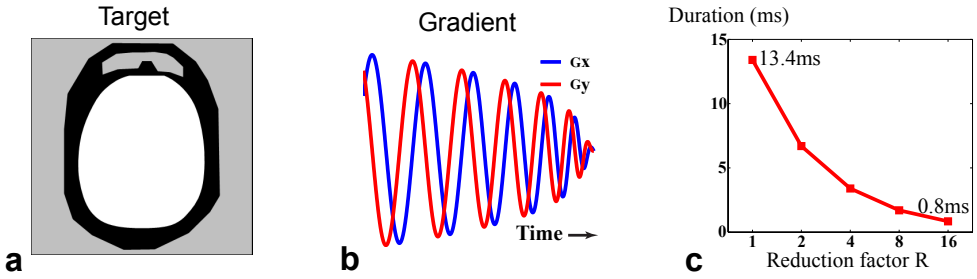

Figure 6.6: Pulse design specifications. (a) The target excitation pattern. Here white represents 30° flip angle and 0° phase, black is 0° flip angle and gray stands for spin-free regions. (b) One example of slew rate limited gradient waveforms. (c) Pulse duration vs. reduction factor.

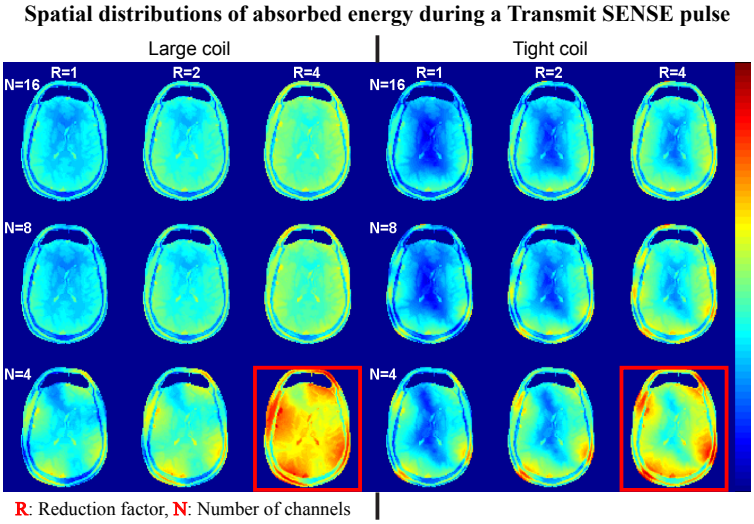

Figure 6.7: Comparison of energy distribution due to a Transmit SENSE RF pulse designed for different coil geometries, different number of channels and different reduction factors. All maps are in arbitrary unit and are displayed with a logarithmic color scale. The red box indicates that the corresponding excitation prole was of poor quality.

increased as the reduction factor increased. Overall, SAR decreased with increasing number of channels. However, SAR did not vary significantly from $N = 8$ to $N = 16$ for the large coil. In good agreement with Ref. [32], our data show that the absorbed energy decreases with larger N and increases with R, especially when the ratio N/R is small.

Note that in practice, we always consider no less than 4 Tx channels (i.e., $N \geq 4$) for parallel transmission in order to obtain short enough RF pulses with satisfactory performance. Although shown in Fig. 6.8 for illustration purpose, those cases where $N < 4$ will not actually be considered for experiments.

6.2.3 Conclusion

To conclude, both coil design (especially the number of channels) and the reduction factor have a strong impact on SAR distribution in the human head when using Transmit SENSE at 7 Tesla. Further investigations could determine which additional gain could be expected with even higher number of channels (i.e., $N > 16$) at 7 Tesla when using

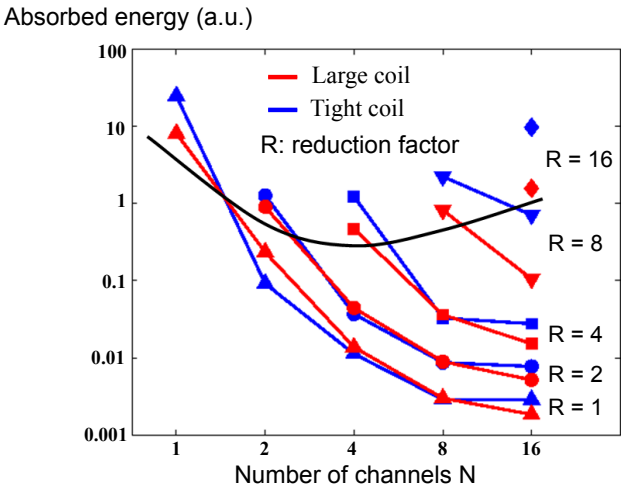

Figure 6.8: Comparison of spatially averaged energy due to a Transmit SENSE RF pulse designed for different coil geometries, different number of channels and different reduction factors. A poor quality was observed in the excitation profiles corresponding to the data above the black curve, and those data were not considered in the results.

a small coil. Our results also suggest, within the range of our parameters, an inverse relationship between SAR levels and the quality of excitation patterns, i.e., high/low SAR levels correlate to low/high excitation qualities.

6.3 AFI: From 3D to 2D

Recently, actual flip angle imaging (AFI) has been introduced as an efficient, fast 3D flip angle (FA) mapping technique [74, 84]. In some circumstance (e.g., 2D parallel transmission), a 2D version would be sufficient and thus will be preferable since 2D acquisition requires significantly shorter time than 3D acquisition. Although in the original 3D version the FA calculation in AFI [74] with non-selective excitations does not need to take into consideration the impact of slice profiles, this is however not the case when a 2D slice selective version of the same approach is considered. When using a 2D slice selective excitation, the slice profile of the RF pulse may result in incorrect flip angle values along with T1 bias. Therefore, the purpose of this study was to evaluate the properties and feasibility of 2D AFI where 2D (instead of 3D) image signals are used for FA calculations, using the equation that was derived for the 3D AFI. For this

purpose, we performed simulations and phantom experiments at 9.4 T to study the relationship between 2D and 3D AFI for different T1's.

6.3.1 Materials and Methods

In AFI, the acquisitions of two 3D images (I1 and I2) are interleaved playing two different repetition times (TR1 and TR2 = nTR1) for each imaged k-space line. The image ratio (r = I2/I1) is used to calculate the actual FA map with

$$\alpha = \arccos[(r \cdot n - 1)/(n - r)] \tag{6.1}$$

This equation is derived from a first-order approximation to the ratio formalism showing that the ratio r is independent of T1 contrast bias within an appropriate ratio between T1, TR1 and TR2. Eq. 6.1 was used for all FA calculations in this study after needed 2D or 3D image signals were obtained from experiments or simulations. As suggested in [84], we used TR1/TR2 = 25/125 ms (n = 5) with the average TR, $\bar{\text{TR}}$, being 75 ms. The total acquisition time was given by $T_{\text{acq}} = 2 \times \bar{\text{TR}} \times N_1 \times N_2$, where N_1 and N_2 are the numbers of steps along two phase encoding dimensions, respectively (note that in 2D acquisition N_2 is unity). Additionally, for optimal RF and gradient spoiling in experiments, the incremental RF phase was 35°, and the strong gradient spoiling regime was reached (where the areas of spoiling gradients were 225 and 1125 mT·ms/m during TR1 and TR2 delays, respectively).

Note that the validity of Eq. 6.1 requires image signals to be formed by a common FA, which is satisfied in 3D AFI. However, this requirement is generally not met in 2D AFI because signals in this case are from summation of all transverse magnetizations (Mxy) of different FAs through the slice of interest. As can be easily seen from the slice profile, the through-plane FA distribution corresponding to a RF pulse typically shows a nonlinear pattern. Therefore, 2D AFI using regular RF pulses is expected to provide incorrect and T1 sensitive FA measurements when using Eq. 6.1. Considering that RF pulses with an ideal, rectangular slice profile would generate a uniform FA distribution in slice selection excitation and thus result in an identical FA measurement in 2D and 3D AFI, the bias in 2D AFI may be reduced using RF pulses with a slice profile close as possible to a rectangle. In order to verify this impact of RF slice profiles on 2D AFI, three RF pulses with different slice profiles were designed: a gauss RF pulse, a sinc pulse

with, and a SLR RF pulse. The gauss pulse was generated cutting off a mathematical gaussian curve at the two points whose magnitudes were 1% of the maximum, the sinc pulse was designed to have six lobes on each side for a rectangular slice profile at low flip angles, and the SLR pulse was calculated for a nominal FA of 10° using the FIR filter design approach [110]. All pulses were 3 ms in length. The gaussian and the SLR pulses were also used to obtain experimental and simulated 2D and 3D AFI values.

The FA mapping experiments were conducted using an elliptical 8-channel transceiver stripline array [9, 28] and transmitting through all channels together. In order to demonstrate the T1 induced bias in 2D FA measurements, two doped water phantoms with different T1 values were utilized: a sphere (1.8 L, T1 = 220 ms) and a cylinder (1 L, 10 cm in diameter, T1 = 1330 ms). Two TR signals from the slice of interest were obtained using a modified 2D or 3D gradient echo (GE) pulse sequence. Slice thickness was respectively 2 and 4 mm for the gauss and SLR RF pulses in 2D AFI. In 3D AFI, a slab selective RF excitation with a slab thickness of 20 cm was exploited in order to reduce the impact of ΔB_0. 3D AFI was acquired with a 1 mm resolution along z direction. With this configuration, the signal at a particular location within the central slice of interest can be viewed as being formed with the same FA. The acquisition time was much shorter in 2D AFI than in 3D AFI (11 sec vs 10+ min, 2D AFI was more than 60-fold faster). Note that before FA mapping, local B1 phase shim [77] was performed on a central region within the slice of interest in order to improve Tx B1 efficiency.

Numerical simulations with experimental parameters were performed for slice select excitations in an AFI sequence, assuming ideal RF and gradient spoiling. We utilized the same gradient waveforms generated by the scanner, including the rewinding lobes. Multiple simulations were obtained with the nominal FA (for on-resonance isochromats) ranging from 10° to 90° with a step of 5°. For each nominal FA, the distribution of steady-state Mxy was simulated with a spatial resolution of 0.05 mm along the slice select direction in order to be able to determine the actual FA for each location along the slice profile without noticeable partial voluming effect. In order to generate image signals corresponding to experimental acquisitions with the AFI sequence, complex Mxy values were then summed along the slice selection axis within a centered bandwidth of 40 mm and 1 mm thickness for 2D and 3D AFI's, respectively.

6.3.2 Results and Discussion

As expected, for a given flip angle the sinc pulse needed much more power than the two other RF pulses (Fig. 6.9a). This is due to the fact that we used a 6 lobes (each side) sinc RF pulse of only 2ms duration, which requires far more RF peak power. This high power requirement made this sinc RF pulse not usable in practice, and we did not include it in experimental verifications. Note that based on simulations a standard 3 lobes (each side) sinc RF pulse behaved so poorly with regards to AF mapping with the AFI sequence that we did not use the latter either.

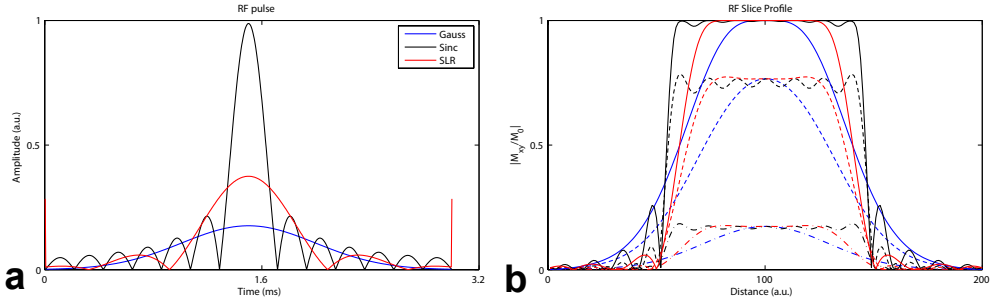

Figure 6.9: RF pulses (a) and their slice profiles (b). The RF pulse amplitudes shown in (a) were normalized to generate the same flip angle. The slice profiles were obtained for nominal flip angles of 10° (dash dotted curve), 50° (dashed curve) and 90° (solid curve).

As can be seen in Fig. 6.9b, at low flip angles ($\sim 10°$), the sinc pulse provided the most uniform profiles, the gauss pulse the least uniform and the SLR pulse in between. However, as the flip angle increased, side lobes arose dramatically with the sinc pulse and were expected to play a significant role in signal formation. By contrast, side lobes were still well suppressed with the SLR pulse at large tip angles, indicating that the SLR pulse will be the best choice of the three for 2D AFI.

The relationship between 2D and 3D AFI FA values was closely matched by our simulations (Fig. 6.10). As expected, 2D AFI provided different and T1 sensitive FA measurements. This difference and T1 sensitivity were reduced using the SLR pulse with a better slice profile. Interestingly, the difference in FA between 2D and 3D AFI's increased with longer values of T1.

In summary, FA mapping based on 2D AFI has been studied and characterized

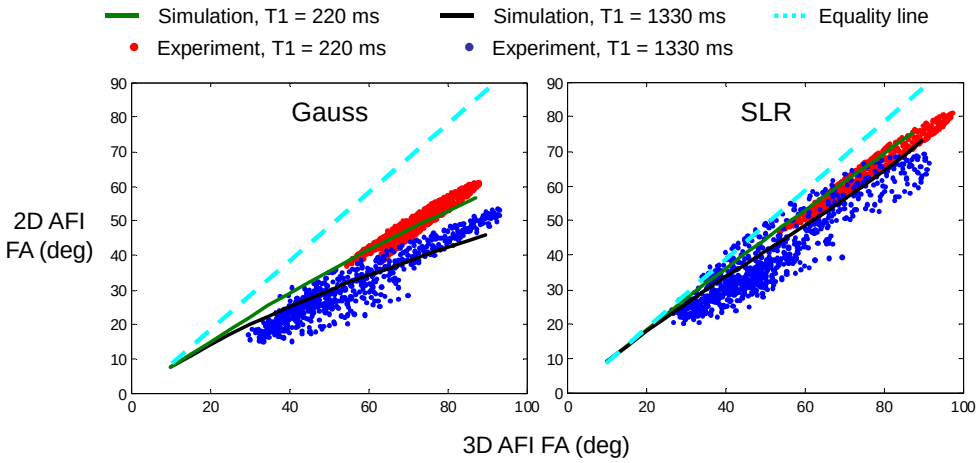

Figure 6.10: 2D vs 3D AFI using a gauss (left) and a SLR (right) RF pulse.

using experiments and simulations. Although the measured FA maps within the slice of interest by 2D AFI presented global patterns similar to those by 3D AFI, the FA values obtained with 2D AFI were deviated from the nominal ones due to the RF pulse profile. Our results also indicate that the FA bias (including T1 sensitivity) in 2D AFI can be reduced using RF pulses with an optimal slice profile (i.e., a slice profile close as possible to a rectangle) over the FA range of interest.

6.4 Single-Shot 2D OVS Pulse Design

Outer Volume Suppression (OVS) is a technique mostly used in spectroscopy to saturate unwanted MR signals spatially located outside of a volume of interest. Typically, OVS is performed with multiple conventional (e.g., sinc) pulses and may suffer from low efficiency and high Specific Absorption Rate (SAR). This is especially true in the case of heterogeneous transmit B1 profiles where it is often necessary to include multiple OVS RF pulses with variable flip angles, in a very short time in order to avoid T1 relaxation. A new OVS RF pulse design, consisting of a constant frequency offset RF pulse applied together with sinusoidal temporal gradient modulations, has been recently introduced [111]. This technique greatly benefits from the high RF efficiency typically associated with frequency sweep RF pulses [14]. It was experimentally demonstrated

that this technique allows, in a single RF excitation, for circular and elliptic shaped 2D OVS patterns. We believe that this technique could strongly benefit from multi channel transmission by optimizing RF efficiency over the spatial location concerned with the bandwidth subjected to the peak of frequency sweep for each time point of the RF pulse. However, even in a single transmit channel setting, it remains challenging to rapidly alter the geometry of these patterns and recalculate on the fly the corresponding RF pulse and gradient waveform. This flexibility is absolutely required in human brain studies in order to match OVS patterns with anatomical targets defined for each patient and must be solved before one could consider multi transmit algorithms. Here, we introduce a new algorithm to calculate the design of these pulses, capable of large geometry adjustment and of preserving a constant OVS width. We verify experimentally its properties in a phantom on a human 9.4 T scanner.

6.4.1 Pulse Design Principle

An RF pulse with constant magnitude and time varying offset frequency is applied with a time varying 2D gradient in order to achieve RF excitation along a curved target. The time-dependent gradient continuously reorients the plane of frequency selection in space. This, together with the appropriately designed RF pulse, creates the proper condition to accomplish rapid passage [112] in a spatial location moving along a curved trajectory. We need to define the gradient strength (G_x, G_y), the gradient orientation and the RF offset frequency. To preserve a constant curve thickness (bandwidth), we constrain the net gradient strength $G = (G_x^2 + G_y^2)^{1/2}$ to be constant and calculate it with $G = s \cdot (T_\mathrm{p}\, w)^{-1}$; here s is an empirically determined scaling factor, and T_p and w are the desired pulse duration and bandwidth, respectively. We apply the gradient and RF in such a way that, at each time point during the pulse, the on-resonance isochromats are disposed along a plane tangent to the curve. With the origin at the gradient isocenter, this problem becomes: given a point on a curve, find the tangent line at that point and the distance from the origin to this tangent line. The orientation of the gradient is perpendicular to this line, while the distance defines the RF offset

frequency. Let's assume for example an excitation curve defined by an ellipse

$$x(t) = a\cos\theta(t) + x_0$$
$$y(t) = b\sin\theta(t) + y_0$$

where t is the time variable (Fig. 6.11). In this case, the gradient orientation and the distance become

$$\phi(t) = \arctan[ab^{-1}\tan\theta(t)]$$

and

$$r_B(t) = [ab + ay_0\sin\theta(t) + bx_0\cos\theta(t)] \cdot [a^2\sin^2\theta(t) + b^2\cos^2\theta(t)]^{-1/2},$$

respectively. The gradient waveforms are then given by $G_x(t) = G\cos\phi(t)$ and $G_y(t) = G\sin\phi(t)$, and the RF offset frequency by $\omega_{\mathrm{rf}}(t) = -\gamma G\, r_B(t)$.

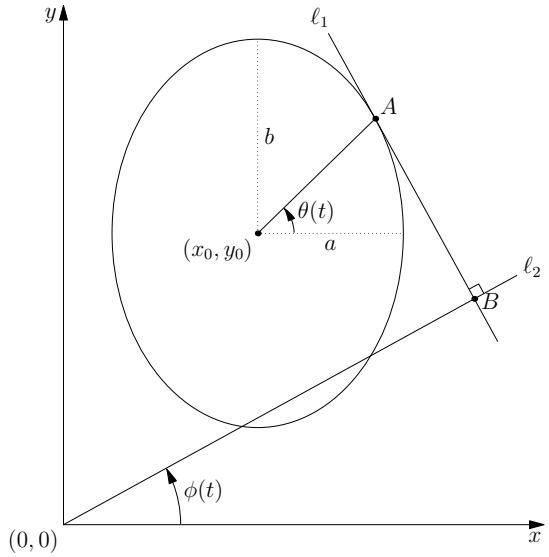

Figure 6.11: Illustration of single-shot OVS RF pulse design

6.4.2 Materials and Methods

For demonstration purpose, we imaged the OVS excitation pattern rather than the corresponding suppressed signal. An 8-channel RF transmit (Tx), 9.4 T human scanner was used (Varian, USA). An elliptical 8-channel transceiver RF array [9, 28] was loaded

with a 1.8 L spherical doped water phantom. Gradient and RF pulses were designed with a constant angular velocity of on-resonance traversal on the ellipse (i.e., $\theta(t) = \omega t$). We designed OVS patterns of different shapes, sizes, positions and bandwidths within an axial slice of 14 cm in diameter. The main specifications for those pulses are displayed in Table 6.1, where the numbers in bold show the parameters that differed from a reference ellipse (first column). $T_{\mathrm{p}} = 2\,\mathrm{ms}$, unless specified otherwise. Excitation patterns were experimentally imaged using a spin echo (SE) sequence where the slice selective excitation module was replaced with the OVS excitation (slice thickness = 5 mm, FOV = $20 \times 20\,\mathrm{cm}^2$, matrix = 128×64, TR/TE = 300/26 ms). Tx B1 heterogeneity was mitigated with static B1 shimming [113]. A regular SE image with sinc RF excitation was also obtained with the same imaging parameters in order to appreciate image intensity variations due to B1 field inhomogeneities. Numerical simulations of the excitation patterns were performed assuming a uniform B1 in the image plane.

(cm)	Ref ellipse	Circle	Big ellipse	Shifted ellipse	Thick ellipse
a	3.5	3.5	**5.5**	3.5	3.5
b	2.5	**3.5**	**4.5**	2.5	2.5
w	1	1	1	1	**2**
x_0	0.1	0.1	0.1	**1.4**	0.1
y_0	-1.4	-1.4	-1.4	**0**	-1.4

Table 6.1: Main specifications for pulse design. The numbers in bold show differences than the specifications of the reference ellipse.

6.4.3 Results and Discussion

Based on those calculations, the RF offset frequency continuously varied through time, and the gradient waveforms were not pure sinusoids (Fig. 6.12).

Numerical simulations closely matched the experimental results (Fig. 6.13). Residual differences between the two were mostly attributed to ΔB_0 and gradient imperfections which were not addressed in this preliminary study. As expected, image intensity variations due to RF coil B1 inhomogeneity (Fig. 6.13a) were consistently observed in all images. It should be emphasized that even in this work RF pulses are designed to obtain saturation (90° flip angle) in the rapid passage regime; they are not however used in the adiabatic condition typically chosen to obtain a homogeneous inversion immune to

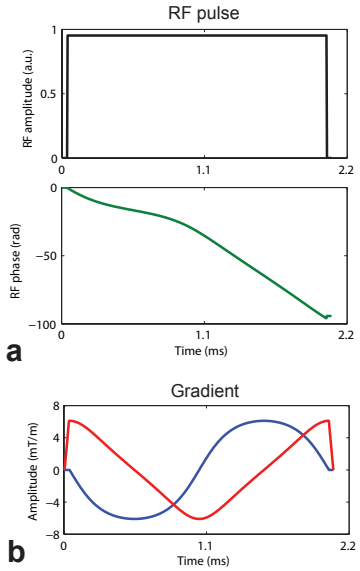

Figure 6.12: An example of designed RF and gradient waveforms. (a) RF amplitude (top) and phase (bottom). (b) Gx (red) and Gy (blue).

transmit B1 heterogeneity. Here, the resulting magnetization does vary as a result of transmit B1 heterogeneity. It will be interesting to determine whether such transmit B1 inhomogeneity induced variations can be addressed by embedding dynamic B1 shim in the pulse design, modulating RF phase and magnitude of each channel through time. Another expected source of signal non-uniformity was the varying excitation traversal rate along the ring, which may be addressed with a constant traversal speed of excitation target. As previously shown, periodic concentric excitation rings were generated outside the first, main excitation ring (Fig. 6.13b-k). However, when using OVS RF pulses in vivo to suppress signal from the skin, only this innermost ring is of interest and the other ones can be ignored. Increasing the bandwidth decreases the gradient strength, and thus increases sensitivity to ΔB_0. Therefore, a shorter RF pulse was utilized (1 ms instead of 2 ms) for the thicker ellipse pattern (Fig. 6.13f). Although an ellipse was used in the current study, the algorithm could be used to obtain any convex curved pattern and extended to account for ΔB_0.

In conclusion, we have introduced a new method to calculate 2D, single-shot OVS RF pulses, allowing for flexible control of pattern geometry. The properties of this

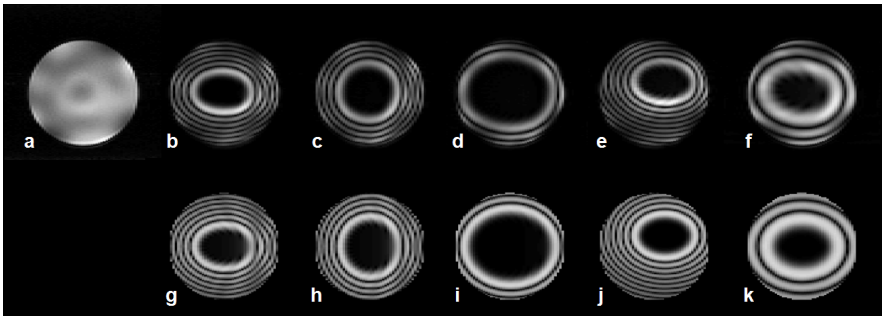

Figure 6.13: Experiments (top row) and simulations (bottom row). (a) Reference SE image. (b,g) Reference ellipse. (c,h) Circle. (d,i) Big ellipse. (e,j) Shifted ellipse. (f,k) Thick ellipse ($T_{\mathrm{p}} = 1\,\mathrm{ms}$).

method have been experimentally verified at 9.4 T. With this necessary step completed, it will now be possible to integrate dynamic B1 shim with multiple transmit channel within these OVS pulse in order to achieve a more homogeneous saturation while using a single RF pulse.

Chapter 7

Summary and Future Direction

Human magnetic resonance (MR) scanners are operated at higher and higher magnetic field to achieve improved image signal to noise ratio (SNR), enhanced blood-oxygen-level dependent (BOLD) effects in functional MRI and increased chemical dispersion in MR spectroscopy. However, the presence of severe transmit B1 inhomogeneities at ultra high field leads to unfavorable nonuniform RF excitation observed in human tissues, affecting both tissue contrast and signal to noise ratio and limiting the application of many conventional MR imaging techniques. This thesis was motivated by the critical need to solve this issue, which is essential in enabling clinical investigations in humans at 7T and higher field. Parallel transmission, an emerging new technique, was used to mitigate transmit B1 inhomogeneities or achieve a 2D localized RF excitation with sufficiently short selective RF pulses. Novel methods were applied to obtain rapid and robust mapping of transmit B1 fields, to design 2D accelerated selective RF pulses with a 2D k-space trajectory and to calculate 3D RF pulses with a spoke trajectory. In addition, a novel pulse design method was proposed to design VERSEd RF pulses that resulted in significant SAR reduction in parallel transmission. These methods were implemented and validated on a 9.4 T human scanner, currently the highest available field to image humans.

The key contributions of this thesis are summarized as follows:

- First implementation and validation of 2D parallel transmission in the human head at 9.4 T using eight RF channels with successful RF pulse design for arbitrarily

shaped excitation profiles.

- Demonstration of a new method to design multidimensional adapted rate RF pulses with effective SAR reduction in parallel transmission.
- Development of a SAR computation model to investigate SAR properties of parallel transmission RF pulses based on eletromagnetic simulations.
- Additional preliminary work including
  - First implementation of 3D parallel transmission with spoke trajectories at 9.4T with demonstration in the human brain.
  - Development of a new, fast 2D transmit B1 mapping approach derived from the 3D-only Actual Flip angle Imaging (AFI) technique.
  - Demonstration of a new algorithm to design single-shot outer volume suppression RF pulses with highly accurate geometry control, a necessary preliminary step for implementing parallel transmission in the design of these pulses.

The long-term goal of this research is to extensively exploit the multi transmit capability to enable or improve clinical applications in human at ultra high field. Based on the body of work that was completed during this thesis, multiple future directions can now be drawn. A non-exhaustive list of these upcoming developments includes:

- Extension of the small tip angle RF pulse design algorithm towards non-linear large flip angle pulse design, required in a large number of sequences (e.g. refocusing RF pulses).
- In-depth investigation of the impact of different RF pulse design, RF coil geometry and number of RF coil elements on SAR characteristics in humans (brain and torso), using 3D SAR computational models.
- Development of spectral-spatial excitation algorithm for parallel transmission to achieve uniform slab-selective or voxel-selective excitation while maintaining a wide enough excitation bandwidth in order to cover a large range of metabolites of interest.

Bibliography

[1] J. T. Vaughan, M. Garwood, C. M. Collins, W. Liu, L. DelaBarre, G. Adriany, P. Andersen, H. Merkle, R. Goebel, M. B. Smith, and K. Ugurbil. 7T vs. 4T: Rf power, homogeneity, and signal-to-noise comparison in head images. *Magn. Reson. Med.*, 46(1):24–30, 2001.

[2] C. M. Collins, Q. X. Yang, J. H. Wang, X. Zhang, H. Liu, S. Michaeli, X. H. Zhu, G. Adriany, J. T. Vaughan, P. Anderson, H. Merkle, K. Ugurbil, M. B. Smith, and W. Chen. Different excitation and reception distributions with a single-loop transmit-receive surface coil near a head-sized spherical phantom at 300 mhz. *Magn. Reson. Med.*, 47(5):1026–1028, 2002.

[3] H. Bomsdorf, T. Helzel, D. Kunz, P. Roschmann, O. Tschendel, and J. Wieland. Spectroscopy and imaging with a 4 tesla whole-body MR system. *NMR Biomed.*, 1:151–158, 1988.

[4] H. Barfuss, H. Fischer, D. Hentschel, R. Ladebeck, and J. Vetter. Wholebody MR imaging and spectroscopy with a 4-T system. *Radiology*, 169:811–816, 1988.

[5] S. Ogawa, D. W. Tank, R. Menon, J. M. Ellermann, S. G. Kim, H. Merkle, and K. Ugurbil. Intrinsic signal changes accompanying sensory stimulation: functional brain mapping with magnetic resonance imaging. *Proc. Natl. Acad. Sci. USA*, 89:5951–5955, 1992.

[6] K. Ugurbil, M. Garwood, K. Hendrich, R. Hinke, X. Hu, R. S. Menon, H. Merkle, S. Ogawa, and R. Salmi. Imaging at high magnetic fields: Initial experiences at 4 tesla. *Magn Reson Quarterly*, 9:259–277, 1993.

[7] K. Ugurbil, G. Adriany, P. Andersen, W. Chen, M. Garwood, R. Gruetter, P.-G. Henry, S. G. Kim, H. Lieu, I. Tkac, T. Vaughan, P.-F. Van De Moortele, E. Yacoub, and X. Zhu. Ultrahigh field magnetic resonance imaging and spectroscopy. *Magn. Reson. Imaging*, 21(10):1263–1281, 2003.

[8] K. Ugurbil, G. Adriany, C. Akgun, P. Andersen, W. Chen, M. Garwood, R. Gruetter, P.-G. Henry, M. Marjanska, S. Moeller, P.-F. Van de Moortele, K. Prussmann, I. Tkac, J. T. Vaughan, F. Wiesinger, E. Yacoub, and X. Zhu. High magnetic fields for imaging cerebral morphology, function and biochemistry. In P.-M. Robitaille and L. J. Berliner, editors, *Ultra High Field Magnetic Resonance Imaging*, volume 26 of *Biological Magnetic Resonance*, pages 285–342. Springer, New York, USA, 2006.

[9] T. Vaughan, L. DelaBarre, C. Snyder, J. Tian, C. Akgun, D. Shrivastava, W. Liu, C. Olson, G. Adriany, J. Strupp, P. Andersen, A. Gopinath, P. F. Van de Moortele, M. Garwood, and K. Ugurbil. 9.4T human MRI: preliminary results. *Magn. Reson. Med.*, 56:1274–1282, 2006.

[10] J. T. Vaughan, H. P. Hetherington, J. O. Otu, J. W. Pan, and G. M. Pohost. High-frequency volume coils for clinical NMR imaging and spectroscopy. *Magn. Reson. Med.*, 32:206–218, 1994.

[11] J. T. Vaughan. Rf coil for imaging system. *U.S. Patent*, 6,633:161, 2003.

[12] Q. X. Yang, W. Mao, J. Wang, M. B. Smith, H. Lei, X. Zhang, K. Ugurbil, and W. Chen. Manipulation of image intensity distribution at 7T: passive rf shimming and focusing with dielectric materials. *J. Magn. Reson. Imaging*, 24:197–202, 2006.

[13] M. Garwood and K. Ugurbil. B1 insensitive adiabatic RF pulses. *NMR, Basic Principles and Progress*, 26:110–147, 1992.

[14] M. Garwood and L. DelaBarre. The return of the frequency sweep: designing adiabatic pulses for contemporary nmr. *J. Magn. Reson.*, 153:155–177, 2001.

[15] M. H. Levitt. Composite pulses. *Prog NMR Spectrosc*, 18:61–122, 1986.

[16] J. Pauly, D. Nishimura, and A. Macovski. A k-space analysis of small-tip-angle excitation. *J. Magn. Reson.*, 81(1):43–56, 1989.

[17] C. J. Hardy and H. E. Cline. Spatial localization in two dimensions using NMR designer pulses. *J. Magn. Reson.*, 82(3):647–654, 1989.

[18] S. Saekho, F. E. Boada, D. C. Noll, and V. A. Stenger. Small tip angle three-dimensional tailored radiofrequency slab-select pulse for reduced b1 inhomogeneity at 3 T. *Magn. Reson. Med.*, 53(2):479–484, 2005.

[19] S. Saekho, C. Y. Yip, D. C. Noll, F. E. Boada, and V. A. Stenger. Fast-kz three-dimensional tailored radiofrequency pulse for reduced b1 inhomogeneity. *Magn. Reson. Med.*, 55(4):719–724, 2006.

[20] U. Katscher, P. Börnert, C. Leussler, and J. S. van den Brink. Transmit sense. *Magn. Reson. Med.*, 49(1):144–150, 2003.

[21] Y. Zhu. Parallel excitation with an array of transmit coils. *Magn. Reson. Med.*, 51(4):775–784, 2004.

[22] D. K. Sodickson and W. J. Manning. Simultaneous acquisition of spatial harmonics (SMASH): fast imaging with radiofrequency coil arrays. *Magn. Reson. Med.*, 38:591–603, 1997.

[23] K. P. Pruessmann, M. Weiger, M. B. Scheidegger, and P. Boesiger. SENSE: sensitivity encoding for fast MRI. *Magn. Reson. Med.*, 42:952–962, 1999.

[24] M. A. Griswold, P. M. Jakob, R. M. Heidemann, M. Nittka, V. Jellus, J. Wang, B. Kiefer, and A. Haase. Generalized autocalibrating partially parallel acquisitions (GRAPPA). *Magn. Reson. Med.*, 47:1202–1210, 2002.

[25] P. Ullmann, S. Junge, M. Wick, F. Seifert, W. Ruhm, and J. Hennig. Experimental analysis of parallel excitation using dedicated coil setups and simultaneous rf transmission on multiple channels. *Magn. Reson. Med.*, 54(4):994–1001, 2005.

[26] K. Setsompop, L. L. Wald, V. Alagappan, B. Gagoski, F. Hebrank, U. Fontius, F. Schmitt, and E. Adalsteinsson. Parallel rf transmission with eight channels at 3 tesla. *Magn. Reson. Med.*, 56(5):1163–1171, 2006.

[27] Z. Zhang, C. Y. Yip, W. Grissom, D. C. Noll, F. E. Boada, and V. A. Stenger. Reduction of transmitter b1 inhomogeneity with transmit SENSE slice-select pulses. *Magn. Reson. Med.*, 57(5):842–847, 2007.

[28] G. Adriany, P. F. Van de Moortele, F. Wiesinger, S. Moeller, J. P. Strupp, P. Andersen, C. Snyder, X. Zhang, W. Chen, K. P. Pruessmann, P. Boesiger, T. Vaughan, and K. Ugurbil. Transmit and receive transmission line arrays for 7 tesla parallel imaging. *Magn. Reson. Med.*, 53(2):434–445, 2005.

[29] G. Metzger, C. Snyder, C. Akgun, T. Vaughan, K. Ugurbil, and P. F. Van de Moortele. Local b1+ shimming for prostate imaging with transceiver arrays at 7 tesla based on subject dependent transmit phase measurements. *Magn. Reson. Med.*, 59:396–409, 2008.

[30] W. Grissom, C. Y. Yip, Z. Zhang, V. A. Stenger, J. A. Fessler, and D. C. Noll. Spatial domain method for the design of rf pulses in multicoil parallel excitation. *Magn. Reson. Med.*, 56(3):620–629, 2006.

[31] P. Ullmann, R. Haueisen, S. Junge, F. Seifert, et al. Flexible feature specific inner-volume selection with Transmit SENSE: methods and applications in humans, animals and biological samples. In *14th Scientific Meeting of ISMRM*, page 130, Seattle, Washington, USA, 2006.

[32] U. Katscher, P. Vernickel, and J. Overweg. Basics of rf power behaviour in parallel transmission. In *13th Scientific Meeting of ISMRM*, page 17, Miami, USA, 2005.

[33] P. Ullmann, G. Wuebbeler, S. Junge, F. Seifert, W. Ruhm, and J. Hennig. Sar-analysis for transmit sense with a 4-channel head array at 3 T. In *14th Scientific Meeting of ISMRM*, page 601, Seattle, USA, 2006.

[34] S. Conolly, D. Nishimura, A. Macovski, and G. Glover. Variable-rate selective excitation. *J. Magn. Reson.*, 78(3):440–458, 1988.

[35] X. Wu, J. T. Vaughan, K. Ugurbil, and P. F. Van de Moortele. Correction of parallel transmit RF pulses at 9.4 T using measured gradient waveforms. In *17th Scientific Meeting of ISMRM*, page 4516, Honolulu, Hawaii, USA, 2009.

[36] X. Wu, J. T. Vaughan, K. Ugurbil, and P. F. Van de Moortele. Parallel excitation in the human brain at 9.4 T counteracting k-space errors with RF pulse design. *Magn. Reson. Med.*, 2010. Available online on December 16, 2009.

[37] X. Wu, C. Akgun, J. T. Vaughan, K. Ugurbil, and P. F. Van de Moortele. Sar reduction in transmit sense using adapted excitation k-space trajectories. In *15th Scientific Meeting of ISMRM*, page 673, Berlin, Germany, 2007.

[38] X. Wu, J. T. Vaughan, K. Ugurbil, and P. F. Van de Moortele. Implementation of VERSE parallel transmission at 9.4 T. In *17th Scientific Meeting of ISMRM*, page 2591, Honolulu, Hawaii, USA, 2009.

[39] X. Wu, J. T. Vaughan, K. Ugurbil, and P. F. Van de Moortele. 16-channel parallel transmission in the human brain at 9.4 tesla: Initial results. Submitted to 18th Scientific Meeting of ISMRM, 2010.

[40] X. Wu, C. Akgun, J. T. Vaughan, K. Ugurbil, and P. F. Van de Moortele. Sar analysis for transmit sense at 7T with a human head model. In *15th Scientific Meeting of ISMRM*, page 3350, Berlin, Germany, 2007.

[41] X. Wu, D. K. Deelchand, V. L. Yarnykh, K. Ugurbil, and P-F. Van de Moortele. Actual flip angle imaging: From 3d to 2d. In *17th Scientific Meeting of ISMRM*, page 372, Honolulu, Hawaii, USA, 2009.

[42] X. Wu, N. Powell, M. Marjanska, M. Garwood, K. Ugurbil, and P-F. Van de Moortele. A flexible design algorithm for single-shot 2d circular/elliptical OVS rf pulses. In *17th Scientific Meeting of ISMRM*, page 4503, Honolulu, Hawaii, USA, 2009.

[43] F. Bloch, W. W. Hansen, and M. E. Packard. Nuclear induction. *Phys. Rev.*, 69:127, 1946.

[44] E. M. Purcell, H. C. Torrey, and R. V. Pound. Resonance absorption by nuclear magnetic moments in a solid. *Phys. Rev.*, 69:37–38, 1946.

[45] W. G. Proctor and F. C. Yu. The dependence of a nuclear magnetic resonance frequency upon chemical compound. *Phys. Rev.*, 77:717, 1950.

[46] W. C. Dickinson. Dependence of the ^{19}F nuclear resonance position on chemical compound. *Phys. Rev.*, 77:736, 1950.

[47] R. R. Ernst and W. A. Anderson. Applications of fourier transform spectroscopy to magnetic resonance. *Rev. Sci. Instrum.*, 37:93–102, 1966.

[48] R. Damadian. Tumor detection by nuclear magnetic resonance. *Science*, 171:1151–1153, 1971.

[49] P. C. Lauterbur. Image formation by induced local interactions: examples employing nuclear magnetic resonance. *Nature*, 242:190–191, 1973.

[50] P. Mansfield. Multiplanar image formation using NMR spin echoes. *J. Phys. C: Solid State Phys.*, 10:L55–L58, 1977.

[51] T. R. Brown, B. M. Kincaid, and K. Ugurbil. NMR chemical shift imaging in three dimensions. *Proc. Natl. Acad. Sci. USA*, 79:3523–3526, 1982.

[52] D. B. Twieg. The k-trajectory formulation of the NMR imaging process with application in analysis and synthesis of imaging methods. *Med. Phys.*, 10:610, 1983.

[53] K. K. Kwong, J. W. Belliveau, D. A. Chesler, I. E. Goldberg, R. M. Weisskoff, B. P. Poncelet, D. N. Kennedy, B. E. Hoppel, M. S. Cohen, R. Turner, H.-M. Cheng, T. J. Brady, and B. R. Rosen. Dynamic magnetic resonance imaging of human brain activity during primary sensory stimulation. *Proc. Natl. Acad. Sci. USA*, 89:5675–5679, 1992.

[54] P. A. Bandettini, E. C. Wong, R. S. Hinks, R. S. Rikofsky, and J. S. Hyde. Time course epi of human brain function during task activation. *Magn. Reson. Med.*, 25:390–397, 1992.

[55] H. C. Torrey. Bloch equations with diffusion terms. *Phys. Rev.*, 104:563–565, 1956.

[56] J. Pauly, D. Nishimura, and A. Macovski. A linear class of large-tip-angle selective excitation pulses. *J. Magn. Reson.*, 82:571–587, 1989.

[57] M. A. Griswold, S. Kannengiesser, M. Mller, and P. M. Jakob. Autocalibrated accelerated parallel excitation (Transmit-GRAPPA). In *13th Scientific Meeting of ISMRM*, page 2435, Miami, FL, USA, 2005.

[58] K. Setsompop, V. Alagappan, B. Gagoski, T. Witzel, J. Polimeni, A. Potthast, F. Hebrank, U. Fontius, F. Schmitt, L. L. Wald, and E. Adalsteinsson. Slice-selective rf pulses for in vivo b1+ inhomogeneity mitigation at 7 tesla using parallel rf excitation with a 16-element coil. *Magn. Reson. Med.*, 60(6):1422–1432, 2008.

[59] P. A. Bottomley and E. R. Andrew. Rf magnetic field penetration, phase shift and power dissipation in biological tissue: implications for nmr imaging. *Phys. Med. Biol.*, 23(4):630–643, 1978.

[60] C. M. Collins, S. Li, and M. B. Smith. Sar and b1 field distributions in a heterogeneous human head model within a birdcage coil. specific energy absorption rate. *Magn. Reson. Med.*, 40(6):847–856, 1998.

[61] D. I. Hoult and D. Phil. Sensitivity and power deposition in a high-field imaging experiment. *J. Magn. Reson. Imaging*, 12(1):46–67, 2000.

[62] J. Jin and J. Chen. On the SAR and field inhomogeneity of birdcage coils loaded with the human head. *Magn. Reson. Med.*, 38:953–963, 1997.

[63] U. Katscher, J. Rohrs, and P. Börnert. Basic considerations on the impact of the coil array on the performance of transmit sense. *Magma (New York, N.Y.)*, 18(2):81–88, 2005.

[64] K. Yee. Numerical solution of initial boundary value problems involving maxwell's equations in isotropic media. *IEEE Transactions on Antennas and Propagation*, 14:302–307, 1966.

[65] D. L. Phillips. A technique for the numerical solution of certain integral equations of the first kind. *J. ACM*, 9:84–97, 1962.

[66] A. N. Tikhonov. Solution of incorrectly formulated problems and the regularization method. *Soviet Math. Dokl.*, 4:1035–1038, 1963.

[67] O. Axelsson. *Iterative Solution Methods*. Cambridge University Press, Cambridge, UK, 1994.

[68] G. H. Golub and C. F. Van Loan. *Matrix Computations*. The John Hopkins University Press, Baltimore, MD, third edition, 1996.

[69] K. Miller. Least squares methods for ill-posed problems with a prescribed bound. *J. Math. Anal.*, 1:52–74, 1970.

[70] P. C. Hansen. Analysis of discrete ill-posed problems by means of the l-curve. *SIAM Review*, 34:561–580, 1992.

[71] P. Hansen. *Rank-Deficient and Discrete Ill-Posed Problems*. Philadelphia, 1998.

[72] E. K. Insko and L. Bolinger. Mapping of radiology field. *J. Magn. Reson.*, 103:82–85, 1993.

[73] C. H. Cunningham, J.M. Pauly, and K. S. Nayak. Saturated double-angle method for rapid b1+ mapping. *Magn. Reson. Med.*, 55:1326–1333, 2006.

[74] V. L. Yarnykh. Actual flip-angle imaging in the pulsed steady state: a method for rapid three-dimensional mapping of the transmitted radiofrequency field. *Magn. Reson. Med.*, 57(1):192–200, 2007.

[75] J. P. Mugler and G. W. Miller. Rapid 3d mapping of the b1 field using a low-flip-angle, phase-based method with improved sensitivity. In *15th Scientific Meeting of ISMRM*, page 351, Berlin, Germany, 2007.

[76] D. O. Brunner, S. Schweizer, and K. P. Pruessmann. Fast mapping of highly inhomogeneous rf fields. In *15th Scientific Meeting of ISMRM*, page 353, Berlin, Germany, 2007.

[77] P. F. Van de Moortele, Carl Snyder, Lance DelaBarre, G. Adriany, J. T. Vaughan, and K. Ugurbil. Calibration tools for rf shim at very high field with multiple element rf coils: from ultra fast local relative phase to absolute magnitude b1+ mapping. In *15th Scientific meeting of ISMRM*, page 1676, Berlin, 2007.

[78] S. Zhao, L. J. Gregory, and G. J. Parker. A fast 3d b1 mapping method at 3t. In *16th Scientific Meeting of ISMRM*, page 356, Toronto, Canada, 2008.

[79] Michael Schar, P. A. Vonken, and Matthias Stuber. Simultaneous b0- and b1-map acquisition for fast localized shim, frequency and rf power determination in the heart at 3T. In *16th Scientific Meeting of ISMRM*, page 358, Toronto, Canada, 2008.

[80] J. J. Hsu, G. Zaharchuk, and G. H. Glover. Fast simultaneous measurement of the rf flip angle and the longitudinal relaxation time for quantitative mri. In *16th Scientific Meeting of ISMRM*, page 360, Toronto, Canada, 2008.

[81] J. Y. Park and M. Garwood. B1 mapping using phase information created by frequency-modulated pulses. In *16th Scientific Meeting of ISMRM*, page 361, Toronto, Canada, 2008.

[82] P. F. Van de Moortele, C. Snyder, L. DelaBarre, C. Akgun, X. Wu, T. Vaughan, and K. Ugurbil. Fast mapping of relative b1+ phase in the human head at 9.4 tesla with a 14 channel transceive coil array. In *Intnl symposium on Biomed Magn Reson Imaging and Spectroscopy at Very High Fields*, page 37, Wuerzburg, 2006.

[83] P. F. Van de Moortele, C. Akgun, G. Adriany, S. Moeller, J. Ritter, C. M. Collins, M. B. Smith, J. T. Vaughan, and K. Ugurbil. B1 destructive interferences and spatial phase patterns at 7 t with a head transceiver array coil. *Magn. Reson. Med.*, 54(6):1503–1518, 2005.

[84] V. L. Yarnykh. Improved accuracy of variable flip angle t1 measurements using optimal radiofrequency and gradient spoiling. In *16th Scientific Meeting of ISMRM*, page 234, Toronto, Canada, 2008.

[85] D. I. Hoult. The principle of reciprocity in signal strength calculations - a mathematical guide. *Concepts Magn. Reson.*, 12:173–187, 2000.

[86] P. Bornert and T. Schaffter. Curved slice imaging. *Magn. Reson. Med.*, 36(6):932–939, 1996.

[87] D. Xu, K. F. King, Y. Zhu, G. C. McKinnon, and Z. P. Liang. A noniterative method to design large-tip-angle multidimensional spatially-selective radio frequency pulses for parallel transmission. *Magn. Reson. Med.*, 58(2):326–334, 2007.

[88] P. Vernickel, P. Roschmann, C. Findeklee, K. M. Ludeke, Ch Leussler, J. Overweg, U. Katscher, I. Grasslin, and K. Schunemann. Eight-channel transmit/receive body MRI coil at 3T. *Magn. Reson. Med.*, 58(2):381–389, 2007.

[89] A. Takahashi and T. Peters. Compensation of multi-dimensional selective excitation pulses using measured k-space trajectories. *Magn. Reson. Med.*, 34(3):446–456, 1995.

[90] P. Bornert and B. Aldefeld. On spatially selective rf excitation and its analogy with spiral mr image acquisition. *Magma (New York, N.Y.)*, 7(3):166–178, 1998.

[91] P. Ullmann, M. Haas, F. Hennel, M. Wick, J. Voiron, M. Zaitsev, J. Hennig, and W. Ruhm. Parallel excitation experiments using measured k-space trajectories for pulse calculation. In *16th Scientific Meeting of ISMRM*, page 1313, Toronto, 2008.

[92] K. Setsompop, A. C. Zelinski, V. Alagappan, J. Nistler, A. Hebrank, U. Fontius, F. Schmid, L. L. Wald, and E. Adalsteinsson. In vivo parallel rf excitation with b0 correction. In *15th Scientific Meeting of ISMRM*, page p. 671, Berlin, Germany, 2007.

[93] G. Adriany, P. F. Van de Moortele, F. Wiesinger, P. Andersen, J. P. Strupp, X. Zhang, C. Snyder, W. Chen, K. P. Pruessmann, P. Boesiger, J. T. Vaughan, and K. Ugurbil. Transceive stripline arrays for ultra high field parallel imaging applications. In *11th Scientific Meeting of ISMRM*, page 474, Toronto, Canada, 2003.

[94] G. H. Glover. Simple analytic spiral k-space algorithm. *Magn. Reson. Med.*, 42(2):412–415, 1999.

[95] P. Jezzard and R. S. Balaban. Correction for geometric distortion in echo planar images from bo field variations. *Magn. Reson. Med.*, 34:65–73, 1995.

[96] E. T. Jaynes. Matrix treatment of nuclear induction. *Phys. Rev.*, 98(4):1099–1105, 1955.

[97] J. Schneider, M. Haas, J. Hennig, S. Junge, W. Ruhm, and P. Ullmann. Coping with off-resonance effects and gradient imperfections in parallel transmission experiments. *17th Scientific Meeting of ISMRM*, page 172, 2009.

[98] M. T. Alley, G. H. Glover, and N. J. Pelc. Gradient characterization using a fourier-transform technique. *Magn. Reson. Med.*, 39(4):581–587, 1998.

[99] J. H. Duyn, Y. Yang, J. A. Frank, and J. W. van der Veen. Simple correction method for k-space trajectory deviations in mri. *J. Magn. Reson.*, 132(1):150–153, 1998.

[100] A. C. Zelinski, K. Setsompop, V. Alagappan, B. A. Gagoski, L. M. Angelone, G. Bonmassar, U. Fontius, F. Schmitt, E. Adalsteinsson, and L. L. Wald. Pulse design methods for reduction of specific absorption rate in parallel rf excitation. In *15th Scientific Meeting of ISMRM*, page 1698, Berlin, Germany, 2007.

[101] R. Lattanzi, D. K. Sodickson, A. K. Grant, and Y. Zhu. Electrodynamic constraints on homogeneity and radiofrequency power deposition in multiple coil excitations. *Magn. Reson. Med.*, 61(2):315–334, 2009.

[102] I. Graesslin, J. Weller, F. Schweser, B. Annighoefer, S. Biederer, U. Katscher, T. Nielsen, P. Harvey, and P. Börnert. Sar hotspot reduction by temporal averaging in parallel transmission. In *17th Scientific Meeting of ISMRM*, page 176, Honolulu, USA, 2009.

[103] I. Graesslin, S. Biederer, F. Schweser, K. H. Zimmermann, U. Katscher, and P. Börnert. Sar reduction for parallel transmission using verse and k-space filtering. In *15th Scientific Meeting of ISMRM*, page 674, Berlin, Germany, 2007.

[104] D. Xu, K. F. King, and Z. P. Liang. Variable slew-rate spiral design: theory and application to peak b1 amplitude reduction in 2D RF pulse design. *Magn. Reson. Med.*, 58(4):835–842, 2007.

[105] K. Setsompop, L. L. Wald, V. Alagappan, B. A. Gagoski, and E. Adalsteinsson. Magnitude least squares optimization for parallel radio frequency excitation design demonstrated at 7 tesla with eight channels. *Magn. Reson. Med.*, 59:908–915, 2008.

[106] G. Adriany, A. Gozubuyuk, E. J. Auerbach, P. F. Van de Moortele, P. Andersen, S. Moeller, J. T. Vaughan, and K. Ugurbil. A 32 channel transmit/receive transmission line head array for 3D rf shimming. In *15th Scientific Meeting of ISMRM*, page 168, Berlin, Germany, 2007.

[107] G. Adriany, D. Deelchand, P. Henry, J. Tian, J. Vaughan, K. Ugurbil, and P. F. Van de Moortele. A 16 channel T/R open-faced head array for humans at 9.4T. In *17th Scientific Meeting of ISMRM*, page 3005, Honolulu, USA, 2009.

[108] C. J. Snyder, L. DelaBarre, C. Akgun, S. Moeller, G. Adriany, K. Ugurbil, and J. T. Vaughan. High-field transmission line arrays for transmit and receive. In *14th Scientific Meeting of ISMRM*, page 421, Seattle, WA, USA, 2006.

[109] G. Adriany, J. Ritter, P-F. Van de Moortele, S. Moeller, C. Snyder, B. Voje, T. Vaughan, and K. Ugurbil. A geometrically adjustable 16 channel transceive transmission line array for 7 tesla. In *13th Scientific Meeting of ISMRM*, page 673, Miami, FL, USA, 2005.

[110] J. Pauly, P. Le Roux, D. Nishimura, and A. Macovski. Parameter relations for the Shinnar-Le Roux selective excitation pulse design algorithm. *IEEE Trans. Med. Imaging*, 10:53–65, 1991.

[111] N. J. Powell, M. Marjanska, J. Valette, P-G. Henry, and M. Garwood. A new method for single-shot 2-d OVS. In *16th Scientific Meeting of ISMRM*, page 1327, Toronto, Canada, 2008.

[112] R. R. Ernst. Sensitivity enhancement in magnetic resonance. *Adv. Magn. Reson.*, 2:1–135, 1966.

[113] T-H. Chang, Z-Q. Luo, X. Wu, C. Akgun, T. Vaughan, K. Ugurbil, and P-F. Van de Moortele. Transmit b1 shimming at high field with sar constraints: A

two stage optimization method independent of the initial set of rf phases and amplitudes. In *16th Scientific Meeting of ISMRM*, page 1088, Toronto, Canada, 2008.